Electro-optical properties of dislocations in silicon and their possible application for light emitters

Von der Fakultät für Mathematik, Naturwissenschaften und Informatik
der Brandenburgischen Technischen Universität Cottbus

zur Erlangung des akademischen Grades
Doktor der Naturwissenschaften
(Dr. rer. nat.)

genehmigte
Dissertation
vorgelegt von

Diplom-Ingenieurphysiker

Tzanimir Vladimirov Arguirov
geboren am 12. Mai 1971 in Sofia, Bulgarien

Gutachter:
Prof. Dr. rer. nat. habil Jürgen Reif
Prof. Dr. sc. nat. Martin Kittler
Prof. Dr. rer. nat. habil Hans-Joachim Fitting

Tag der mündlichen Prüfung: 14.10.2007

Contents

Introduction

Dislocations in silicon can have a decisive influence on the performance of electronic devices. The interest in the dislocation properties is driven mainly because of two practical reasons. One is the application of multicrystalline silicon for solar cells production, which contains dislocations [Möl1996, Sch2004], and the other is the possibility to enhance the raditive properties of the silicon by introducing dislocations [Ng2001, Pan2004, Pav2003, Kve2005]. A deeper understanding is required of the mechanisms governing the dislocation recombination activity, their radiation, and how they interact with other defects present in silicon.

The dislocation specific radiation may provide a means for optical diagnostics of solar cell grade silicon.

One broad application of the solar energy requires decreasing of the production costs while increasing the efficiency of the solar cells. Multicrystalline silicon is an alternative, which meets both the low cost production and the high efficiency requirements for solar cells. The production of highly efficient solar cells require high minority carrier lifetime in the starting material and effective lifetime updating during the processing into solar cell. It is recognized that a high dislocation density is one of the major factors which limits the material quality and their recombination activity is decisive for the carrier lifetime and diffusion length [Möl1996].

A technique which gives spectroscopic access to the dislocation activity is the investigation of the photoluminescence [Mudr2002, Ost1999, Kos1999, Tar1999]. Since multicristalline silicon wafers are inhomogeneous, there is a need to combine the spectral capabilities with the ability of spatially resolving the defect areas [Ost2000, Tar2000].

Enhancement of band-to-band radiation or strong dislocation-related radiation may provide a means for on-chip optical data transfer. Due to complexity of the current ultra large integrated circuits and meanwhile very fast switching times of the single transistors, a situation is reached where the signal delay is limited by transfer in the interconnects. It is reasonable to expect that the integration is progressing such that the length of the wiring on a single chip will be getting longer and longer. The total length of the interconnects of a modern microprocessor is estimated to several kilometres, and following the development trend it will be several ten kilometres in ten years. Not only is it the length of the wiring, which causes a concern, but also the increased complexity of their architecture. Signal cross-talk, RC-coupling, RL- delays are expected to introduce problems related to the delay in signal propagation due to the reduction in the dimensions and the increase in density of the metal lines.

A possible solution is looked for in optics [Pav2003]. Optical interconnects are one of the main motivations to look for silicon photonics. The main limitation for achieving monolithically integrated silicon microphotonic devices, is the lack of any practical Si-based light sources: either efficient light emitting diodes or Si lasers.

Aim and outline of the work

The goals of this work are to study how the dislocations present in silicon influence its radiative properties and to find ways to enhance the silicon radiation by controllable formation of dislocations. The first aspect of this research is the utilization of photoluminescence for monitoring of the recombination activity in solar cell grade silicon and the identification of contaminants, based on their photoluminescence signatures. It requires to correlate the luminescence spectral features and the recombination activity of the defects.

The second aspect is related to the preparation of silicon based light emitters for on-chip optical interconnects. It is looked for an enhancement of the sub-band-gap or band-to-band radiation, by controlled formation of dislocation rich areas in microelectronics grade silicon and understanding the processes governing such an enhancement.

The work contains three main parts.

In the first (Chapters 1 to 3), the applicability of scanning photoluminescence spectroscopy for the characterisation of solar cell grade material is explored. In the second part (Chapters 4 and 5), solar cell grade silicon, produced by different growth techniques is characterised. Photoluminescence mapping, electron beam induced current (EBIC) and comparison of the diffusion length with the wavelength dependent light penetration depth (spectral response; SR) are employed. The recombination activity of the defects is correlated with the spectral features of their luminescence. The ability of the photoluminescence spectroscopy is demonstrated to uncover material specific defects exhibiting strong luminescence in the temperature range 80 K-300 K.

Dislocations in solar cell grade material are in a random environment and their radiation is influenced by the local properties in the material. Thus, the solar grade materials provide a model system for studying dislocation radiative properties at different contamination and recombination activity.

The third part (Chapters 6 to 9) is devoted to the possibility to create silicon based light emitter utilizing the dislocation radiation or band-to-band radiation in silicon. Dislocation rich areas are analyzed, which were prepared in a controlled way on microelectronics grade silicon.

In details, Chapter 1, gives an overview of the main recombination processes in dislocated silicon. The processes of radiative recombination due to band-to-band transition and transitions at the dislocations are discussed.

Chapter 2 gives an overview of the literature related to the origin and the relation between the dislocation spectral features.

Chapter 3 presents a brief description on the applied experimental techniques and the typical characteristics of the materials, which are studied.

Chapter 4 reveals the correlation between the recombination activity of dislocations and their luminescence. Temperature dependent EBIC and photoluminescence are applied to study the relation between the dislocation contamination and their radiation.

In Chapter 5, typical defects which can be detected by means of photoluminescence mapping are discussed.

Chapter 6 reveals the different approaches for use of silicon as a light source material in view of their applicability for the on-chip application.

In Chapter 7, the parameters, which are used to characterise the silicon light emitting diodes, are reviewed and the method for a calibration of the photoluminescence system for absolute measurements of the radiant flux is described.

Chapter 8 presents the results of controllable dislocation formation by implantation and annealing. The observed enhancement of the band-to-band luminescence is analysed in view of competitive recombination mechanisms in silicon and optimal injection level. The role of the dislocation and the dopants for enhancement of the band-to-band radiation is discussed.

In chapter 9, the possibility for realizing a light emitter, based on dislocation activity of silicon, is discussed. Different methods for the preparation of the dislocation rich region in silicon wafers are used and their emission is characterized by photo- and electro- luminescence spectroscopy.

Part I

RECOMBINATION PROCESSES IN SILICON

Chapter 1

Recombination processes in silicon with dislocations

In this chapter the main recombination processes in dislocated silicon are presented. The processes of radiative recombination due to band-to-band transition and transitions at the dislocations are discussed.

In standard bulk silicon the probability of phonon assisted band-to-band luminescence is low and most of the excited electron–hole pairs recombine nonradiatively. Dislocations, when present in silicon, offer additional radiative and nonradiative routes for recombination. It will be shown, that the recombination activity of the dislocations is strongly influenced by the background metal contamination.

The *radiative* recombination processes and their temperature dependence are of main interest, because they provide a means for non-destructive and non-contact characterisation in luminescence experiments. However, the *nonradiative* recombination is decisive for the concentration of excited carriers and thus influences the efficiency of the radiative processes.

1.1. Radiative recombination. Bimolecular and monomolecular rate equations.

A recombination event in a semiconductor consists of the annihilation of one conduction band electron and one valence band hole. Thus the rate of the recombination, R, should be proportional to the concentration of electrons, n, and also to the concentration of holes, p. The recombination rate can be written as:

$$R = -\frac{dn}{dt} = -\frac{dp}{dt} = B n p , \qquad (1.1.)$$

Absorption of light or current injection leads to the formation of excess carriers in the semiconductors.

$$\begin{aligned} n &= n_0 + \Delta n \\ p &= p_0 + \Delta p \end{aligned} \qquad (1.2.)$$

where n_0 and p_0 denote the equilibrium concentrations and Δn and Δp are the concentrations of the excess carriers. The excitation is usually done in a way that the concentrations of both injected carrier types are equal $\Delta n = \Delta p$. Then the recombination rate, R, can be regarded as a sum of equilibrium R_0, and excess ΔR, recombination rates:

$$R = R_0 + \Delta R \qquad (1.3.)$$

Let us assume a p-type doped semiconductor with concentration of majority carriers $p_0 >> n_0$. The recombination rate of the excess carriers, is given by:

$$\Delta R = B(n_0 + \Delta n)(p_0 + \Delta p) - B n_0 p_0 = B(n_0 + p_0)\Delta n + B\Delta n^2 . \qquad (1.4.)$$

In case of low injection ($\Delta n << p_0$), the term containing Δn^2 can be neglected and the rate of recombination becomes linearly dependent on the injected carrier concentration:

$$\Delta R = B(n_0 + p_0)\Delta n . \qquad (1.5.)$$

Thus one obtains the 'monomolecular' rate equation which holds at low injections, when the amount of carriers introduced in the semiconductor is negligible compared to the concentration of the majority carrier.

At high injections ($\Delta n >> p_0$), the term containing Δn^2 in equation (1.4.) prevails so one obtains:

$$\Delta R = B\Delta n^2 . \qquad (1.6.)$$

This equation is the 'bimolecular' rate equation and the coefficient B denotes the recombination coefficient.

In case of radiative recombination, the coefficient B is also related to the intensity of the emitted radiation. It can be theoretically estimated by application of a detailed balance principle [Roo1954]. According this principle, the rate of radiative recombination at thermal equilibrium in an elementary frequency interval, $\mathrm{d}\nu$, at frequency, ν, is equal to the corresponding rate of generation of electron – hole pairs by thermal radiation. The generation rate then is defined by the spectral photon density (number of photons in unit volume and unit frequency interval) in the semiconductor, $\rho(\nu)$, which is determined by Planck's law,

$$\rho(\nu)\mathrm{d}\nu = \frac{8\pi\nu^2}{c^3}\frac{n_s^2\left[\dfrac{d(n_s\nu)}{d\nu}\right]}{\exp\left(\dfrac{h\nu}{kT}\right)-1}d\nu , \qquad (1.7.)$$

and the probability at which photons are absorbed in the semiconductor. The absorption probability is given by the product of the group velocity of the light, $V_g = c\, d\nu / d(n_s\nu)$, and the semiconductor's absorption coefficient, α. Thus the $R(\nu)\mathrm{d}\nu$ becomes:

$$\mathrm{R}(\nu)\mathrm{d}\nu = \frac{8\pi\alpha {n_s}^2}{c^2}\frac{\nu^2}{\exp\left(\frac{h\nu}{kT}\right)-1}d\nu, \qquad (1.8.)$$

where n_s stands for the refractive index of the semiconductor, c, h, and k are, respectively, the speed of light, Boltzmann's and Planck's constants. Upon integration of this equation, taking into account the dispersion of absorption coefficient and refractive index, one gets the radiative recombination rate, $R = \int_0^\infty R(\nu)\,d\nu$ [Roo1954, Var1967]. This recombination rate is characteristic for thermal equilibrium ($n_0\ p_0 = {n_i}^2$). The radiative recombination coefficient is calculated by the ratio of the recombination rate and the squared intrinsic carrier concentration, n_i:

$$B = \frac{R}{{n_i}^2} \qquad (1.9.)$$

Silicon being an indirect semiconductor, optical interaction at the band gap energy must be assisted by phonon interaction to compensate for the momentum mismatch. An analytical expression for B requires the absorption coefficient $\alpha(\nu)$ in an analytical form. For silicon the absorption coefficient in the range of the band-to-band luminescence can be approximated by the following expressions [Mac1995]:

$$\alpha = A\left[\frac{(h\nu - E_g + k\vartheta)^2}{e^{\vartheta/T}-1} + \frac{(h\nu - E_g - k\vartheta)^2}{1-e^{-\vartheta/T}}\right]; \qquad h\nu > E_g + k\vartheta \qquad (1.10.a)$$

$$\alpha = A\left[\frac{(h\nu - E_g + k\vartheta)^2}{e^{\vartheta/T}-1}\right]; \qquad E_g - k\vartheta \le h\nu \le E_g + k\vartheta \qquad (1.10.b)$$

$$\alpha = 0; \qquad h\nu < E_g - k\vartheta \qquad (1.10.c)$$

where A is a constant independent on the temperature, E_g denotes the band gap energy of silicon, ϑ is the Debye temperature (i.e. $k\vartheta$ is the mean phonon energy) and T is the temperature of the sample.

Taking into account this analytical expression for α, Varshni [Var1967] obtained the following expression for the radiative rate coefficient:

$$B_{indirect} = \frac{Ah^3{n_s}^2}{2\pi^2c^2}\frac{{E_g}^2}{M_c(m_e m_h)^{3/2}}\frac{e^{\vartheta/T}+1}{e^{\vartheta/T}-1}, \qquad (1.11.)$$

where m_e, m_h stand for the electron and hole effective masses (for the density of states calculations), and $\mathrm{M_c}$ is the number of equivalent minima in the conduction band (six for

silicon). The same expression (but just written in the form as monomolecular rate equation) has been derived by Dumke [Dum1957] from a microscopic analysis of the indirect transition.

Expression (1.11.) does not account for formation of excitons, i.e. the Coulomb attraction between electrons and holes and. Although, it agrees for the order of magnitude with the experimental results, it makes a wrong prediction for the temperature dependence of the radiative band-to-band recombination [Sch1974]. Because the phonon states are increasingly occupied on increasing temperature, *B*, according to (1.11) shows increase, too. Such temperature behaviour of the recombination coefficient is not observed experimentally.

The Coulomb attraction enhances the probability that an electron and a hole can be found at the same position in space. Recombination events are then favoured due to their close proximity. Due to thermal motion, the excitons become destroyed more easily at higher temperature and correspondingly their recombination is hindered. For the recombination coefficient, *B*, this results in the following expression [Sch1974]:

$$B_{indirect} = 2\sqrt{\pi}\sqrt{\frac{G}{kT}}\left(1+2\frac{G}{kT}e^{G/kT}\right)C\frac{e^{\vartheta/T}+1}{e^{\vartheta/T}-1}, \qquad (1.12.)$$

where *G* is the binding energy of the excitons (15meV) and *C* denotes the first two temperature independent terms in (1.11).

An alternative way to overcome the problem with the wrongles predicted temperature behaviour in the theory of Varshni is to implement experimental data or a more accurate model for the absorption of silicon in (1.8). Thus instead the absorption coefficient approximation given by Macfarlane and Roberts [Mac1995] one can implement the that given by Elliott [Ell1957], already accounting for the absorption due to the excitons.

From Eq. 1.10 it is obvious that the phonon contribution to the optical interaction results in a broadening of the spectrum of α, accounting for the phonon emission and phonon absorption respectively. At low temperatures phonon absorption is the main mechanism determining the photon absorption. However, at elevated temperatures (80 K – 300 K), photon absorption in the branch of phonon emission gives a significant contribution [Tru2003]. Absorption spectra in the range of phonon emission down to four phonon processes below the band gap of silicon have been reported. The radiative recombination coefficient, *B*, is then calculated by numerical integration of Eq. (1.8), using experimentally obtained absorption curves for different temperatures.

The radiative recombination coefficients calculated in the studies of Schlangenotto et al. [Sch1974], Varshni [Var1967], and by Trupke et al. [Tru2003] for several temperatures in the interval 90 – 300 K are given in Table 1.1.

T, K	B, cm^3/s		
	Varshni [Var1967]	Schlangenotto [Sch1974]	Trupke [Tru2003]
90	1.27 x 10^{-15}	*2.8 x 10^{-13}*	4.57 x 10^{-14}
112	*1.3 x 10^{-15}*	*1.3 x 10^{-13}*	2.14 x 10^{-14}
170	*1.4 x 10^{-15}*	*3.2 x 10^{-14}*	8.84 x 10^{-15}
195	1.43 x 10^{-15}	*2.5 x 10^{-14}*	7.35 x 10^{-15}
249	1.60 x 10^{-15}	*1.4 x 10^{-14}*	5.48 x 10^{-15}
300	*1.77 x 10^{-15}*	*9.8 x 10^{-15}*	4.73 x 10^{-15}

Table 1.1. Values for the radiative recombination coefficient according to Schlangenotto et al. [Sch1974], Varshni [Var1967], and Trupke et al. [Tru2003]. The data in italic are either calculated by the formulas given in the respective text or extracted from the graphs in the corresponding references.

1.2. Nonradiative recombination in silicon

The nonradiative recombination, which is considered here, is due to Shockley–Read–Hall (SRH) multi phonon and Auger recombination processes. Nonradiative recombination occurs also at extended defects. This will be considered separately.

1.2.1. Shockley–Read–Hall recombination

Despite all improvements, a small amount of impurities and crystal imperfections in the final wafer is inevitable. Some of them can be electrically active, causing levels in the band gap. Thus the impurities appear as recombination active centres or traps for minority carriers. The recombination rate caused due to their presence in the material is given by [Sho1952, Hal1952]:

$$R_{SRH} = \frac{n\,p - n_i^{\,2}}{(n + n_1)\tau_p + (p + p_1)\tau_n}, \qquad (1.13.)$$

where the electron and hole concentrations are given by n and p and n_i^2 is the intrinsic carrier concentration. The lifetimes τ_n and τ_p are electron and hole lifetimes, when the recombination centres are completely empty or completely occupied by electrons, respectively. They are related to the recombination centre density, N_t, their capture cross section for holes, σ_p, and electrons, σ_n, and the carriers' thermal velocity $V_{th,\,p}$ or $V_{th,\,n}$ (~ 10^7 cm/s in silicon):

$$\tau_n = \frac{1}{\sigma_n V_{th,n} N_t} \text{ and } \tau_p = \frac{1}{\sigma_p V_{th,\,p} N_t}. \qquad (1.14.a)$$

The concentrations n_1 and p_1 are defined as the equilibrium electron and hole concentrations when the Fermi level coincides with the energetic position of the recombination centre, E_t in the band gap:

$$n_1 = N_c \exp\left(\frac{E_t - E_c}{kT}\right) \text{ and } p_1 = N_V \exp\left(\frac{E_v - E_t}{kT}\right). \qquad (1.14.b)$$

(Here N_c and N_v are the effective density of states in the conduction and valence band, respectively, k is the Boltzmann constant and T denotes the temperature. E_c and E_v stand for the conduction and the valence band energy, respectively)

At low injection the SRH recombination is usually the prevailing recombination in silicon. In doped materials the change in the concentration of the majority carriers due to the injection can be neglected and the contribution in the total recombination due to SRH mechanism can be simplified:

$$\Delta R_{SRH} = \frac{\Delta n}{\tau_{SRH}}, \qquad (1.15.)$$

where τ_{SRH} denotes the minority carrier lifetime and Δn is their concentration.

The SRH model describes the total recombination in the following assumptions:

- No presence of radiative or Auger transitions.
- Non degenerated semiconductor.
- The energy position of the recombination centre E_t does not depend on the occupation.
- The relaxation of carriers captured at the centre is much faster than the emission processes.
- The recombination centres are homogeneously distributed and at much lower concentration than the doping concentration.
- There is no direct interaction between the defects.
- Fermi-Dirac-Statistics is applicable.

1.2.2. Auger recombination

In the case of high injection or high concentration of majority carriers (~10^{18} cm^{-3}) one should take into account also Auger processes.

Auger processes, occur when the energy released due to the recombination of an electron-hole pair via band gap is transferred to an addition carrier (either electron or hole), which then dissipates this energy by emitting phonons. This process involves three particles and presumes that their concentration is sufficiently high, so that such collisions become probable. A large number of Auger processes can occur, depending on the carrier concentration and the nature of the possible transitions [Pan1975]. Figure 1.1 illustrates some of them. Dziewior and Schmid [Dzi1977] showed that the Auger process in silicon is not significantly influenced by the presence of impurities and the main contribution is either due to electron-electron-hole (eeh) or due to electron-hole-hole (ehh) recombination (see Figure 1.1 a and b). The

recombination rate in Auger process is dependent on the concentration of all three species participating in the recombination:

$$R_{Auger} = C_{eeh} n^2 p + C_{ehh} n p^2, \qquad (1.16.)$$

where C_{eeh} and C_{ehh} stand for the e-e-h and e-h-h recombination mechanism, correspondingly.

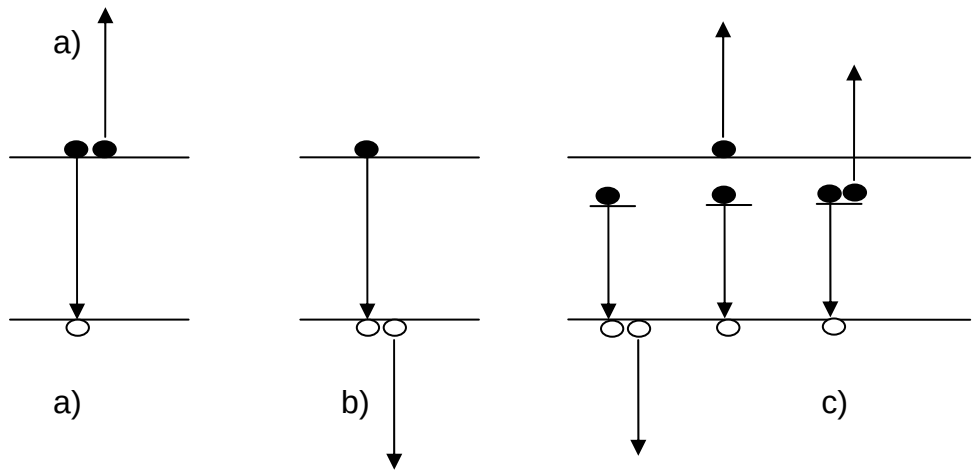

Figure 1.1. Diagram of Auger processes. a) Electron–electron–hole process in which the transition energy is carried away by an electron. b) Electron–hole– hole process in which the transition energy is carried away by a hole. c) Processes involving a level in the band gap with different possibilities of transferring the energy to the third carrier.

Both coefficients depend slightly on the temperature [Dzi1977] (Table 1.2) and are not influenced by presence of impurities.

T, K	77	300	400
C_{eeh}, cm^6/s	$2.3X10^{-31}$	$2.8X10^{-31}$	$2.8X10^{-31}$
C_{ehh}, cm^6/s	$7.8X10^{-31}$	$9.9X10^{-31}$	$1.2X10^{-31}$

Table 1.2. Auger coefficients for eeh and ehh recombination at different temperatures. Data from [Dzi1977]

1.3. Dislocation recombination activity

Annihilation of electrons and holes at a dislocation requires capturing of minority carriers at the dislocation line and subsequent recombination. In silicon the dislocation can be regarded as charged lines, capable of attracting minority carriers. The charge and the recombination activity of the dislocations depend on the presence of deep states induced in the band gap by the defect.

1.3.1. Dislocations charge

The presence of defects and dangling bonds at the dislocation implies a possible charging. Indeed, in doped silicon such defects capture majority carriers and the dislocations become charged [Ale1990]. Around the dislocation a space charge region is formed (Read cylinder), maintaining the total neutrality of the system (Figure 1.2). Thus, the dislocations cause a band banding in the semiconductor, compensating for the dislocation charge.

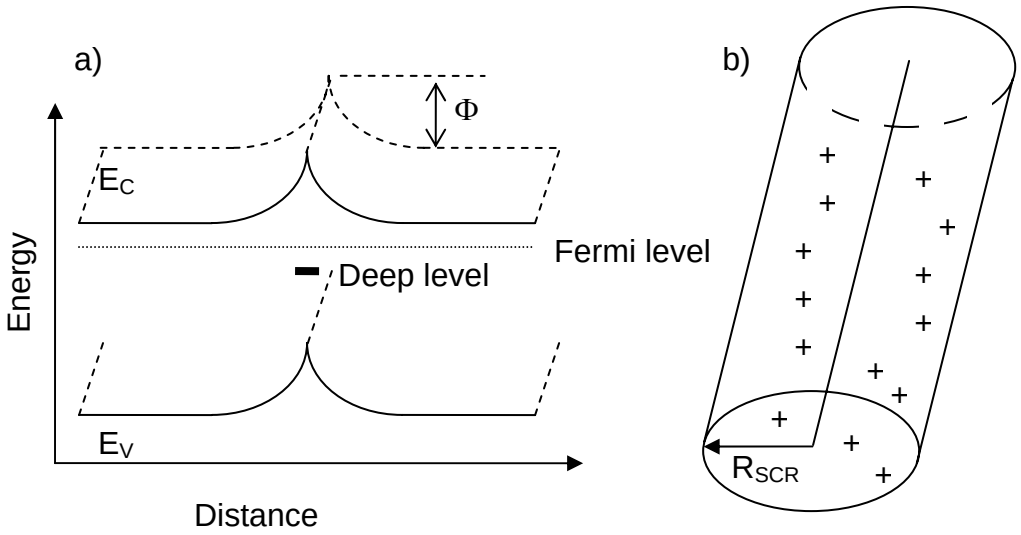

Figure 1.2. Model of charged dislocation in n- type material. a) Space charge region and band bending at dislocation. b) Space charge cylinder with charged dopants.

There is a relation between the formed potential barrier, Φ, and the charge carrier line density at the dislocation, N_{tot} [Kve2001]:

$$\Phi = \frac{e\,N_{tot}}{4\,\pi\,\varepsilon_{Si}}\left(\ln\left[\frac{N_{tot}^{\,3}}{(\pi N_d)}\right]-1\right), \qquad (1.17.)$$

where ε_{Si} is the permittivity of the semiconductor, e - the elementary charge and N_d - the dopant concentration. The radius of the space charge region is given by:

$$R_{SCR} = \sqrt{\frac{N_{tot}}{\pi N_d}} \qquad (1.18.)$$

The dislocations exhibit amphoteric character. They can be positively or negatively charged depending on the doping type. In n-type material the dislocations are negatively and in p-type material they are positively charged.

Recombination at the dislocations occurs when minority carriers captured at the dislocations recombine trough the states in the band gap.

1.3.2. Recombination activity at the dislocations. Role of contamination

The recombination activity at the dislocations is best illustrated, considering their contrast behaviour in an electron beam induced current (EBIC) experiment. In EBIC, a short circuit current is induced in a Schottky contact or p-n junction by injection of an electron beam. The variations of this current upon scanning the electron beam is measured to map the sample. Specifically, variations are observed when the carriers induced by the electron beam in the bulk of the sample, cannot diffuse to the surface Schottky contact, but recombine at defects (or dislocations) in the bulk. The contrast c_c is defined by the difference between the measured current I_d when the beam hits the dislocation, and I when it is off the dislocation:

$$c_c = \frac{I - I_d}{I}. \qquad (1.19.)$$

The EBIC contrast reflects the recombination activity of the dislocations. Since the recombination activity of the dislocations depends on the temperature of the sample and the concentration of minority carriers, created by the electron beam, the contrast is a function of temperature and beam current.

A widely accepted picture assumes that activity of the dislocation is caused by recombination at the deep levels at the dislocations. According to this picture, one would expect that the dislocation contrast will have a positive slope upon increasing the temperature and a negative one on increasing the probe beam current. Indeed, in some cases such behaviour has been observed [Kit1995d, Kit1995c], although opposite behaviour has been detected, too [Kus1992, Rad1992, Kit1993b, Kit1993a, Kit1995d, Kit1995c]. In fact, experiments show that such behaviour can as well observed as a reversed dependence. An essential point is that the dislocation contrast is strongly influenced by the interaction of the dislocations with impurities.

The role of the transition metal contamination for the dislocation activity was demonstrated in numerous of studies [Kit1995d, Kit1995c,Kit1995b]. It was shown that the contrast behaviour is influenced by small amounts of metal impurities (in the range of ppb) present in the sample. Four major types of temperature behaviour, shown in Figure 1.3 can be distinguished [Kit1995d, Kit1995c].

- For as-grown, not contaminated sample, only a very faint contrast at low temperature (80K) is detectable, vanishing at higher temperatures (*Type II*). This is connected to represent the intrinsic dislocation recombination.
- At low contamination with transition metals (several ppb) the contrast is usually high at low temperature and drops with increasing the temperature (*Type 2*).

- Higher contamination with transition metals (several ten ppb) leads to a contrast increase with the temperature, although the contrast at low temperature is still high (*Type 1*).

-*Type I contrast* is caused by dislocation, decorated by metal silicide precipitates, acting as internal Schottky barriers. Such defects have a very high contrast, relative weak dependent on the temperature.

-*Mixed Type* behaviour, shows a temperature dependant EBIC contrast which is alike a superposition of type 1 and type 2. It exhibits a maximum at low temperature, but is still detectable at 300K. It is characteristic for contaminations in the range between those causing type 1 and type 2 behaviours [Kve2001].

Upon contamination with transition metals the dislocation contrast behaviour was found to change in the order: Type II ==> Type 2 ==> Mixed type ==> Type 1==> Type I.

The contrast behaviour can be reversed by gettering and passivation [Kit1995d, Kit1995c, Sei1997]. It was found that passivation in hydrogen plasma and phosphorous diffusion gettering can convert the behaviour of type 1, or mixed type to type 2. However, a conversion to type II was not detected, indicating that not all impurities captured at the dislocations can be gettered or passivated.

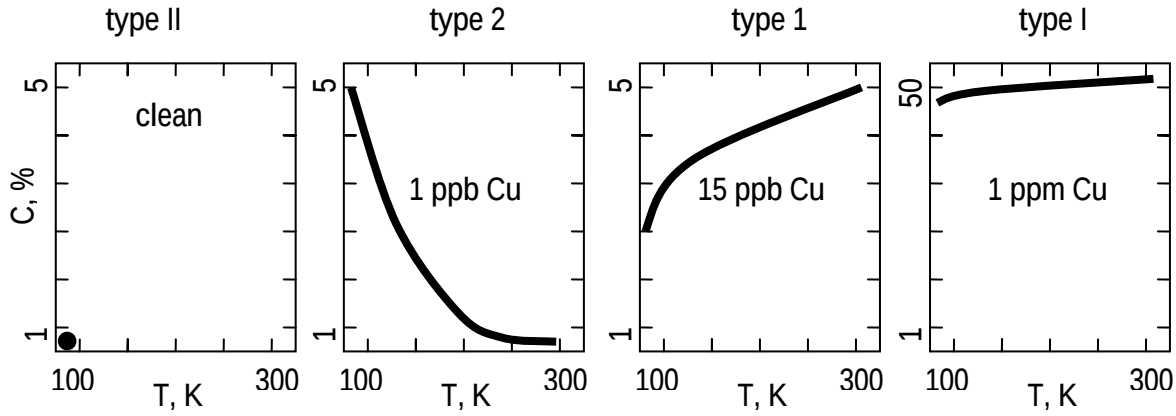

Figure 1.3. Schematic representation of the dominant types of dislocation contrast behaviour versus temperature in dependence on the Cu contamination. The thick lines represent the dominant contrast behaviour. (After [Kit1995y])

A comprehensive understanding of the interaction between dislocations and metals is given by a model of Kveder et al. [Kve2001]. The model describes the recombination at the dislocations supposing strong coupling between the metallic impurity deep level and the one-dimensional dislocation bands.

Straight 60° dislocations, which dissociate in 30° and 90° partials with a stacking fault ribbon in between, have reconstructed cores and no deep levels can be associated with them in the one-dimensional dislocation band gap. Only shallow bands, splitting from the valence and

conduction band can be associated with the strain field of the dislocation (Figure 1.4). The position of the dislocation conduction, E_{De}, and valence, E_{Dh}, bands has been estimated to about 70 - 80 meV from the conduction, E_C, and the valence, E_V, band edges of the bulk silicon and a space charge region around the dislocation is formed, causing band bending, Φ. An impurity level, E_m, at the vicinity or at the core of the dislocation can mediate the transitions at the dislocation.

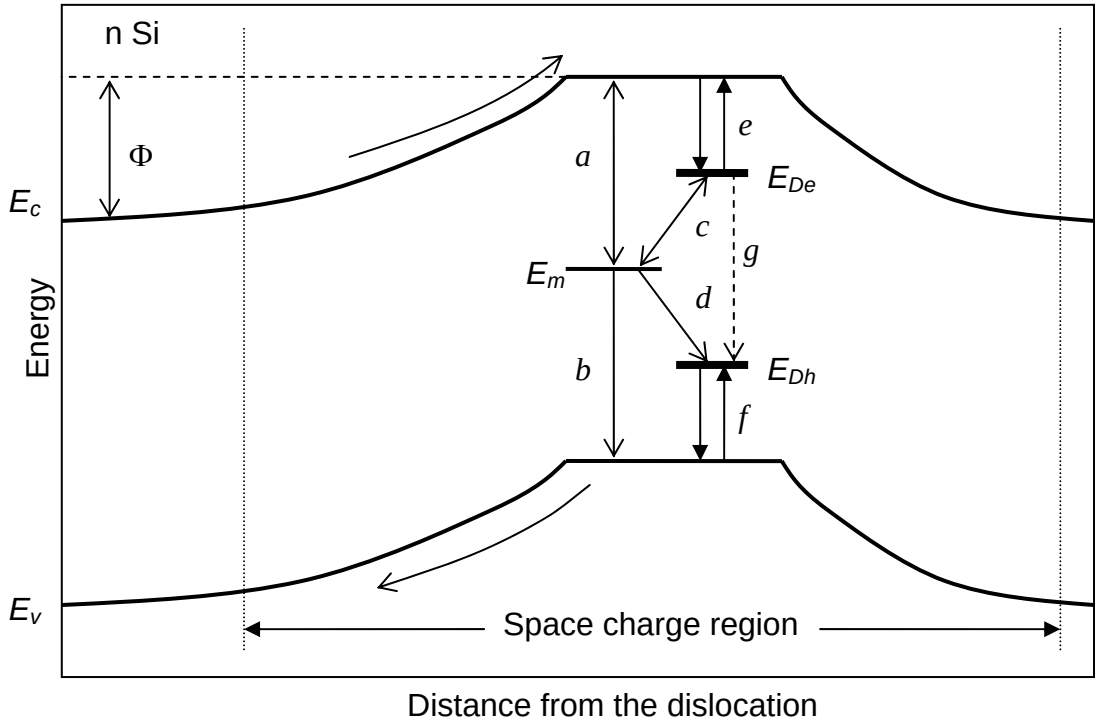

Figure 1.4. Scheme of the energy model of a dislocation in n-type Si interacting with metallic impurity, creating a deep level E_m. The band bending is caused by the negative charge of the dislocation in the n-type material. Recombination at the dislocation without presence of metallic impurity occurs with low probability between the one dimensional shallow dislocation bands (E_{Dh} - E_{De}) (dotted arrow). In presence of a deep centre many recombination transitions involving it are open. (After [Kve2001])

The model is based on the balance between the rates of carrier exchange and recombination between the dislocation bands and the states formed by the metal impurity (Figure 1.4). The model postulates a balance between all carrier exchange and recombination rates between the dislocation and the impurity. Each shallow dislocation band exchanges electrons or holes with the conduction (*e*) or valence band (*f*), respectively, and with the deep level of the metal atom, whereas the deep levels exchange charge carriers with the two dislocation bands (*c* and *d*) and also with the conduction and the valence band (*a* and *b*). Additionally, there is a low recombination rate directly between both dislocation bands (*g*). The total recombination rate is given by the sum of the recombination through the dislocation valence band and the deep level,

the bulk valence band and the deep level, and the recombination between both dislocation bands.

If one considers a n-type material, then the recombination of minority holes at negatively charged dislocations occurs in a sequence of three steps:

- Diffusion of holes from bulk, where the holes are generated, to the border of the space charge region.
- Capture by the space charge around the dislocation and drift to the dislocation core.
- Capture at the shallow band or by the deep states of the metal impurity and then recombination with electrons, present at the dislocation.

The EBIC contrast depends on the temperature, T, the deep level energy, E_m, the linear density of impurity states at the dislocation, N_m, the capture cross section for electrons, σ_n, and holes, σ_p, and on the coupling between the dislocation and the impurity level, α:

$$c_c = c_c(T, E_m, N_m, \sigma_n, \sigma_p, \alpha). \qquad (1.20.)$$

The parameter α accounts for the interaction between the deep level and the one-dimensional dislocation bands. It characterises the overlap between the electron wave functions of the deep acceptor with those of dislocation bands and may vary from 0 (no overlap) to 1 (fully overlapped).

The enhancement of the recombination activity of the metal as well the dislocation is due to combined action of both defects. The dislocation is responsible for the capturing of the carriers at one-dimensional bands and recombination occurs at the centres induced by the impurity atoms.

A direct relation exists between the impurity line density at the defects, N_m, and the dislocation activity. Based on the EBIC results one can estimate the concentration of centres at the dislocation. Two diagrams from [Kve2001], which are used in this work to estimate the line density of the metals at dislocations, are shown in Fig. 1.5. It is assumed that deep level beneath the conduction band at E_C-E_m=0.5eV interacts with a dislocation. The capture cross sections are taken to be σ_n=2x10^{-15} cm^2 and σ_p=10^{-14} cm^2 for the electrons and holes, respectively [Kve2001]. Fig. 1.5a presents the dependence of the EBIC contrast on the temperature for several different coupling parameters α for relatively strong contaminated dislocations (N_m=3x10^7 cm^{-1}). The values of the varied parameter are given close to the corresponding curve. As seen in Fig. 1.5a, without interaction between the deep level and the dislocation (dotted line) the contrast is determined mostly by the recombination through the deep state. The contribution of the recombination through the dislocation bands is small and only at low temperature. For strongly decorated dislocations even a small overlap of the wave

functions between the deep state and the dislocation bands ($\alpha << 1$) results in a significant increase of the low temperature contrast of the dislocation. Upon increasing the overlap, the change in the contrast becomes detectable at room temperature.

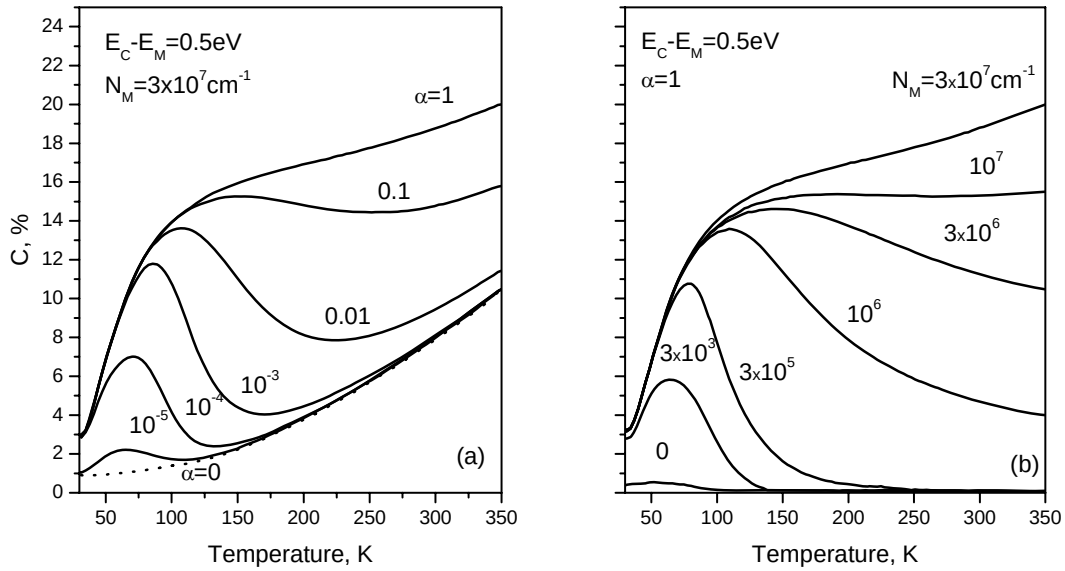

Figure 1.5. Temperature dependence of EBIC contrast behaviour. a) Strong coupling between the dislocation bands and the deep level, leads to high dislocation activity. b) The concentration of the deep centres at the dislocation is decisive for the dislocation activity. Upon increasing their concentration the dislocation recombination behaviour evolutes from active at low temperature (Type II) to active at room temperature (Type 1). (Diagrams after [Kve2001])

Figure 1.5b shows the evolution of the temperature behaviour of the contrast upon increasing the metal concentration at the dislocation at strong coupling between the dislocation and the deep level (α = 1). All possible types observed experimentally can be described. The model gives a quantitative access to estimate the contamination level of the dislocations. However, it does not allow to make conclusions about the position of the deep level in the band gap. Although it predicts changes in the contrast v/s temperature behaviour related to the deep level energy, E_m, the energy position gives impact only in a limited range of values of the other parameters. The small influence of the impurity level position in the band gap on the contrast behaviour of the dislocation is related to the capture properties of the dislocation. The temperature mostly influences the population of minority carrier in the dislocation bands, whereas the deep level provide only a means for their recombination and is not affected in the same extend by the temperature. This weak dependence on E_m is consistent with the experimental observation, where the nature of the transition metal used for contamination does not play a role for the contrast behaviour and the major impact is the due to the concentration of the metal at the dislocation line.

In contrast to the *total* recombination rate, the *radiative* recombination rate at dislocations has been found always to decrease upon increasing temperature [Kve1996, Kve1995, Sue1983a].

1.4. Temperature dependence of dislocation-related luminescence

There are mainly two models which are used to describe the temperature roll-off of the dislocation radiation intensity. The *bound-to-free* or the *bound-to-bound deactivation* models, which describe the deactivation of a carrier trapped at a radiative centre into a semiconductor three-dimensional band or into another bound state, respectively. The temperature roll-off due to *bound-to-free deactivation* is given by the following relation [Saue1985, Sue1983a]:

$$\frac{I(T)}{I(0)} = \frac{1}{1 + C\,T^{3/2}\exp(-E/kT)} \tag{1.21.}$$

where *I(T)* is the height of the luminescence peak at temperature *T*, *I(0)* is that extrapolated to zero temperature, and *k* is the Boltzmann constant. The term $CT^{3/2}$ is proportional to the degeneracy factor of the bound state and the density of states in the band, and *E* is the deactivation energy.

In *bound-to-free deactivation* model, it is assumed [Sue1983a] that two (non-degenerated) levels at the dislocation (Figure 1.6a), one being shallow and the other deep are responsible for the recombination at the dislocation. These two levels are occupied one by holes and the other by electrons. For sake of convenience let us assume electrons are populating the shallow level and the holes the deep one. Due to the injection of carriers the system is not in thermal equilibrium and the occupations statistics is described by the use of quasi-Fermi levels for electrons and holes. One can assume that both quasi-Fermi levels are close to the conduction, E_C, and valence, E_V, band edges and thus the deep level should not change its population (Fig. 1.6a). Let us assume, that a shallow trap, E_D, is close to the Fermi level, F_n, and its population probability is given by:

$$f = \frac{1}{1 + \exp\left(\frac{E_D - F_n}{kT}\right)}. \tag{1.22.}$$

The local density of electrons, *n*, in the conduction band, generated by the excitation in the vicinity of the shallow trap is related to the quasi-Fermi level by:

$$n = N_C \exp\left(\frac{F_n - Ec}{kT}\right), \tag{1.23.}$$

where, N_C is the effective density of states in the conduction band. Combining (1.22) and (1.23) and taking into account the temperature dependence of N_C ($N_C = N_{C0}\,T^{3/2}$, N_{C0} is a

constant, determined by the effective mass of the carriers in the band[1]) one gets the following expression for the population probability of the shallow level:

$$f = \frac{1}{1+\left(\frac{N_{C0}}{n}\right)T^{3/2}\exp\left(\frac{E_D - E_C}{kT}\right)}, \qquad (1.24.)$$

Relation (1.21.) is obtained by substituting the activation energy $E = -(E_D - E_C)$ and $C = N_{C0}/n$. The local density of electrons, n, is regarded constant, determined primary by the excitation. The probability for recombination is proportional to the population probabilities for both traps. Because only the occupation of the shallow one is influenced by the temperature, its population probability temperature dependence determines that for the entire process.

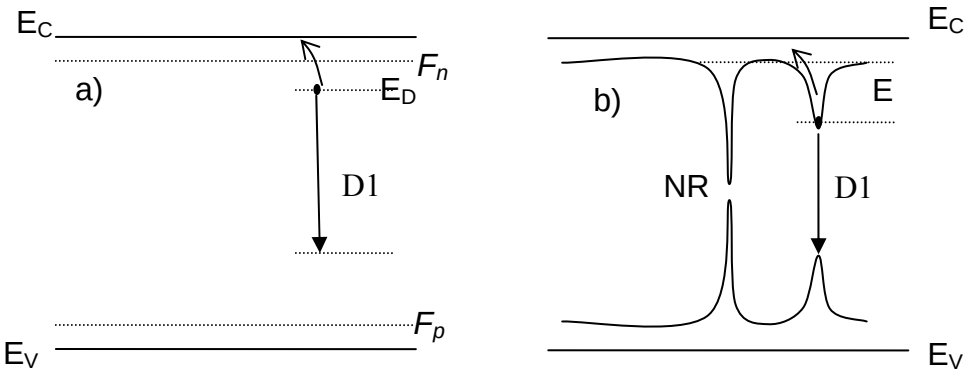

Figure 1.6. Temperature roll-off of dislocation-related radiation (e.g. D1) a) Deactivation back into the conduction band. The quasi-Fermi levels F_n and F_p are indicated. b) Deactivation and recombination through a nonradiative centre (NR). The carriers need to overcome a barrier E to reach the nonradiative centre.

The *bound-to-bound deactivation* model [Saue1985, Pan1975] can be adopted to describe the deactivation of dislocation-related radiative centres, assuming that in its vicinity nonradiative centres (NC) exist and the energy released due to recombination is transferred by multi-phonon or Auger processes (See section 1.2). Similar model has been used in [Pan1975] to explain the cathodoluminescence behaviour of microscopic inclusions and defects in direct gap semiconductors.

In case of extended defects it can be interpreted as a competition between radiative and nonradiative recombination of carriers captured in centres responsible for the dislocation radiation.

Let us assume that a carrier is captured at a centre responsible for dislocation-related luminescence (e.g. D1) (Figure 1.6b). A deactivation is possible, in which the carrier

[1] N_{C0} is the temperature independent term in the expression for the density of states in the conduction band $N_{C0} = 2\left(\frac{2\pi m_e k}{h^2}\right)^{\frac{3}{2}} M_c$, where m_e is the effective mass of the electrons M_c the number of equivalent minima in the conduction band, h and k are Boltzmann's and Planck's constants, respectively.

overcomes a potential barrier, E, and becomes captured at a nonradiative recombination centre (NR). It is supposed that the recombination at that centre is nonradiative and independent on the temperature. Thus, the probability, P_{nr}, to reach the nonradiative centre and to recombine there is given by:

$$P_{nr} = P\exp(-E/kT), \tag{1.25.}$$

where P is the nonradiative decay probability. If one assumes that the probability for radiative recombination, P_r, is also not dependent on temperature, then the dependence of the intensity ratio is given by the relations:

$$\frac{I(T)}{I(0)} = \frac{P_r}{P_{nr} + P_r} \text{ and thus} \tag{1.26.}$$

$$\frac{I(T)}{I(0)} = \frac{1}{1 + C'\exp(-E/kT)} \tag{1.27.}$$

where C' is a constant, accounting for the radiative and nonradiative transition probabilities, and E is the deactivation energy of a radiative centre.

A model, related to the band structure of the dislocations, with energies influenced by the presence of impurities at the dislocation line has been introduced by Kveder et al. [Kve1996, Kve1995]. It describes the temperature behaviour of one of the specific fetures of the dislocation-related luminescence (D4), assuming that radiative transition occurs between the one-dimensional dislocation bands $E_V + E_{Dv}$ and $E_C - E_{Dc}$. Here E_{Dv} and E_{Dc} are the split off energies of the bands corresponding to the straight parts of 60° dislocations, from the valence, E_V and the conduction band E_C, respectively. It is also assumed that the dislocation one-dimensional band has a mobility edge E_{mob}, which electrons reach by thermal activation from the dislocation band, overcoming a barrier E_{mob} (See Fig. 1.7). The intensity of the dislocation luminescence is then given by:

$$\frac{I(T)}{I(0)} = \frac{1}{1 + C_1\exp(-E_{mob}/kT) + C_2 T^{3/2}\exp(-E_{Dc}/kT)}, \tag{1.28.}$$

where C_1 and C_2 are temperature independent constants.

Temperature roll-off of D4 occurs when e.g. electrons are activated to the mobility edge of the dislocation or to the semiconductor valence band. After that they can move along the dislocation band until captured by nonradiative centre, or reemitted in the conduction band. The second term in the denominator describes the activation of the carriers to the mobility edge of the dislocation band. The authors presume that the barrier, E_{mob}, usually of order of 4 - 7 meV originates from weak modulation of the one-dimensional band due to point defects in the vicinity of the dislocation. The deep recombination centres are at the dislocation core and serve

as recombination sink for the electrons, moving along the dislocation. The third term in the denominator of (1.28.) accounts for the reemission of the electrons from the dislocation band, directly back to the conduction band.

Relation (1.28) describes the temperature dependence of D1 intensity, too [Kve1996]. It is anticipated that the direct deactivation, of D1 centre by reemission back to the conduction band is accompanied by a reemission to the mobility edge of the dislocation. Instead of E_{Dc} the value E_{Dc1} is obtained, which characterises the depth of the D1 electron trap.

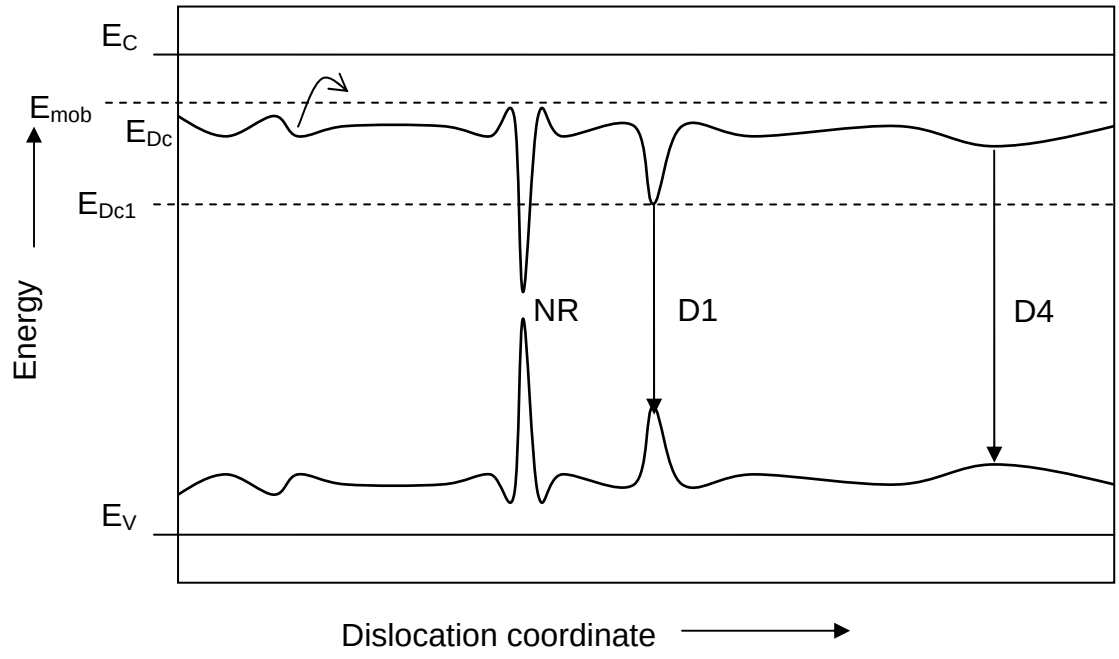

Figure 1.7. Illustration of possible electron transitions between the shallow dislocation bands. The electron can recombine producing a D4 or migrate along the dislocation until trapped at nonradiative recombination centre (NR), or migrate to D1 centre, or can be emitted back to the conduction band.

1.5. Summary

The recombination processes in dislocated silicon are governed by SRH, Auger, Radiative band-to-band recombination, and radiative and nonradiatiuve recombination at the dislocations. The recombination at a dislocation is strongly influenced by the presence of metallic impurities at the dislocation sites. It can either decrease or increase with temperature, depending on the degree of contamination. In contrast to the total recombination rate, the *radiative* recombination on defects as well *band-to-band* luminescence exhibit a decrease upon increase of the temperature. The defect luminescence temperature quenching is related to a depopulation of the shallowest level involved in the radiative transition. Information about the position of the defect levels in the band gap caused by dislocations can be obtained by analysing the temperature dependence of the dislocation luminescence intensity.

Chapter 2

Dislocation-related radiation

In this chapter, the dislocation radiative properties are reviewed. The possible origin and the relation between the dislocation lines are discussed based on literature data.

Radiation activity of the dislocations has been first reported by Drozdov et al.[Dro1976]. It consists of a quartet of lines (D1, D2, D3 and D4) with energies in the sub-band gap energy range of silicon: D1(0.8 eV), D2(0.87 eV), D3(0.94 eV) and D4(1.0 eV) (Fig. 2.1).
Narrow lines indicate bound states. Bound states for charge carriers at the dislocations can be caused by three major factors:

1) mechanical strain or long-range electrical interaction;
2) dangling bonds, structural imperfections and defects in the dislocation core;
3) impurities and defects in the vicinity of the dislocations.

The experimental efforts are usually directed to distinguish between these factors.

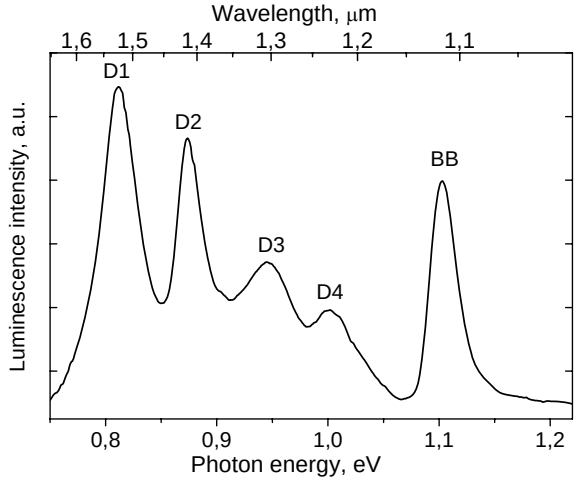

Figure 2.1. Typical spectrum obtained from plastically deformed silicon sample at 80K. Dislocation lines (D1-D4) and band-to-band (BB) radiation.

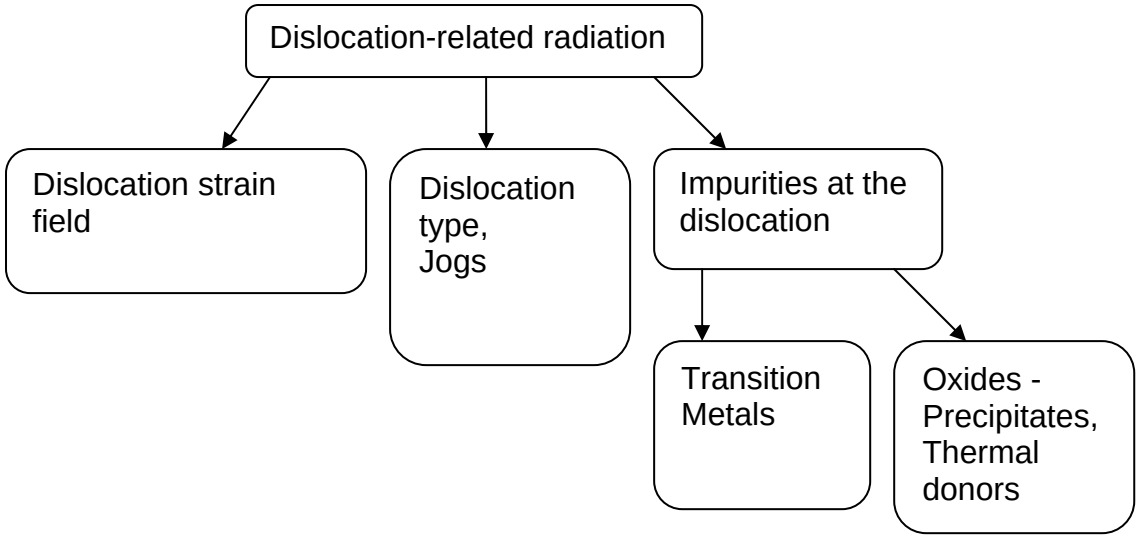

Figure 2.2. Possible origin of the dislocation radiation.

2.1. Origin of the dislocation luminescence

The spectrum of dislocation-related luminescence has been subject of many studies but the exact mechanism is still unknown. The optical activity of the dislocations can have different origin. Levels in the band gap of silicon can be formed due to the strain field caused by the lattice distortion around the dislocation, structural defects at the dislocation like kinks and jogs or due to impurity atoms captured at the dislocation strain field, either in the vicinity or at the core of the dislocation (Figure 2.2).

2.1.1. Dislocation strain field and dislocation type

A long-range strain field is an inherent property of the dislocation, and is not influenced by the impurities or the core structure. It causes the formation of one-dimensional energy bands, which are related to the Burgers vector of the dislocation [Lel1992]:

$$E = Eg - A\left(\frac{b_e}{a}\right)^2 , \qquad (2.1.)$$

where E is the energy of the radiation Eg is the silicon band gap, a - the lattice constant, A is a constant accounting for the deformation potential and the effective mass of the carriers and b_e is the edge component of the Burgers vector of the dislocation. For silicon, the constant A is estimated to about 800 meV.

Accordingly, Lelikov et al. [Lel1992] estimated the band-gap modification for different dislocation type and compared it to the known spectral features (Table 2.1).

Dislocation Type	*b/a*	E estimated, eV	E observed, eV
Screw non-split	½[110]	0	
30° partial glide	1/6 [210]	1,140	
Stair-rod partials	1/6 [110]	1,125	1,030
90° partial glide	1/6 [112]	1,040	1,025
Frank Partial	1/3 [111]	0,900	0,870(D2)
60° -non-split	½[101]	0,870	
Lomer-Cotrell	½[110]	0,770	0,807(D1)

Table 2.1. One-dimensional band gap, formed due to the strain field of the dislocations. The D4 (1.000eV) line was associated with a 90° partial of a dissociated 60° dislocation and an equilibrium stacking fault of 50 nm width. [Lel1992]

Other authors have supported the assumption that the distinct dislocation features in the spectrum are related to the dislocation type, too. Thus Sekiguchi et al. [Sek1994, Sek1996] demonstrated spatial correlation between the dislocations related lines and specific morphological formations after plastic deformation of silicon crystals. D1 and D2 lines are dominant in regions of intersection of slip lines, whereas D3 and D4 lines are detected along the slip lines. Thus D3 / D4 are attributed to glide dislocations and D1 / D2 to the reaction product of dislocations, namely Lomer-Cottrell dislocations or jogs.

2.1.2. Dislocation structural defects

Jogs are formed either by dislocation climb (change of the dislocation glide plane due to interaction with three dimensional crystal defects) or by the intersection of two dislocations in different glide plains, at the crossing nodes. Jogs as an origin of D1 were pointed out by Ikeda et al. [Ike1998]. To avoid slip systems and the glide dislocations there, the authors produced artificial grain boundary by direct bonding of two (100) oriented wafers. The dislocations in the specimens were identified as screw dislocations at intervals of about 200 nm, compensating a twist angle of about 0.1° between the wafers. Cathodoluminescence measurements at 18K showed only band-to-band emission and D1 luminescence, from the grain boundary and no other dislocation-related lines were present. The authors attributed the D1 emission to jogs, generated at the intersections of the two sets of screw dislocations. The absence of D3 and D4 was related to the absence of glide dislocations, which according to [Sek1994, Sek1996] should be the origin of these two peaks. TEM imaging showed the presence of oxygen precipitates at the interface between both bonded wafers, but their possible role for the dislocation radiation was not discussed.

Jogs as origin for D1 and D2 luminescence were also suggested by Shevchenko and Izotov [Sch2005]. It was discussed, that D2 originates on jogs formed on 60° dislocations and D1 on edge type jogs formed on screw dislocations.

2.1.3. Straight 60° dislocations, D3 and D4

In tetrahedrally bonded semiconductors the most frequently occurring dislocations are the 30° and the 90° partials, lying on {111} planes along [110] directions, resulting from the dissociation of 60° dislocations. Deep level transient spectroscopic studies (DLTS) on plastically deformed (700°C) p-Si reveal a band around Ev+0.47 eV which was correlated with the presence of dislocation-related radiation [Fek1999]. The density of the centres, ~ 10^{12} cm^{-3}, in samples containing $5x10^5$ cm^{-2} dislocations, corresponds to an upper limit of about one state per ten spacing along the dislocation line. Such high density rules out jogs, as a source of the dislocation radiation in the plastically deformed material.

Woronek et al. [Wor1992] ruled out the Lomer-Cotrell dislocations (formed by the combination of two 60° dislocations out of different glide systems) as origin of the D1 /D2 luminescence. The dislocation radiation is a dipole transition with electric field vector oriented parallel to Burgers vector of the dislocation. Thus, the dislocation luminescence shows pronounced linear polarisation when the dislocations are predominantly oriented in one direction. In samples, where the dislocations are formed by plastic deformation such preferable orientation of the Lomer-Cotrell dislocations can be achieved. It was found that the polarisation of the D1/D2 radiation does not mach the orientation of the Burgers vectors of the Lomer-Cotrell dislocations and thus the luminescence cannot be attributed to transitions related to this dislocation type.

Thus the origin of the D luminescence should be looked for in 90° and 30° partials of 60° dislocations [Nun1998, Che1984, Rab1993, Blu2001]. Models of dislocation electronic structure, based on a continuous media approach and an empirical approximation for the deformation potential and effective mass [Rab1993] show that one-dimensional bands are formed at the dislocation, with band-gap reduced by several tens meV. The core structure of the dislocations is reconstructed forming a single or a double period and deep states do not arise from any of the partials. The high energetic features in the spectrum (D3 and D4) can be related to the one-dimensional dislocation bans. However, the absence of deep stats in the band structure of the dislocations does not allow to explain the appearance of the low energetic D1 and D2. They must be related to defects trapped at the dislocation.

2.1.4. Role of oxide precipitates

Formation of oxide precipitates in silicon is accompanied by injection of interstitials and formation of "punch out" dislocations. Relations have been suggested between the dislocation luminescence and over coordinated oxygen, interstitial clusters at the dislocation [Piz2000, Piz2000a, Piz2001], or donor acceptor recombination between oxygen related donor centres and dislocation acceptor states [Ste2005]. The role of oxygen in silicon for the dislocation radiation was studied by comparison of dislocated samples prepared on materials grown by float zone (FZ) or Czochralski (CZ) growth techniques. The main difference between both techniques is the content of interstitial oxygen in the final crystal. Thus for CZ material the oxygen is about 10^{18} cm^{-3} and in FZ is less than $10^{16}cm^{-3}$.

Dislocations are acting as gettering sites for oxygen, as shown by Cavallini et al. [Cav1993]. The relation of oxygen with the dislocation luminescence was initially pointed out by Drozdov et al. [Dro1981], who showed, that the formation of an oxygen atmosphere around dislocations by heating of oxygen rich ($5x10^{17}cm^{-3}$) CZ samples at 750°C, induces a broadening of the D1 line in the photoluminescence spectrum. Studies of the luminescence generated by oxide precipitates [Taj1992] reveal that the D1 and D2 bands broaden and shift downwards in energy with increasing temperature leading to a room temperature peak at 0.77 eV.

The influence of oxygen in the substrates on the dislocation radiation D1/D2 was also studied by Pizzini et al. experimentally [Piz2000, Piz2000a, Piz2001]. The luminescence in the range 0.7-0.9 eV was attributed to the presence of oxide precipitates or to so-called thermal donors (TD), which form in oxygen rich silicon at 470°C anneal. The authors associated D1/D2 luminescence with the properties of the interface between the oxide precipitate and silicon matrix and with recombination centres arising from over-coordinated oxygen. Generation of self-interstitials around oxide precipitates during their nucleation and growth was also considered as being involved in the formation of centres responsible for dislocation radiation. The self-interstitials excess leads to the formation of interstitial clusters at dislocation cores and thus, to luminescence in the range 0.8- 1.0 eV, according to theoretical predictions [Blu2001, Blu2000, Jon2000]. Complexes of 3 and 4 interstitial atoms (I_3 and I_4, respectively) bound at the 30° and 90° dislocation partials. The clusters strongly perturb the dislocation band structure and cause the appearance of occupied states in the lower and unoccupied states in the upper quarter of the band gap. The energy positions of the dislocation-bound I_3 and I_4 related states are similar to those of isolated clusters. Although interstitial defects show luminescence, generally, at about 1eV (W and X line) [Ter1997], the D1 radiation can be explained by a

transition between a one-dimensional band at the dislocation and a state caused by the interstitial cluster, resulting in a reduced energy of about 0.8 eV.

To account for the resulting D1-line broadening and shift upon increasing excitation power, a coupling between TD and dislocation acceptor states was suggested [Ste2005]. The growth of oxide precipitates in initially dislocation free samples of CZ silicon is associated with appearance of distinct features in the luminescence spectrum in the range of 0.8-0.92 eV [Bin2002]. Despite oxide precipitates show an emission in the energy range of D1 and D2, their luminescence cannot be associated with dislocations. The luminescence from oxide precipitates does not depend on their size and shape. Upon precipitate growth, dislocation and stacking faults are formed. Dislocation-related lines D3 and D4 were detected only after stacking faults and dislocation half loops appeared due to the precipitates growth. Typical dislocation-related lines D1-D4 were observed only on samples with dislocations formed by plastic deformation or when dislocations punch out from the precipitates.

Nano precipitates at high concentrations formed by high pressure isostatic annealing of CZ silicon [Bin2003] exhibit luminescence at about 0.8 eV (~ D1).Although, that radiation is strongly suppressed in presence of dislocations [Bin2002, Bin2003]. The D1 emission and the radiation related to oxide precipitates are substantially different and D1 cannot be explained by luminescence from oxygen precipitates.

2.1.5. Role of transition metals

A contamination with a small amount of metals is unavoidably present in silicon materials of all types. The background contamination with transition metals can play a decisive role for the dislocation radiative recombination activity. The role of small concentrations of transition metals (Cu, Ni, Fe, Ag and Au) for the D1 and D2 radiation has been studied by Higgs et al. [Hig1992]. High purity, FZ material with a residual concentration of transition metals below $10^{11}cm^{-3}$ was used in order to prevent background contamination of the dislocations. Dislocations were introduced by formation of epitaxially grown stacking faults (ESF) or stacking faults formed by oxidation (OISF). It was found that neither ESF nor OISF emit D radiation in non-contaminated samples. Thermal treatment in clean condition also does not lead to the appearance of D lines. Only after intentional contamination with transition metals the dislocations emissions of D1 and D2 lines occur. An optimal metallic concentration exists at which the dislocation radiation is maximal and no precipitation of the metals occurs. At high concentration of metallic impurities, precipitation at the dislocations is observed and the D lines are almost not present. The dependence of the intensity of D1 and D2 on the metal contamination in terms of surface concentration is shown in Figure 2.3. This behaviour is

characteristic for most of the transition metals. However, exceptions are found for gold and platinum. Both metals influence predominantly the D1 radiation, and D2 is not present. A broadening of the low energy side of the D1 line and an additional feature, 50 meV below the D1 peak has been observed on samples containing OISF after diffusion of gold or platinum [Pea1989].

The transition metals induced enhancement of dislocation radiation was also observed in silicon germanium mixed crystals. It was found that the contamination with Cu favour the formation of misfit dislocations [Hig1991]. Additionally, in presence of Cu contamination, the typical D band luminescence observed from such samples was enhanced [Hig1990, Hig1993].

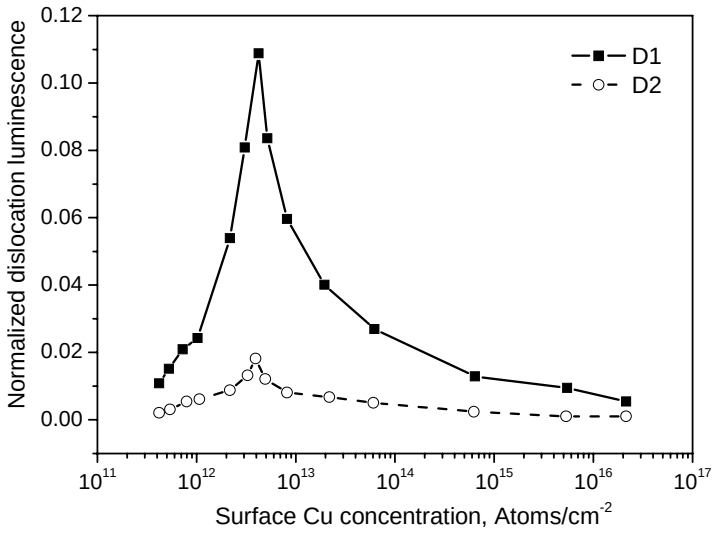

Figure 2.3. Dependence of the D1 and D2 intensities on the surface concentration of Cu. The dislocation luminescence peaks are normalized on the phosphorous bound-exciton peak, which appears close to band-to-band one in the spectra. The Cu contamination was controllably introduced into the sample surface. (After [Hig1992])

Though it has been well established that the transition metals influence the dislocation radiative properties, their role has been differently interpreted. It has been suggested that metals can passivate the nonradiative recombination centres at the dislocations and thus the recombination through D1centre is increased [Sek1994, Sek1996, Lel1992]. Such explanation implies that the dislocations, free of metals would show strong nonradiative recombination and upon decoration the metals would decrease the total recombination activity of the dislocations. Such behaviour is in contrast with the observation in [Kit1993c, Hig1993a]. Dislocations in clean, as grown samples show low recombination activity, while contaminated dislocations show high recombination activity and D luminescence. Such correlation between the total recombination activity and radiation from the dislocation has been demonstrated [Hig1993a].

In conclusion, a passivation of nonradiative recombination centres due to contamination with metals cannot explain the origin of the dislocation radiation. The transition metals have to be considered as directly involved in the mechanism of the D1 and D2 radiation.

2.2. Relation between the dislocation lines

Although the origin of dislocation radiation is not known, relations between the D lines have been observed. The lines D1 and D2 and respectively D3 and D4 are commonly considered as pairs, because of their similar behaviour upon varying external parameters. The similar responses of the lines to uni-axial stress, excitation level, alloy composition in SiGe, time and temperature decays and spatial correlation are reviewed below.

2.2.1. Energy shift of the dislocation-related lines upon application of uniaxial stress

The peak position shift upon externally applied uni-axial stress on the samples gives information about the symmetry of the radiative centre and its piezo-optical constant. Drozdov et al. [Dro1977] found a shift of the D lines upon subjecting the samples on compression along the <111>, <110> and <100> crystallographic directions. D3 and D4 shift to lower energy, following the change of the band gap of silicon. The influence on the spectra around D1 and D2 shows different behaviour. Both lines are significantly shifted towards higher-energy. It has been found, that the piezo-optical constants are equal for D1 and D2 and the same holds for D3 and D4. In the similar experiments, the authors of [Sue1982, Sue1983, and Saue1985] found a splitting of the D1 and D2 lines in two components each. For all stress directions the splitting and the shift of D1 has been observed to be practically identical with that of D2. Both components of the splitting have different sign of their piezo-optical constants. One of them shifts to higher energy [Dro1977] and the other to lower. The splitting has been explained by a centre with tetragonal symmetry, responsible for the D1 and D2 emission. The similar behaviour of D1 and D2 on the one hand as well D3 and D4 on the other hand upon uni-axial stress allows to treat them as pairs.

2.2.2. Comparison of the radiative decays

The radiative lifetime of all four dislocations related lines in the nanosecond time domain was studied by Fukatsu et al. [Fuk1996] in a wide temperature range. They investigated misfit dislocations formed in undoped SiGe alloy layers with a Ge content of 10%, grown on p- type silicon.

It was found that the temporal decay profiles of the lines in the pairs D1/ D2 as well D3/ D4 are similar. The decay time estimated for D1/D2 was estimated to 0.2 - 0.35 μs at 9 K. Much shorter decay time (37 – 46 ns) was obtained for D3 and D4 lines. However, the radiative lifetimes are essentially different from the decay times, whereas the latter characterize the decay through the radiative and the nonradiative routes the former only accounts for the radiative processes. The radiative lifetime is then proportional to the decay time and inversely proportional to the intensity of the line. Taking into account the change in intensity of dislocation-related luminescence in the temperature range 9 – 100 K the authors estimated the temperature behaviour of the radiative lifetimes associated with the centres responsible for D1/D2 and D3/D4 emission. It was found that the radiative lifetime of D3/D4 does not depend on the temperature, while that for D1/ D2 increases with the temperature.

According to the similar temperature behaviour of the radiative lifetimes, the D1 and D2 as well as D3 and D4 can be again regarded as pairs.

2.2.3. D lines in SiGe and their dependence on alloy composition

The energy shift of the dislocation-related luminescence in Si_xGe_{1-x} alloys upon varying composition x was studied by J. Weber and M. Alonso [Web1990] in the whole range of possible x ($0 \leq x \leq 1$). Dislocations resulting from the lattice mismatch between the SiGe layer and the silicon substrate were found to emit all dislocation characteristic lines in the interval of Ge content from 0% to 50%. Above 80% Ge, only one dislocation-related line was observed, which is characteristic for the dislocations in Ge [New1957]. D3 and D4 shift to lower energy proportionally to the Ge content in the range 0 to 80 %. The energy separation between D3 and D4 was found to correspond to the transversal optical phonon energy of the corresponding alloy composition. However, the behaviour of D1 and D2 differs from that of D3 and D4. D1 and D2 exhibit no energy shift up to 20% Ge in the alloy. Thus one can conclude, that initial and the final state of D1 and D2 transitions exhibit an energy separation, which is independent on the band gap shrinkage, caused by the presence of Ge in the alloy. The authors suggested that an internal transition between deep levels would account for such behaviour. At higher compositions both lines show similar shift to lower energy, but the slope is different from those of D3 and D4. Because of the energy separation between the peaks D1 and D3 were assigned to phonon replicas of the D2 and D4 bands, respectively.

2.2.4. Dependence on the excitation power

The intensity of the dislocation luminescence depends on the excitation level, i.e. on the excess carrier density generated by excitation. It was found [Sue1983a] that the intensity of the

dislocation-related lines D1 and D2 show sub linear dependence on the excitation level, while D3 and D4 intensities are proportional to it. At elevated temperatures, the dependence of D1/D2 on the excitation level becomes weaker and the intensities of both peaks show a tendency of reaching saturation at high injections.

The effect can be related to the observed difference in the temperature dependencies of the radiative lifetimes of D1/D2 and D3/D4 [Fuk1996]. Although, the decay times for both D1/D2 and D3/D4 decrease, the radiative lifetime for D1/D2 increases with temperature, while that for D3/D4 remains constant (See 2.2.2).

2.2.5. Temperature dependence of the dislocation lines intensities

The temperature dependence of the luminescence lines D1 through D4 has been usually measured in the range from 4.2 K up to 200 K. The temperature roll-off rates of D line intensities measured in different studies are rather scattered. Thus Fukatsu et al. [Fuk1996] found all four lines have similar temperature roll-off and thus are equally susceptible to the nonradiative pathways.

Suezawa et al. [Sue1983a] found similar temperature behaviour only for D4 and D3 with deactivation energy of about 4.2 meV. D1 and D2 lines showed different temperature behaviour and their deactivation energies were different - 7.0 and 4.5 meV, respectively.

Kveder et al. [Kve1996, Kve1995] studied temperature quenching of heavily dislocated silicon in a range between 5 K and room temperature. The activation energies obtained in their studies differ significantly from those reported in the other works. The D1 activation energy was estimated to 165 meV and that for D4 to about 95 meV.

Although the studies cited previously in this section confirm the similar temperature dependence of D1 and D2 as well that for D3 and D4, there are experimental findings which disprove such correlation. Thus Sauer et al. [Saue1985] found that D1 and D3 remain virtually constant up to 20 K, while D2 and D4 showed a gradual decrease.

2.2.6. Spatial distribution

For a characterisation of the spatial distribution of luminescence centres around the dislocations, luminescence studies with a very high lateral resolution are necessary. Cathodoluminescence is capable of detecting the luminescence of individual dislocations and slip lines. Higgs et al. [Hig1992a] found that D3 and D4 lines originate at the dislocation core and D1 and D2 lines appear in the vicinity, 2-9 μm away from the dislocations. Similar observation was reported by Sekiguchi et al. [Sek1996]. The cathoduoluminescennce images of

D1 and D2 are always similar to each other on all kinds of specimens studied. The same observation is valid for the images of D3 and D4.

2.2.7. Phonon replica relation between D1-D2 and D3-D4

The correlation between D1 - D2 and between D3 – D4 has been observed in many studies. Meanwhile it is accepted that at D3 is a phonon replica of D4. According to Woronek et al. [Wor1992] the energy separation between D3 and D4 is identical to the energy separation between bound-exciton transitions mediated by one transversal optical (TO) phonon (BE^{TO}) and no-phonon transition (BE^{NP}). Thus, D3 is considered to be TO phonon replica of D4, and the larger width of D3 line when compared to D4 is explained by the small energy differences between the three, momentum conserving TO phonons, which cause three replicas slightly different in their energy. The energy separation between D1 and D2 was observed to be bigger than the energy of the TO phonons and that is why D1 was assigned to a phonon replica of D2 with optical phonon at the centre of the Brillouin zone (O^{Γ}).

2.3. Dislocation luminescence on non-relaxed dislocations

Other lines D5, D6 and D12 in the sub-band-gap energy range were associated with dislocations, too [Saue1985, Saue1986]. They were attributed to non-relaxed dislocations, produced by two-step deformation. The three new lines D12 at 1.468 µm (0.8443eV), D5 at 1.3µm (0.953 eV) and D6 at 1.224 µm (1.0126eV) were observed after a two-step deformation of FZ silicon samples. The deformation procedures included a predeformation at high temperature and low stress step (650 °C, ~ 30 MPa), followed by a second compression step at low temperature and relatively high stress (420 °C, ~300 MPa). After relaxation by low temperature annealing (300°C), the lines transformed into usually observed D1/D2 and D3/D4.

2.4. Summary

The dislocation radiation consists of four lines D1–D4. D3 and D4 are generated by transition between one-dimensional dislocation bands on 60° dislocations. In comparison to D3 and D4, the origin of D1 and D2 is less clear, but they are most probably caused by the interaction of the dislocations with background metallic impurities. There is a relation between the lines D3 and D4, and D3 is a phonon replica of D4. In case, D1 and D2 are simultaneously present, there is a relation between both lines. However, it is possible to observe only a single line D1 without presence of D2.

Chapter 3

Experimental methods and investigated materials

This chapter gives a brief description of the applied experimental techniques and typical characteristics of the materials, which are studied.

To study the dislocation activity in silicon a variety of techniques for sample preparation and different methods for characterisation can be applied. Many aspects have already been presented in Chapter 2. In this work, mainly three techniques were used for characterisation of the radiative and nonradiative recombination properties of samples, containing dislocations. These are photoluminescence spectroscopy and mapping, EBIC mapping, and minority carrier diffusion length measurement based on the spectral response of the light-induced-current in samples with p-n junctions. A short overview of the construction details of photoluminescence apparatus and the basic principles of the methods for electrical characterisation is given below. In order to correlate the recombination activity at the defects with their luminescence properties different samples were analysed. The principles of the preparation methods and the typical characteristics of the obtained materials are briefly described.

3.1. Luminescence in silicon

The luminescence spectroscopy is a technique, which is commonly used to study defects in semiconductors. Although the interpretation of luminescence spectra can be quite complicated, the basic concept of how it works can be explained using conservation of energy and momentum.

Silicon is an indirect band gap semiconductor, which means that its conduction band minimum and valence band maximum occur at different positions in reciprocal space, as shown schematically in Figure 3.1. When light with energy $h\nu > E_g$ (band gap) is incident on a semiconductor it can be absorbed, exciting electron to the conduction band and leaving a hole in the valence band. The electron in the conduction band and hole in the valence band are referred to as an electron hole pair. After the electron hole pairs are excited, they will recombine in order to obtain a lower energy state. This recombination can occur via a variety of paths, the simplest of which is band-to-band recombination.

Let us consider the case where an electron moves from the conduction band to a state within the gap. As the electron makes this transition, it loses energy.

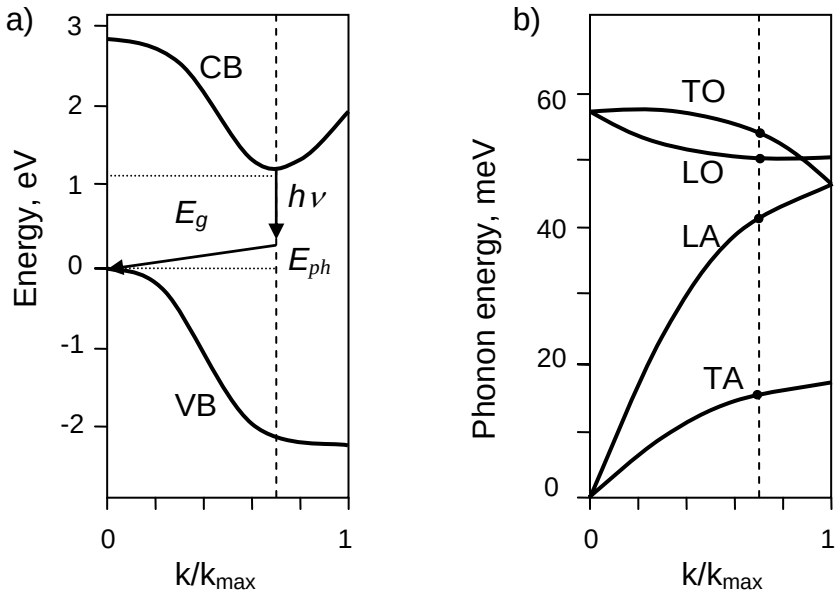

Figure 3.1. Luminescence in silicon. The band-to-band transition is mediated by a phonon. Schematic representation of (a) band structure and (b) phonon dispersion diagram. [Lig1990]

The energy must be transferred to some other particle, typically either a photon or a phonon. Transitions that emit photons are referred to as radiative processes, and transitions that generate only phonons are nonradiative processes. There are transitions, which involve both phonon, $E_{ph,}$ and photons, $h\nu$, as it is the case by radiative band-to-band transition in silicon. The energy of the resulting photon is given by:

$$h\nu = E_g - E_{ph} \tag{3.1}$$

By excitation at low temperatures, the effects of Coulomb interaction between the carriers lead to reduction of the energy of the emitted photons. In case of free excitons, formed by the interaction of a free hole and a free electron in the conduction band, the energy of the resulting photon by recombination becomes reduced by the binding energy of the exciton, E_z.

$$h\nu = E_g - E_{ph} - E_z \tag{3.2}$$

The exactions may become bound to neutral donor or acceptor, forming bound excitons. The emission energy from bound excitons is reduced, by the binding energy of the excitons, E_b, to the donor or acceptor which is about 1/10 of their ionisation energy [Lig1990]:

$$h\nu = E_g - E_{ph} - E_z - E_b \tag{3.3}$$

At very high excitation densities the electrons and holes condense into a plasma, referred as electron-hole droplets [Lig1990]. They give rise to a broad luminescence, due to recombination of the electrons and holes inside the droplets.

Neutral defect complexes, like deep levels and isoelectronic traps, may also exhibit defect specific, radiative transitions [Pan1975].

The energy positions of the peaks in the luminescence spectrum indicate the types of transitions taking place during the recombination process. The types of occurring transitions depend, to great extend, on the temperature at which the spectra are taken. For example, at room temperature, the spectra are typically dominated by band-to-band recombination because all the shallow impurities are ionized. The resulting room-temperature spectra show a broad peak centred at approximately room-temperature band gap of silicon.

3.1.1. Setup for photoluminescence measurements

The experimental setup for photoluminescence measurements is shown in Figure 3.2. The sample is placed in a cryostat (Konti-CryoVac) which allows to adjust the temperature in the range 77K - 325K. The excitation beam is supplied by an Ar^+ laser with wavelengths 488 or 514 nm. In some cases 647 nm radiation from a Kr-Ar ion laser was used. The beam passes a filter, F_1, which extinguishes radiation with wavelengths longer than 800 nm (infrared suppressor) preventing infrared radiation from the source to enter the detection system. Although the infrared radiation from the source has low intensity, if not filtered, it can mask the week infrared luminescence signal from the sample. The power of the beam is controlled by a system of two partially crossed polarizers P_1 and P_2. The laser beam is modulated by a chopper in order to apply lock-in technique for detection of the signal. The excitation light is directed normal to the sample surface and is focused to a spot of about 100 μm in size by a parabolic mirror with a focal length of 12 cm. The same parabolic mirror is used for collecting the luminescence. This configuration of normal incidence of the excitation beam and collecting the luminescence normally to the specimen surface gives the maximal signal. A filter, F_2, blocks the reflected and scattered excitation light. It is a long-pass filter, transmitting only light with a wavelength longer than 800 nm. The luminescence spectrum is spectrally resolved by a monochromator (HR 640 Jobin Yvon) equipped with a 300 groves/mm grating and blazed at 1300 nm. The system allows to change the spectral resolution by exchanging the gratings and using 600 or 1200 groves/mm ones. The bandpass of the spectrometer is adjusted by the widths of the entrance and exit slits to 15 nm by using the second order diffraction of the 514 nm line of the laser. The filters are removed and the detector is replaced with a silicon photodiode sensitive to the radiation scattered from the sample. The width of both monochromator slits is

adjusted, so that the full with at half maximum of the second order diffraction peak is 15 nm. As the laser excitation line is much narrower, that broadening reflects mainly the instrumental line profile.

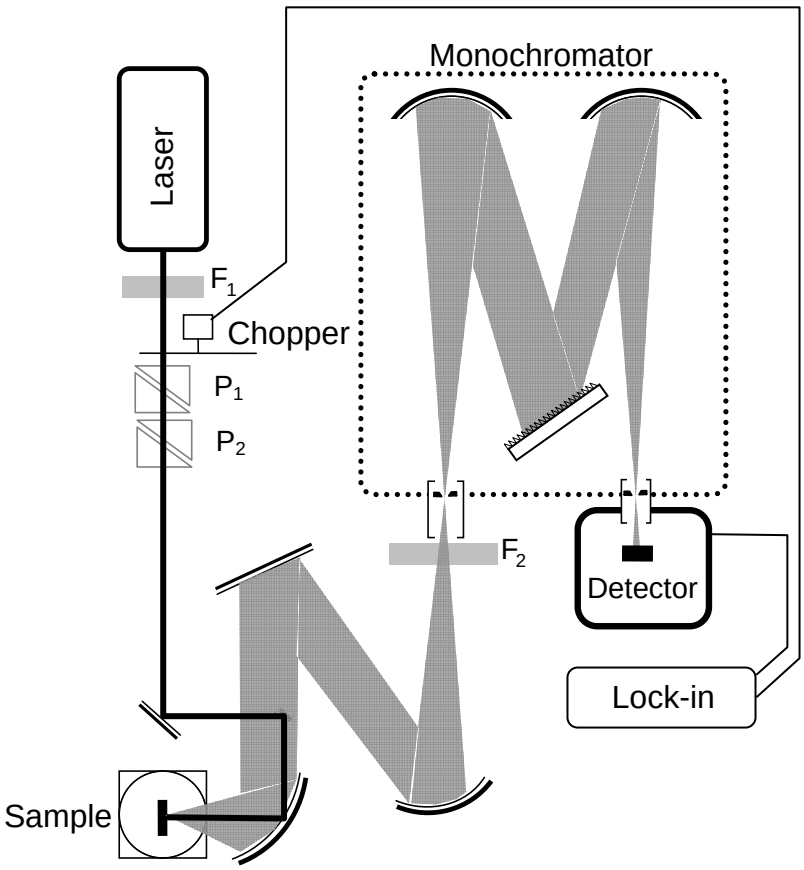

Figure 3.2. Photoluminescence setup. The sample is mounted in a cryostat and is excited by a laser beam. The laser beam is directed normal to the sample surface and focused at the sample to a spot size of about 100 μm. The luminescence is gathered by a parabolic mirror and analysed in a monochromator, which is equipped with a cooled germanium detector. The filters F_1 and F_2 prevent infrared light from the excitation source, respectively visible excitation light to appear at the detector.

A liquid nitrogen cooled germanium p-i-n diode (North coast L) is used for detection. The detector is sensitive in the wavelength range 0.8 - 1.8 μm. The response time of this detector of 5 ms requires to select a low modulation frequency for the lock-in measurements. In all experiments, 33 Hz modulation is used. The integration constant of the lock-in is usually set to 30 ms. Spatial line scans of the photoluminescence can be done by changing the position of the sample in the cryostat and recording spectra at every point. Maps of a certain spectral line are prepared by pointwise scanning the sample, placed in a second cryostat (Microstsat N), which is mounted on a motorized positioning stage.

3.1.2. Sensitivity correction

Because of the wavelength dependent sensitivity of the detector and the ability of the grating to disperse light with different efficiency in the different parts of the spectral range of interest, the response of the system does not reflect the real distribution of the spectral energy density. That is why a calibration is necessary. The calibration is done by means of a halogen lamp with known temperature of the wire, emitting black body radiation. The Plank's law is used to calculate the spectral distribution of the radiation energy density from the source. The calculated spectrum is divided by the measured lamp spectrum, yielding a multiplication factor curve, shown in Figure 3.3.

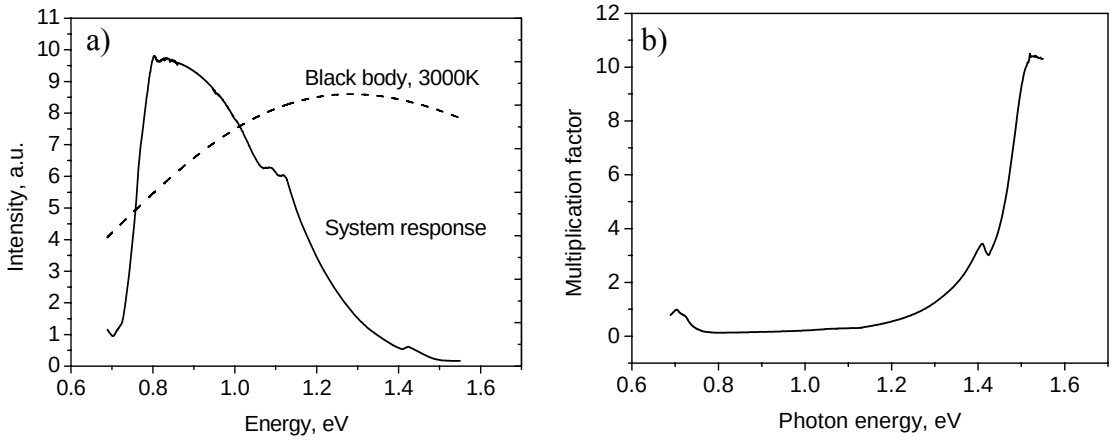

Figure 3.3. Calibration of the spectral response. a) Black body radiation spectral energy density curve and uncorrected system response. b) Multiplication factor used for calibrating the spectra. It is obtained by dividing the black body radiation curve by the system response one.

3.1.3. Spatial resolution of photoluminescence scans

The estimation of the system spatial resolution is done classically by scanning a sample with a sharp edge formed on a piece of CZ silicon with natural oxide by partially covering with aluminium. The intensity of band-to-band luminescence is recorded. Figure 3.4.a shows the profile of the luminescence intensity.

The profile of the intensity can be well fitted by the product of two complementary-error-functions:

$$I(d) = A\int_{d}^{\infty} \exp\left[-\left(\frac{x-x_0}{L_1}\right)^2\right]dx \int_{d}^{\infty} \exp\left[-\left(\frac{x-x_0}{L_2}\right)^2\right]dx, \qquad (3.4)$$

where A is a constant, x_0 is the position of the edge, I the intensity the luminescence, d and x stand for the coordinate along the scan. The two parameters L_1 and L_2 are characteristic distances for the laser spot size (dotted line in Fig. 3.4b) and the lateral distribution of the injected carriers (full line in Fig. 3.4b), respectively.

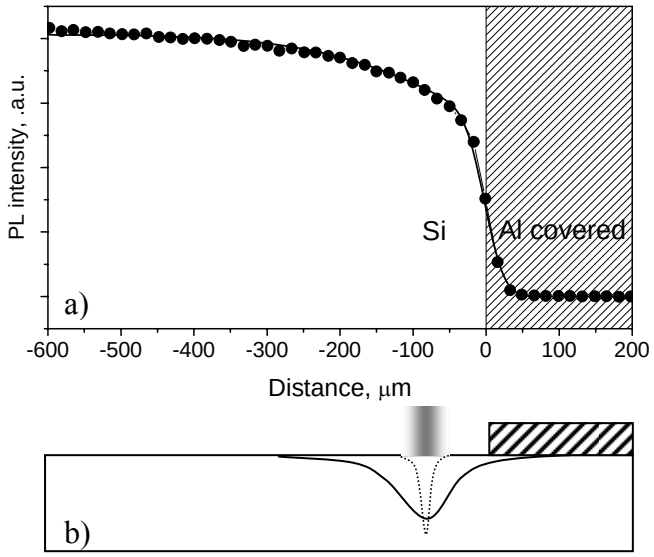

Figure 3.4. Estimation of the spatial resolution. a) Dependence of the band-to-band intensity by scanning the excitation beam across the edge of an opaque aluminium film on the surface of a silicon sample. b) Schematic representation of the processes leading to such shape of the curve. The excitation beam with a Gaussian profile (dotted line) is assumed to induce a broad maximum of excess carrier in (full line), the width of which is determined by the diffusion.

The choice of the complementary error function is made because it describes the convolution of a Gaussian with a step function. The fit curve is shown together with the experimental points in Fig. 3.4a, L_1 is estimated from the fit to about 300 μm and L_2 to 30 μm.

The laser beam induces excess carriers in the sample. They diffuse out of the place of generation. The carriers' spatial distribution has a characteristic size of the diffusion length. The band-to-band luminescence intensity is proportional to the excess carrier concentration (in case of low injection) and, consequently, its spatial distribution follows that for the injected carriers. When the laser approaches the covered area of the sample, part of the carriers diffusing out of the irradiated spot recombine beneath the aluminium stripe and their radiative recombination does not contribute to the total detected radiation. When the laser partially hits the stripe, the illuminated area shrinks, causing a rapid decrease in the intensity of the luminescence. The parameter L_2 = 30 μm is the characteristic distance in this case and it corresponds to a Gaussian shaped laser beam[2] with a full width at half maximum of about 50 μm.

Such broad laser spot is desired in order to minimize the local heating of the sample due to the deposited optical power. One should take into account, that the minority carriers in the studied multicrystalline silicon materials usually have diffusion lengths in the interval 10 to 100 μm.

[2] The 2 mm wide laser beam is focused by a mirror with 12 cm focal length, which limits the minimal spot size to about 30 μm for a wavelength of 514 nm.

The chosen laser spot size allows an optimal spatial resolution for mapping and it is sufficiently wide to avoid a local heating, when illuminating with laser power of about 100 mW.

3.1.4. Role of surface recombination

The surface of a semiconductor is a large sink for excited carriers. If not passivated it decreases strongly the effective lifetime of the minority carriers and the efficiency of the radiative recombination.

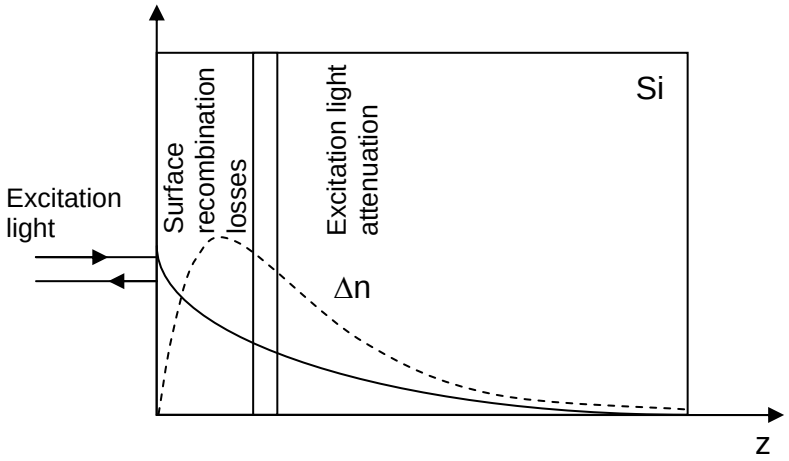

Figure 3.5. Light excitation of excess carriers. The light hits the surface of the semiconductor and is partially reflected and partially absorbed. The absorbed light generates carriers, Δn.

To demonstrate the role of the surface recombination for the luminescence intensity we consider the one-dimensional problem of light excitation on a semi infinite semiconductor (Fig. 3.5). In the case of carrier generation by illumination with monochromatic light the generation rate, *G*, depends on the penetration depth, *z*, and according the Beer's law, is given by:

$$G(z) = (1-R)\alpha\Phi\exp(-\alpha z) \tag{3.5}$$

where *R* is the reflectivity, α is the absorption coefficient of the excitation light and Φ is the photon flux. The excess carriers, Δ*n*, diffuse into the sample or recombine. The diffusion equation in case of stationary conditions i.e. equilibrium between generation, recombination and diffusion, gives the following relation:

$$0 = D\frac{\partial^2\Delta n}{\partial z^2} + G(z) - \frac{\Delta n}{\tau}, \tag{3.6}$$

where *D* denotes the diffusion constant for minority carriers and τ stands for their lifetime.

This equation is solved under the following boundary condition:

$$D\left.\frac{\partial\Delta n}{\partial z}\right|_{z=0} = -S\,\Delta n(0) \tag{3.7}$$

where *S* denotes the surface recombination velocity. The solution of equation (3.6) is given by:

$$\Delta n(z) = \frac{(1-R)\Phi\alpha\dfrac{L^2}{D}}{1-(\alpha L)^2}\left[\exp(-\alpha z) - \left(\frac{\alpha L + \dfrac{SL}{D}}{1+\dfrac{SL}{D}}\right)\exp(-\frac{z}{L})\right], \tag{3.8}$$

where the relation $L = \sqrt{D\tau}$ between diffusion length, L, and lifetime, τ is taken into account.

Figure 3.6a illustrates the distribution of excess carriers in two extreme cases of surface recombination: 1) without any (solid line) and 2) with extremely fast one (dashed line). The curves are calculated for 514 nm excitation ($\alpha = 1.18\text{x}10^4$ cm^{-1}) [Gre1987].

Obviously, fast surface recombination leads to a lower excess carrier concentration than in the case of no surface recombination. The same relation holds for the intensity of the luminescence, too.

Excitation at longer wavelengths, maintaining the photon flux constant, shifts the maximum of the excess carrier distribution in depth and increases their overall concentration (Fig. 3.6b). Thus, excitation at longer wavelengths is favourable for samples with high surface recombination velocity.

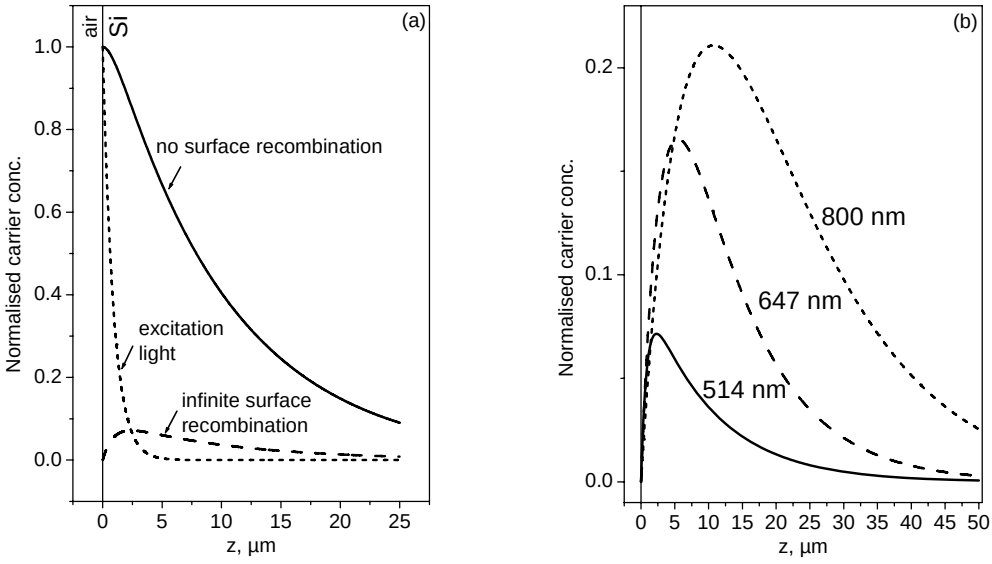

Figure 3.6. Influence of the surface recombination on the excess carrier concentration.
a) The 514 nm excitation light extinguishes exponentially within the sample. Without surface recombination, the concentration of excited carriers near the surface is high and falls exponentially in depth (the decay is due to the diffusion). At high surface recombination, the concentration of carriers at the surface is small and the overall carrier concentration is low as compared to the case of no surface recombination.
b) Variation of the excess carrier distribution with wavelength at constant photon flux and infinite surface recombination. The diffusion length is taken 10 µm.

The surface recombination velocity at the Si/SiO_2 interface depends strongly on the oxidation procedure, on the doping type and on the concentration of dopants in silicon [Ead1985]. However, it turns out that at high injection levels (minority carrier concentration > 10^{19} cm^{-3}) it is reduced strongly and gets independent on the doping level and the doing type.

An enhancement of the photoluminescence signal can be achieved by surface passivation. It has been shown that the surface recombination velocity, S, of oxidised samples (S~10^4 cm/s) can be significantly reduced by rinsing in hydrofluoric acid (S~10^3 cm/s) due to hydrogen termination of the dangling bonds [Bae2005].

3.2. "Spectral Response" Technique

Diffusion length measurements on processed solar cells can be performed by the so-called spectral response technique (Figure 3.7). The technique is based on the measurement of the short circuit current through the p-n junction of the cell, under illumination with light at different wavelengths [Ort1990]. Due to the dispersion in the absorption coefficient of silicon the light at longer wavelengths, generate carriers deeper in the sample (See 3.1.4). These carriers may either recombine in the bulk or reach the junction by diffusion. Those which diffuse to the depletion region of the junction are collected, producing the current which is measured.

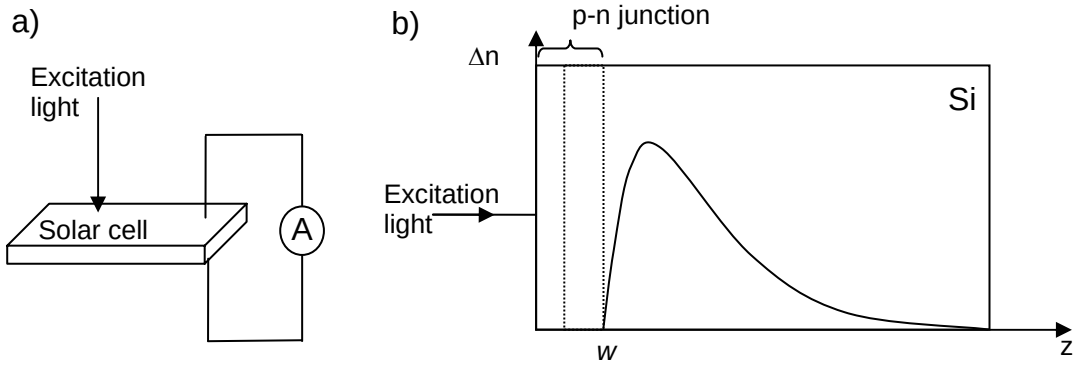

Figure 3.7. Spectral response technique for measurement of minority carrier diffusion lenght. a) Schema of the setup. b) Excess carrier distribution within the sample. The depletion region ends at depth w.

The current density, j, outside the depletion region, is determined by the diffusion, caused by the gradient in the minority carrier depth distribution.

$$j = -D \left. \frac{\partial \Delta n}{\partial z} \right|_{z=w} \tag{3.9}$$

The carrier distribution can be calculated by solving Eq. (3.6) with the following boundary conditions:

$$\begin{matrix}\lim_{z\to\infty}\Delta n(z)=0\\ \Delta n(w)=0\end{matrix}, \tag{3.10}$$

where w denotes the depth of the depletion region. A relation between the diffusion length, L, and the wavelength, λ, dependent parameters: photon flux, Φ, current trough the junction, I, and the absorption coefficient, α, can be obtained:

$$L+\frac{1}{\alpha(\lambda)}=K\frac{\Phi(\lambda)}{I(\lambda)} \tag{3.11}$$

where K accounts for the parameters which are wavelength independent. The equation presents the diffusion length as a constant parameter in a linear dependence between two wavelength dependent variables $1/\alpha(\lambda)$ and $\Phi(\lambda)/I(\lambda)$. It is obtained by linear regression analysis of the experimental data at different wavelengths.

3.3. Electron beam induced current mapping

The electron beam induced current (EBIC) mapping is a semiconductor analysis technique, performed in a scanning electron microscope (SEM), used to identify defects in semiconductors and to examine their recombination properties [Lea1985]. In EBIC, energetic electrons deliver energy for creating electron-hole pairs. An internal electric field existing in the depletion region of a short-circuited Schottky or p-n junction at the surface of the sample separates the electrons and holes and, consequently, induces a current.

By using the signal from the picoampermeter as imaging signal, an EBIC image is formed. Because the electron beam diameter of a SEM is very small, it is scanned across the sample and variations in the induced current are used to map the recombination activity. When a Schottky junction is imaged in plan-view, areas free of defects will show bright contrast (the carriers arrive at the junction), and areas containing defects will show a dark one (the carriers recombine at the defects).

3.4. Materials and treatment of the multicrystalline samples

Almost all commercially produced solar cells employ a p-type material as substrate, on which a thin n-type layer is prepared by diffusion of donors (e.g. phosphorous). Such construction is more or less historically inherited from the solar cells for extraterrestrial application and is due to the higher resistance of the p-type silicon against high energetic particle radiation [Rap1962]. In contrast, n-type substrates have some important advantages:

- The metal impurities capture cross section for holes σ_p, are significantly smaller than for electrons σ_n (e.g. Fe interstitial donor: σ_n = 5x10^{-14} cm^{-2} and σ_p = 7x10^{-17} cm^{-2} [Mac2004]).

That is why it is expected that the diffusion length of the minority carriers in n-type material is longer than for p-type at the same impurity concentration [Mac2004].

- The missing boron in the substrate cannot cause a formation of iron-boron or oxygen-boron complexes, which are responsible for the light induced degradation of the solar cells, [Sch1998, Bir2005].

In the scope of the work p- and n-type silicon was studied. The samples were prepared from two types of materials, widely used in the photovoltaics.

3.4.1. Edge Defined Film Fed Growth (EFG) silicon

One of the material types investigated in this work is produced by the so-called Edge Defined Film Fed Growth (EFG) technique. The principle is schematically shown in Figure 3.8a. Silicon foil is pulled out of a melt through a graphite die. The molten silicon forms a meniscus at the top of the die, which is placed in contact with a seed foil. The crystallisation occurs at the meniscus contact with the seed foil, in the melt confined between the edges of the die and the foil. The technique requires a precise control of temperature gradients and pulling rates. Typically, the resulting foils contain high concentration of substitutional carbon (10^{18} cm^{-3}) and relatively low concentration of interstitial oxygen ($5x10^{16}$ cm^{-3}) when compared to the block cast silicon, where, usually, the oxygen concentration is higher than that of carbon. Non-recombination active twin boundaries are typically formed in EFG silicon. The dislocation density strongly varies within the material and it is typically in the range 10^{4}-10^{6} cm^{-2}.

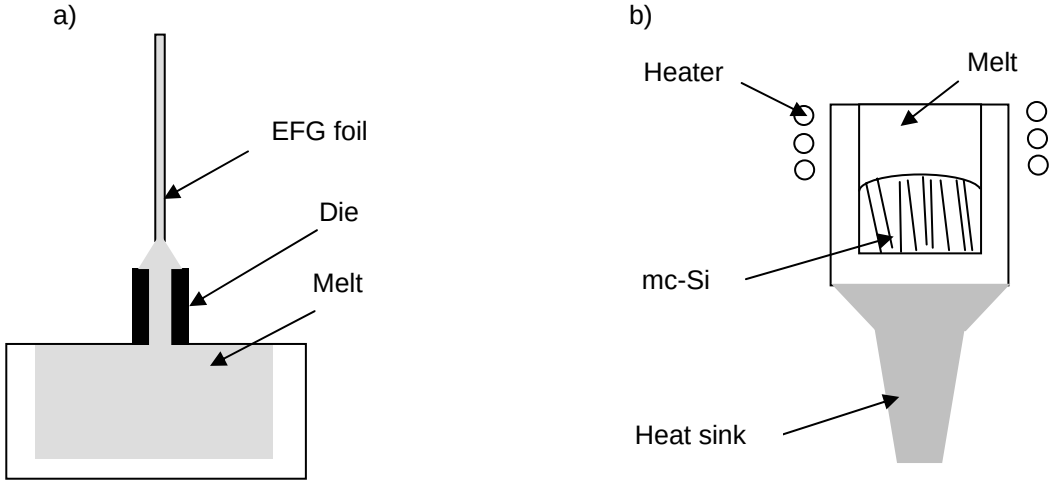

Figure 3.8. Methods for crystallisation of multicrystalline silicon (mc-Si). a) Edge Defined Film Fed Growth (EFG). b) Heat Exchange Method (HEM)

3.4.2. Block silicon

The second type materials studied here are produced by solidification of a silicon melt in blocks. Two variants of this technique are available - block casting method and so-called Heat Exchange Method (HEM) (Figure 3.8b). HEM involves melting of the initial material and solidification of the melt, afterwards. The melting and the solidification are carried out in the same crucible. After the melting step, the crystallisation is initiated by putting the crucible bottom in a thermal contact with a heat sink.

In the case of block casting, molten silicon is introduced in the crucible for crystallization and the temperature gradients in the melt, during the crystallisation are controlled by top and side heaters.

In both methods, the silicon melt crystallises in an ingot, in a way that the crystallisation front travels from the bottom to the top of the ingot. Due to segregation of impurities and contamination from the crucible, the top and the bottom parts as well the parts in contact with the side walls of the crucible are not used for solar cell production. The dislocation density is typically in the range 10^4-10^6 cm^{-2}.

3.4.3. Phosphorous Diffusion Gettering

Some of the samples studied here were subjected to phosphorous diffusion gettering (PDG). The effect of PDG on the luminescence is of interest, as this gettering step is commonly used in the production. The phosphorous emitter diffusion is a part of the solar cell production process. During the emitter diffusion a gettering effect occurs. PDG [Spi1997] involves creation of pears of phosphorous with metal ion or phosphorous-metal complexes. The transport of metal contamination during the PDG is mediated by a kick out reaction of the interstitial silicon with metal contamination atoms on interstitial lattice places. During the diffusion silicon interstitials are formed, which diffuse in the bulk of the wafer, causing a replacement of the metal atoms. The latter are transported to positions in the sample where the silicon interstitial current drains out - like the interface of the phosphorous source / silicon wafer or extended defects in the bulk.

3.5. Materials and treatment for silicon based light emitters

Epitaxially grown layers of a few micrometer thicknesses are used for preparation of light emitting devices on CZ silicon wafers (n-and p-type with resistivity of several Ω cm) (See Part III). Implantation of phosphorus, boron or silicon at energies between 135 to 750 keV and doses in the range from $4x10^{12}$ to $1x10^{15}$ cm^{-2} is used to form an implantation-damaged area. After implantation, the samples were heat treated in a furnace or by rapid thermal annealing

(RTA) in order to form extended defects in the implantation-damaged area. Alternatively, wafer direct bonding was applied for preparation of dislocation rich areas in some of the samples. A detailed description is given in Chapters 8 and 9.

3.6. Summary

A brief overview of the methods, used for optical and electrical characterisation in this work was given. The main characterisation was carried out by means of photoluminescence spectroscopy and therefore the apparatus was described in more detail. The role of the measuring conditions and the sample recombination properties, like excitation wavelength, size of the irradiated area, and velocity of the surface recombination were discussed in view of optimal excess carrier generation and optimal luminescence signal.

The structural defects in silicon, which are subject of study, are either formed in the process of crystal growth or are result of additional treatments like ion implantation, annealing, or wafer bonding. The methods for growing multicrystalline silicon for photovoltaics and the procedure for gettering of impurities during emitter diffusion in the cells were briefly revealed.

Part II

Characterisation of solar cell grade silicon by means of scanning photoluminescence spectroscopy

Chapter 4

Correlation between electrical and optical activities in EFG silicon. Influence of the surface recombination and stress.

In this chapter the correlation between the dislocation activity and their luminescence is revealed. The typical spatial distribution of the recombination activity in defect-rich and defect-free zones in n- and p- type silicon is characterized by means of photoluminescence and EBIC mapping. It is compared with the distribution of the diffusion length, measured by means of spectral response technique. Temperature dependent EBIC and photoluminescence measurements are applied to study the relation between the dislocation contamination and their radiation.

Inhomogeneous defect distribution is typical for the solar cell grade silicon. It is the origin for spatial inhomogeneity of the electronic properties. Therefore, for production in-line and off-line diagnostics, application of scanning techniques is strongly required. Defect mapping can be employed for initial screening and follow-up local analyses in large-scale materials and devices. In this chapter, such approach is illustrated on multicrystalline silicon wafers. Three different mapping techniques were applied concurrently to as-grown and processed EFG silicon. We report on mapping of (1) minority carrier diffusion length, (2) photoluminescence, and (3) EBIC at different temperatures.

4.1. Correlation between the electrical and the radiative activity of the dislocations in EFG silicon

In order to use the photoluminescence to characterise solar cell grade material one needs to find a relation between the photoluminescence spectral features and the recombination active defects, present in the material. The spatial distribution of recombination active defects in a sample is determined by mapping of EBIC and the diffusion length of minority carriers. That spatial distribution is then correlated with the spatial distribution of the photoluminescence spectral features. Te results presented below are obtained from a p-type EFG silicon. The sample is prepared from a processed solar cell by etching the emitter and the backside contacts. Aluminium Schottky contact formed on a fresh etched surface are used for EBIC measurements.

4.1.1. Estimation of dislocation contamination level

In a first step, EBIC measurements allow to find defect reach areas on the sample and to estimate the activity of the dislocations there. To determine the activity of the defects and their distribution in the sample, two EBIC micrographs at 77 K and at 300 K are taken (Figure 4.1a and 4.1b, respectively). The defect rich regions appear dark on the micrographs, because the excess carriers predominantly recombine at the defects, not contributing to the measured current (i.e the collection efficiency is low). The profiles of the collection efficiencies at these two temperatures are shown in the Figure 4.1c.

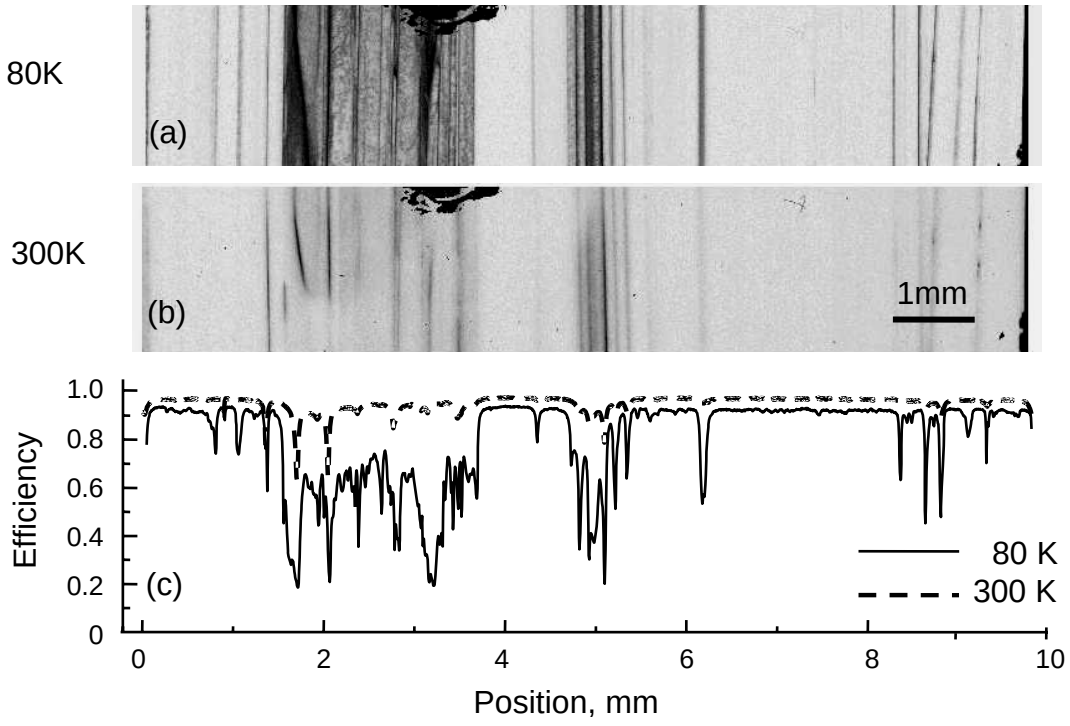

Figure 4.1. EBIC micrographs taken at 80 (a) and 300 K (b) and the corresponding profiles of the collection efficiency (c). The high recombination activity in defect-rich regions causes a reduction of the collection efficiency, which is more pronounced at low temperature.

The recombination activity of the defects is influenced by the temperature. At low temperature, the defect-rich regions (most probably consisting of closely packed dislocations) show a strong recombination activity. At room temperature, the recombination activity of the defects is much weaker, because the collection efficiency at 300 K is remarkably lower than that at 80K. For some defects, the activity at room temperature even vanishes. According to the model of dislocation activity presented in Chapter 1, the level of contamination can be estimated. The temperature behaviour of defect-rich regions corresponds to type 1 and type 2 of those given in Chapter 1 and in [Kit1995d, Kit1995c, Kit1995b]. The two types are typical for relatively low contaminated dislocations with transition metals, at the order of 10 impurity atoms/μm of dislocation length.

4.1.2. Comparison of photoluminescence and EBIC maps

Photoluminescence characterisation of the same material is carried out after the Schottky contact was removed by etching. Figure 4.2 shows in comparison, room temperature micrographs of photoluminescence and EBIC. The photoluminescence micrographs are taken at photon energy of 1.1 eV for the band-to-band luminescence and at 0.8 eV for D1 luminescence. A laser beam with 514 nm wavelength is used for excitation. The mapping system allows scanning across the sample without any sophisticated preliminary preparation, but at lower spatial resolution then EBIC. The band-to-band and the defect related D1 luminescence are essentially reversed. D1 luminescence is observed from the areas, where the band-to-band one is low.

The EBIC micrograph represents the total recombination activity of the defects (radiative and nonradiative). As in silicon the radiative recombination is only a minor contribution to the total recombination, the main part of the recombination process is nonradiative. The balance between the recombination and generation rates determines the equilibrium excess carrier concentration. In the case of low injection, the band-to-band recombination is proportional to the excess carrier concentration. The similar lateral distribution of dark and bright areas in the EBIC and band-to-band micrographs reflects the distribution of the nonradiative recombination at defects in the sample. The D1 luminescence is predominantly strong at the positions where band-to-band luminescence is low and the EBIC shows dark contrast. The presence of D1 indicates, that the recombination-active regions contain dislocations and that the dislocations are responsible for the enhanced recombination activity there [Kos1999, Kit2002].

Although, the band-to-band luminescence and the EBIC collection efficiency show similar pattern, some differences are accounted. These differences originate either in the lower

resolution of the photoluminescence mapping system or in inhomogeneities of the surface recombination.

The photoluminescence and EBIC micrographs reveal defect areas on the sample with increased recombination activity, where a decreased diffusion length can be expected. Quantitative information about the recombination activity is be obtained by measuring the diffusion length of minority carriers. For instance, the experimentally obtained dependence of the band-to-band luminescence intensity on the diffusion length can be used for estimation of the diffusion length on samples of the same material type.

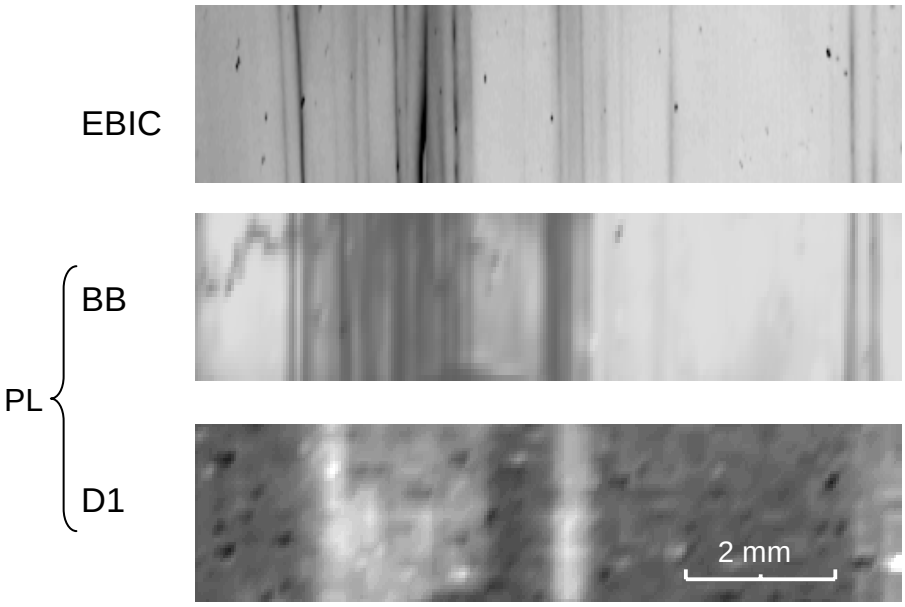

Figure 4.2. Micrographs of room temperature EBIC and photoluminescence (PL). The photoluminescence images present the intensity of band-to-band luminescence and D1 luminescence across the sample. (Note that the bright and dark round spots in the D1 image are artefacts.)

4.1.3. Correlation between band-to-band luminescence and minority carrier diffusion length

In contrast to the spectral response characterisation, the luminescence spectroscopy is usually carried out on samples with no junction at the surface. Thus, if not passivated, the surface can exhibit spatial variations in its recombination activity. The surface recombination may have an influence on the luminescence intensity dependence on the diffusion length. That is why, below, its role is explored in more detail. A relation between diffusion length, surface recombination velocity and excess minority carrier concentration can be derived, considering the model of an illuminated semi-infinite semiconductor (See Chapter 3). The radiative band-to-band recombination rate R_{rad}, is assumed proportional to the total surface density of excess carriers Δn_{tot}, supposing low injection regime.

$$R_{rad} \sim \Delta n_{tot} \tag{4.1}$$

The surface density of the excited carriers can be obtained by integration of Eq. (3.8) over the dept coordinate of the sample:

$$\Delta n_{tot} = \int_0^\infty \Delta n(z)dz = \frac{(1-R)\Phi\frac{L^2}{D}}{1-(\alpha L)^2}\left[1-\left(\frac{\alpha L+\frac{SL}{D}}{1+\frac{SL}{D}}\right)\alpha L\right] \tag{4.2}$$

In the case of a negligible surface recombination velocity, so that $S\,L << D$, one obtains that the excess carrier concentration and band-to-band luminescence are proportional to the square of the diffusion length, L, and to the minority carrier lifetime, τ, respectively:

$$R_{rad} \sim L^2 \sim \tau\,. \tag{4.3}$$

At high surface recombination or long diffusion lengths, $S\,L << D$, this relation is no more valid. If the excitation light is absorbed in a penetration depth, $1/\alpha$, much smaller than the diffusion length, the band-to-band recombination rate becomes proportional to the diffusion length (Figure 4.3):

$$R_{rad} \sim L\,. \tag{4.4}$$

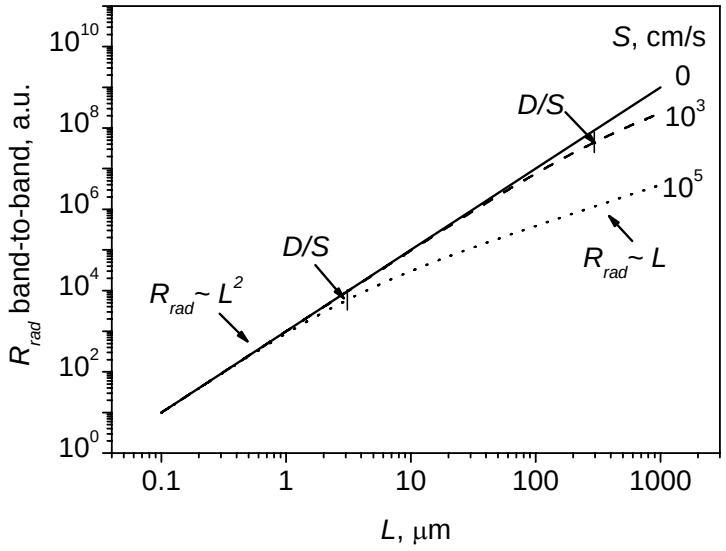

Figure 4.3. Dependence of the band-to-band radiatitive recombination rate on the diffusion length and influence of the surface recombination. The rate can be proportional either to the first or the second power of the diffusion length, depending on the relation between the diffusion coefficient, D, the surface recombination velocity, S, and the diffusion length, L. The curves are calculated for D = 30 cm^2/s, and absorption $\alpha = 10^{-4}$ cm^{-1}.

The minimal diffusion length detected for our sample (Figure 4.4) is about 70 μm, while the penetration depth of the 514 nm excitation light is 0.85 μm. These dependences are derived in assumption of low excitation. They hold to a concentration of excess carriers, which does not exceed that for the majority carriers. (For laser excitation with a power of 0.01 mW/μm^2 at wavelength 514 nm (2.4 eV), assuming a diffusion length of 100 μm and an infinite surface

recombination velocity, the concentration of carriers estimated by Eq. (4.2), is about 10^{15} cm^{-3}, which is at the same order of magnitude as the sample doping concentration).

The diffusion length is measured on the processed p-type EFG sample by spectral response technique. Its spatial distribution profile along a transversal to the direction of growth is scanned point by point. It is compared to the intensity of the band-to-band luminescence along the same line in Figure 4.4. The spatial distributions of the diffusion length and the band-to-band luminescence intensity correlate well. Moreover, the band-to-band luminescence is nearly proportional to the diffusion length, which indicates high surface recombination velocity.

It turns out that band-to-band luminescence can be used to estimate the diffusion length. However, a calibration and the control of surface recombination velocity are required for quantitative results.

The information obtained from band-to-band luminescence intensity is related to both the surface recombination velocity and to the diffusion length of the minority carriers (see Eq. (4.2)-(4.4)). In order to have reliable information from the defects one needs to condition the surface, so that the surface recombination velocity is homogeneous across the surface.

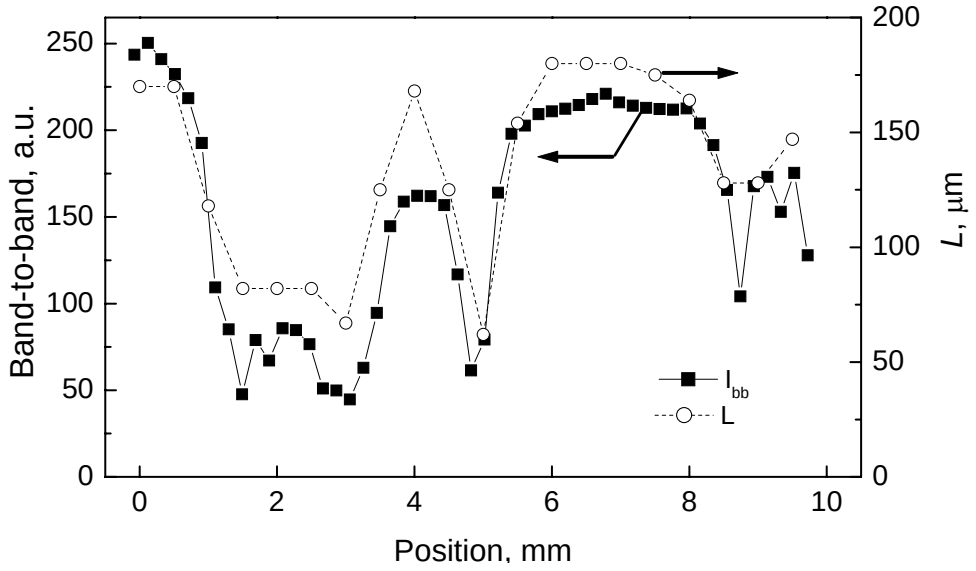

Figure 4.4. Comparison of the profiles of band-to-band luminescence (full line and symbols) and the diffusion length (dotted line and open symbols) measured along the sample at room temperature.

An example of non homogeneous surface recombination is shown on Figure 4.5. Two maps of D1 and band-to-band peak amplitude from an n-type EFG sample, taken at 300 K are compared in the figure. The maps show bright and dark stripes, nearly parallel to each other of high and low luminescence intensity. This luminescence pattern resembles that of the grain distribution, typical for EFG material. An exception exhibits the region, enclosed by a white

dotted line. This region shows strongly reduced both band-to-band and D1 luminescence. The effect indicates a strong surface recombination, which in that case is limiting for excess carrier concentration.

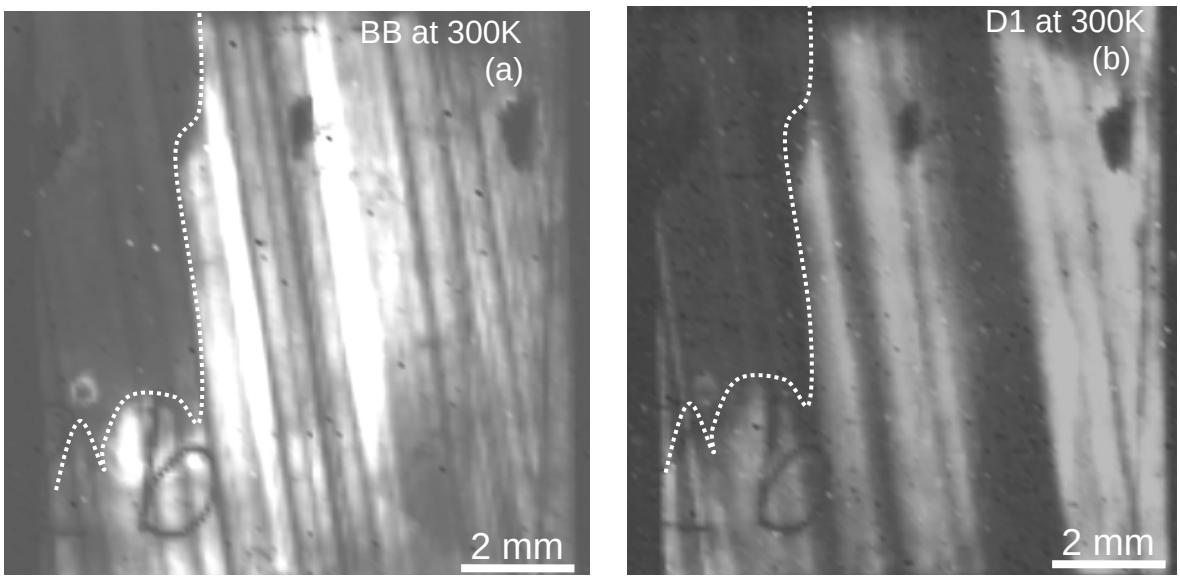

Figure 4.5. Maps of band-to-band (a) and D1 luminescence (b) at 300K from the same sample area. The region on the left side, margined with a white dotted line shows low band-to-band and low D1 luminescence at room temperature when compared to the rest of the sample.

In order to use the band-to-band luminescence intensity for quantitative measurements of the diffusion length, the surface should be conditioned in a way that the surface recombination velocity is uniform across the entire sample.

4.2. Temperature behaviour of the luminescence

The temperature behaviour of the defect-related and band-to-band luminescence is examined to find the deactivation energy of the centres responsible for D1 and D2 radiation. The temperature behaviour of band-to-band gives an indirect access to the behaviour of nonradiative competing processes, which are limiting factor for the excess carrier concentration.

4.2.1. Temperature behaviour of the luminescence from the extended defects

It has been already demonstrated that defect rich areas in the samples contain dislocations, which show room temperature D1 radiation. The EBIC contrast shows that the dislocations' recombination activity is increased upon decreasing the temperature. It is expected that the temperature change will also influence the dislocation radiation.

The formation of the dislocations in the multicrystalline silicon is different from those produced by plastic deformation, which are classically used for studying the dislocation radiation. That may have an influence on the dislocation-related radiation and the temperature

dependence of its spectral features. The defect rich areas of the p-type EFG sample are studied in order to find correlation between the spatial distributions of the dislocation peaks and to find out how the peak parameters change with the temperature.

The variation of the sample temperature states some experimental challenges for tracing the spectra variation at one and same spot in the entire temperature range.

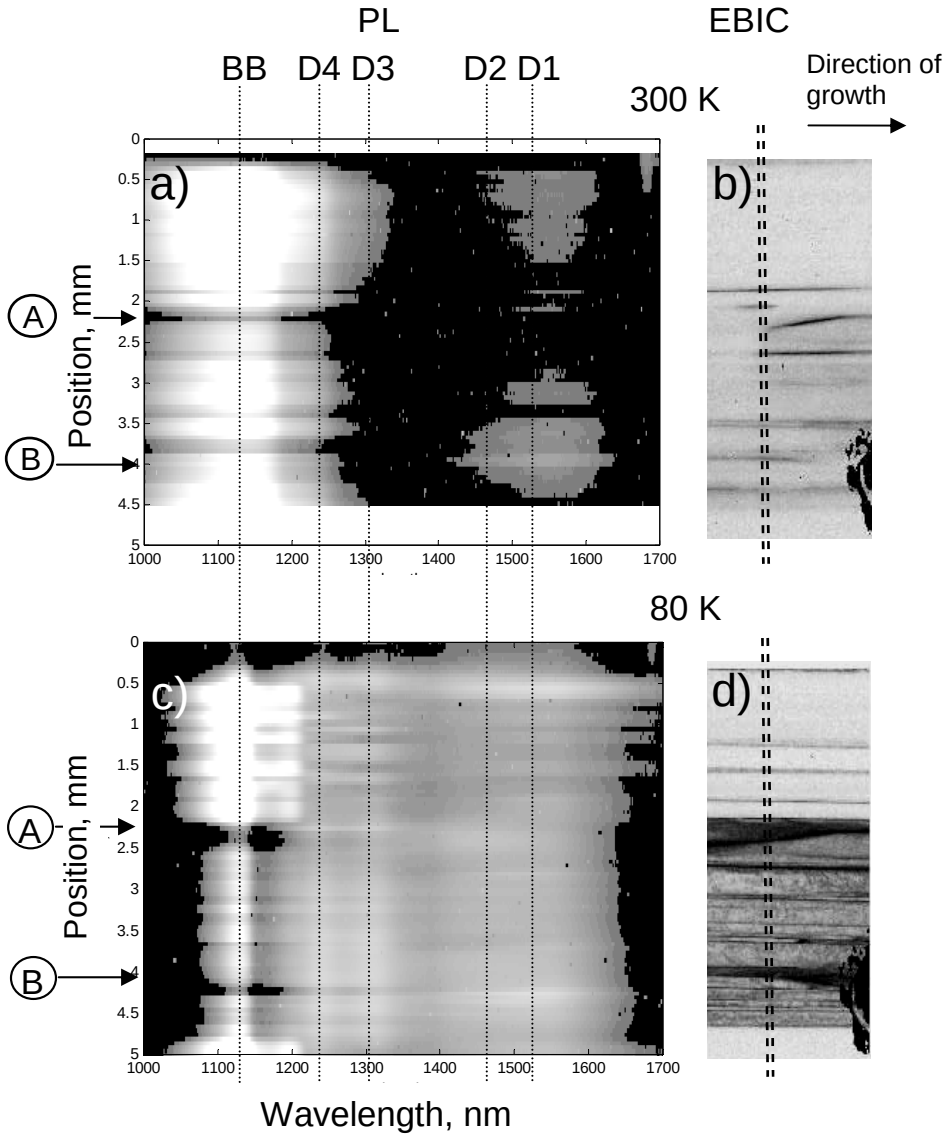

Figure 4.6. Comparison between photoluminescence (a and c) scans and EBIC micrographs (b and d) at 300 and 80 K. Luminescence spectra were taken sequentially along a vertical line (dashed line in c and d) across the sample. The luminescence intensity is given in grey scale with regard to wavelength and position on the sample. D lines (D1, D2, D3 and D4) and band-to-band (BB) luminescence are marked by dashed lines. Detailed spectra at position A and B are presented in Fig. 4.7.

EFG silicon is a nearly homogeneous material along the direction of growth. Significant variations in crystalline quality occur perpendicular to that direction. In fact, as seen on Figures 4.2 and 4.5, the recombination activity varies strongly perpendicularly to the direction of growth, while along that direction the variations are only very weak. This might impose some difficulty for measuring the temperature dependence. In principle, for a reliable evaluation the

luminescence spectra should be recorded over the whole temperature range from one and the same spot. However, due to mechanical shift caused by the temperature change the exact position of the measured sample spot can get lost. Instead of measuring at a single spot, a scan across the sample is taken, recording a spectrum at every position on it. Photoluminescence scans are made at 12 temperatures between 80 and 300 K. Thus one obtains spectroscopic results for the defects across the sample with a 100 μm resolution. The maps in (Fig.4.6 a, c) are constructed from spectra, recorded at fixed points along the scanning line. They represent the intensity of the luminescence light in grey scale with respect to the wavelength and the position on the sample where the spectrum is measured. The EBIC images corresponding to the scans are shown next to photoluminescence data (Fig. 4.6 b, d).

The regions of high recombination activity (dark in EBIC micrographs) show a reduction of band-to-band luminescence and well detectable D band luminescence. Similar to the EBIC collection efficiency, the intensity contrast of band-to-band luminescence between the defect-free and defect-rich areas of the sample increases upon decreasing the temperature. At 80K the band-to-band luminescence is strongly reduced at the defected regions and all four D lines are present.

Although there is a similar temperature behaviour of defect sites on the sample, some quantitative differences can be found between position A at 2.2 mm and position B at 4.1 mm (Fig. 4.6c). At room temperature, the BB luminescence from both places is strongly reduced (Fig. 4.6a). A significant D1 luminescence can be observed only in region B, but it is almost not present in region A. A difference can also be found at 80 K spectra. Figure 4.7 shows a comparison between spectra taken at 80 K at positions A and B, respectively. The spectra are numerically deconvoluted into Gaussian peaks to evaluate the contribution from the different components. The spectrum at position A shows a very weak D1 line. The D1 peak area is nearly one order of magnitude smaller than that of D2. In comparison, the D1 line at position B is significantly stronger and its amplitude is comparable with the D2 amplitude. D3 show almost the same intensity/peak area as D4 at both positions. It is also worth noting that the band-to-band luminescence is stronger, when the sum of D1, D2, D3 and D4 line intensities becomes smaller.

The peak widths are similar on both positions. Assuming, that the temperature behaviour of peak intensity is similar, too, one can construct a mean spectrum from all spectra in the region between A and B investigate its temperature evolution.

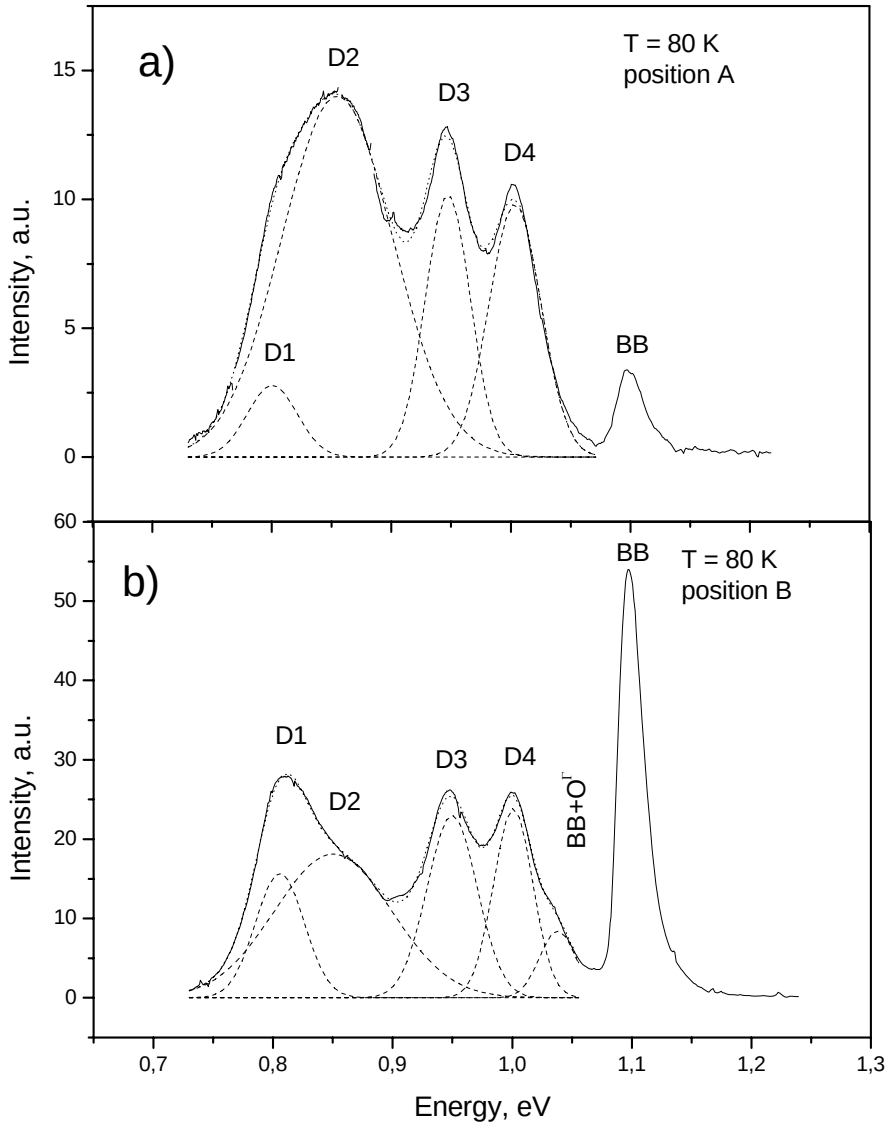

Figure 4.7 Photoluminescence spectra taken at positions A and B (see Fig. 4.6). The dashed lines are Gaussians, obtained by numerical deconvolution of sub-band-gap of the spectrum. The intensity and the width of D3 and D4 are similar, whereas D1 and D2 peak areas differ. At position A the peak area of D1 is one order of magnitude smaller than D2. The D2 appears always broader than other D lines at 80K.

Figure 4.8 depicts the peak area dependencies of D bands on temperature for the defect rich region located between A and B (Fig. 4.6c). At room temperature only D1 is present. Upon decreasing the temperature D2 appears at about 250 K and thereafter D3 and D4 at 190 and 170 K, respectively. D2, D3 and D4 grow upon lowering the temperature, while D1 shows a maximum at about 150 K. The change in the behaviour of D1 can be related to the appearance of D3 and D4. The recombination through D1 becomes lower due to increased recombination through the D3 and D4 centres. It is interesting to note, that the sum of the areas of D1, D3 and D4 lines results in a curve which nearly follows the temperature behaviour of D2.

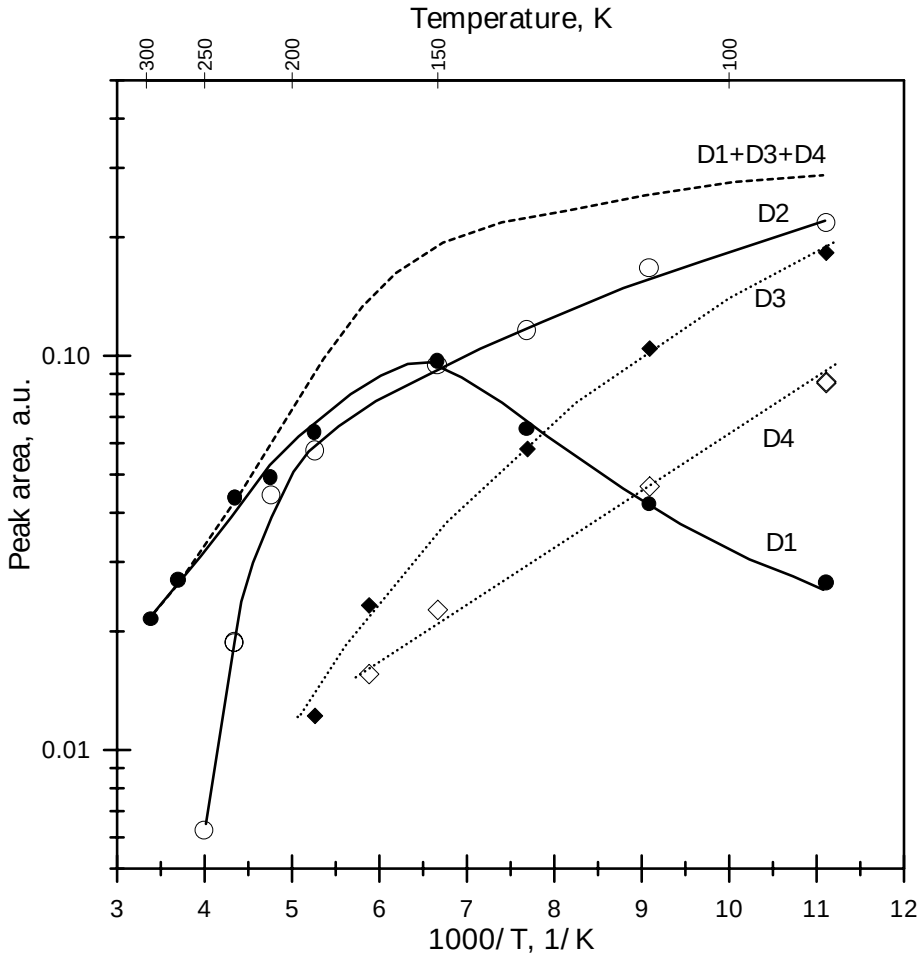

Figure 4.8. Temperature dependence of peak areas. The D2, D3 and D4 increase upon lowering temperature. At high temperatures D1 follows the behaviour of D2. However, after appearance of D3 and D4 it starts to decrease upon lowering temperature. The sum of D1, D3 and D4 is shown as dashed line. It is interesting to note that it follows the temperature dependence of D2, nearly.

The temperature dependence of the D luminescence is used to determine the deactivation energies of the lines. The deactivation energy of D1 is estimated by fitting relation (1.21) or (1.27) (See Chapter 1) to the experimental data for of the temperature dependences of D1 area. The data can be fitted only in the high temperature interval, where a decrease of D1 intensity with the temperature is observed (above 150 K). The scattering in the experimental points and the limited temperature interval do not allow to select between bound to free (1.21) or bound to bound (1.27) deactivation model, as both relations fit the experimental data equally well (dashed line on Figure 4.9) with a deactivation energy about 70 meV. Assuming that there is a bound to free deactivation from a localised state to three dimensional band of the semiconductor a deactivation energy $E_a = (70 \pm 7)$ meV is obtained.

The best fit to the D2 peak area is given by the relation (1.28), suggesting two processes of thermal deactivation of D2. The first is deactivation directly to the semiconductor conduction band, with $E_{a2} = (280 \pm 130)$ meV. The second possible deactivation is to a shallower level with

E_{a1} = (36 ± 3) meV (Figure 4.9b). It is interesting to note, that the deactivation energy E_{a2} is equal to the difference of the silicon bandgap (E_g = 1.12 eV) and the photon energy of the emitted D2 radiation (E_{D2} = 0.85 eV) within the uncertainty intervals:

$$E_g = E_{a2} + E_{D2} \quad (4.5)$$

One can assign the activation energy E_{a2} to a deep level, involved in the D2 radiative transition. In such case the transition would occur between this deep level and the valence band of silicon, not involving the dislocation shallow bands. In contrast, the D1 activation energy, E_a, corresponds to the split off energy of the dislocation one-dimensional bands and thus one can consider them involved in the D1 radiative transition.

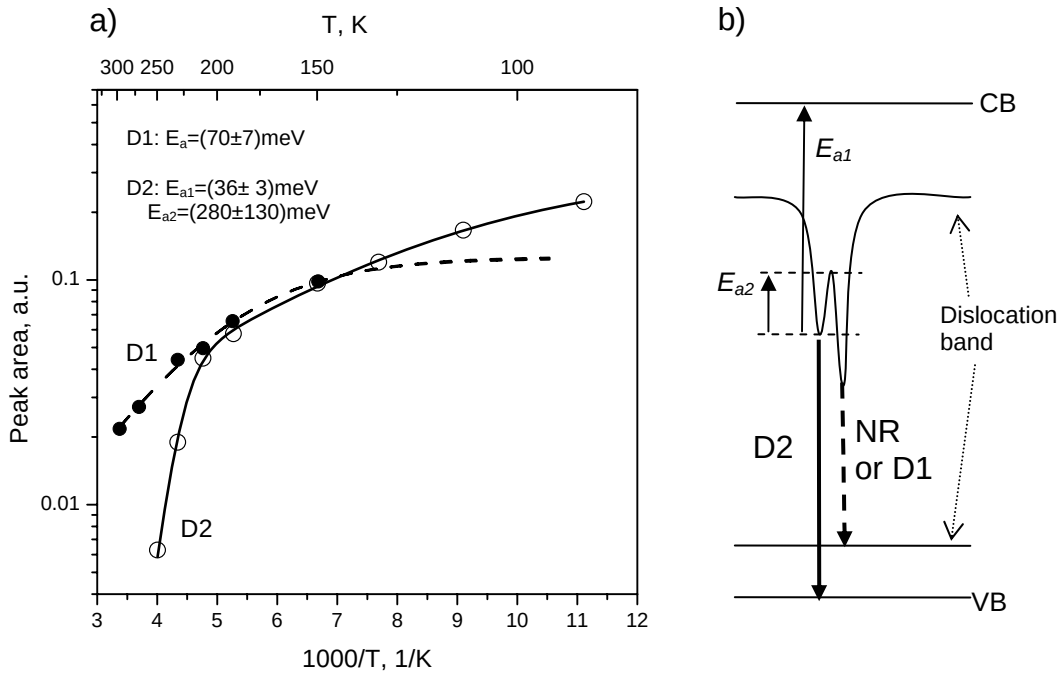

Figure 4.9. Determination of the deactivation energies of D1 and D2 and possible deactivation mechanism of D2. a) The D1 temperature dependence can be fitted only in the range above 150K, where a temperature quenching is observed. b) Possible deactivation process of D2.

Generally, two models of the D1 and D2 transitions have been suggested in the literature. The first one suggests two deep levels (~150 meV) nearly symmetrically separated from the semiconductor three-dimensional bands [Kve1995, Kve1996], while the second assumes a transition between a deep level and a shallow one (4-7 meV) [Saue1985, Sue1983a]. Although, the deactivation energy obtained here are close to those in the first model, the values suggest asymmetric transitions for both D1 and D2.

The temperature dependence of the defect related radiative recombination allows to make conclusions about the levels involved in the emission process. However, their recombination activity is mainly determined by nonradiative processes, which are not accessible directly by

photoluminescence studies. A possibility to gain access to the nonradiative recombination and its temperature dependence is searched in the band-to-band luminescence intensity and its dependence on the temperature.

4.2.2. Temperature dependence of band-to-band luminescence

The presence of recombination active dislocations in the defect-rich regions of the samples causes a reduction of the diffusion length and, therefore, a respective reduction of the band-to-band intensity (See 4.4). It can be expected that the temperature dependence of the diffusion length will influence that of band-to-band luminescence. However, in order to make a correct interpretation one should take into account the temperature decrease of the silicon luminescence due to the thermal destruction of free excitons [Sch1974].

The temperature dependence of the band-to-band luminescence is studied on n- and p-type EFG samples and it is compared with the luminescence temperature behaviour on defect-free FZ silicon. Figure 4.10 shows the temperature dependences of the band-to-band luminescence from defect-rich regions on the n- and p-type samples, together with that measured on defect free silicon (FZ, n-type, phosphorous doped $4x10^{15}$ cm^{-3}).

Although, the measuring and surface treating procedure for both EFG samples are same, the temperature behaviours are opposite. The n-type sample shows increasing band-to-band luminescence upon increasing temperature (anomalous behaviour), while p-type, similar to FZ silicon exhibits a decreasing (normal behaviour). It should be noted that the roll-off rate of the luminescence from p-type silicon differs from that from FZ silicon, the p-type sample showing a less pronounced thermal quenching above 150 K.

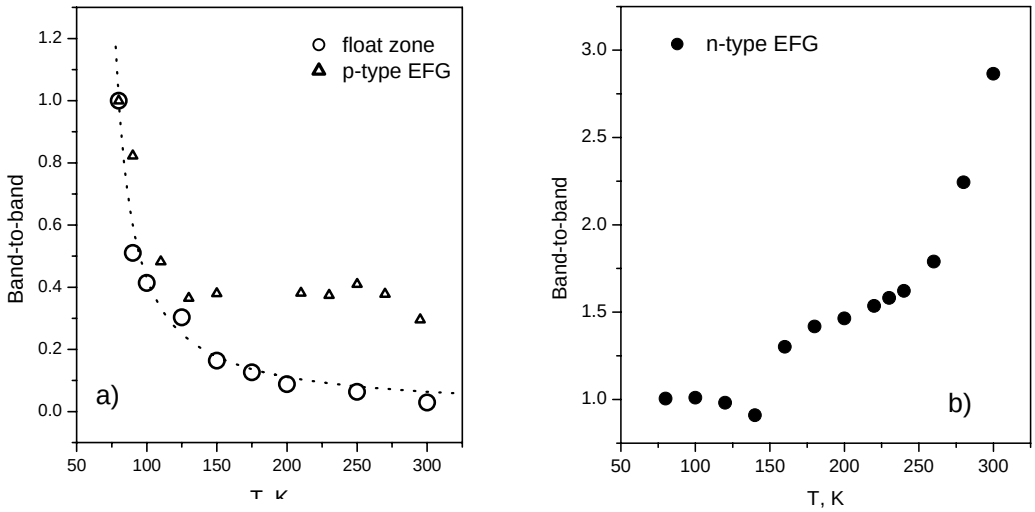

Figure 4.10. Temperature dependences of band-to-band luminescence normalized to the values at 80K of defect-rich regions of the p-type (a) and the n-type (b) samples and compared with the temperature dependence measured on defect-free FZ silicon.

The anomalous behaviour of the band-to-band luminescence from n-type EFG silicon indicates a temperature-induced increase of the diffusion length and minority carrier lifetime. Such behaviour is not typical for the defect free silicon and is clearly caused by presence of defects with temperature dependent recombination activity. One can consider either extended or point defects as possible origin.

Let us first analyse point defects forming shallow recombination centres close to the conduction band. Under the assumption of equal capture cross sections for electrons and holes one can calculate the recombination rate and effective lifetime at different temperatures. In the frame of SRH statistics, the shallow levels are most recombination active when they are equally occupied by electrons and holes. Upon increasing the temperature, the balance between electrons and holes changes in favour to the holes in case of an n-type semiconductor. Consequently, the recombination activity becomes less and the minority carrier lifetime increases. Figure 4.11 illustrates the change of the minority carrier lifetime upon increasing the temperature. The curves are calculated by the SRH theory for two different excitation levels and two different shallow energy levels and are normalized to the values at 100 K. The excitation level, β, is defined as the ratio between the minority and the majority carrier concentrations. The positions of the shallow levels are chosen 45 meV and 70 meV beneath the conduction band in phosphorous doped material. A general trend of minority carrier lifetime increase with temperature is obtained, independent on the excitation level and slightly dependent on the position of the shallow level. As a possible origin for shallow recombination centres one can consider the dopants or centres related to the dislocations. If one assumes that the carrier exchange rate between the one-dimensional dislocation conduction band and the conduction band of the semiconductor is limiting the recombination rate at the dislocation, than the dislocations should behave as shallow recombination centres.

Another possibility to explain the anomalous temperature behaviour can be found in the temperature dependence of the recombination activity of the dislocations (type 2 and mixed type). As it was pointed out (Chapter 1), type 2 and mixed type EBIC contrast behaviours are characteristic for slightly contaminated dislocations (10 to 100 metal atoms per μm dislocation length). The dislocations of those types exhibit strong recombination activity at low temperature and thus can significantly contribute to the decrease of the minority carrier lifetime and the diffusion length at low temperature.

In the p-type sample, anomalous temperature behaviour of band-to-band luminescence is not detected. However, the observed decrease is not as strong as in FZ silicon. It is an indication,

that the effect of increasing minority carrier lifetime at decreasing temperature is also present in p-type EFG, but to a lower extend as in n-type EFG.

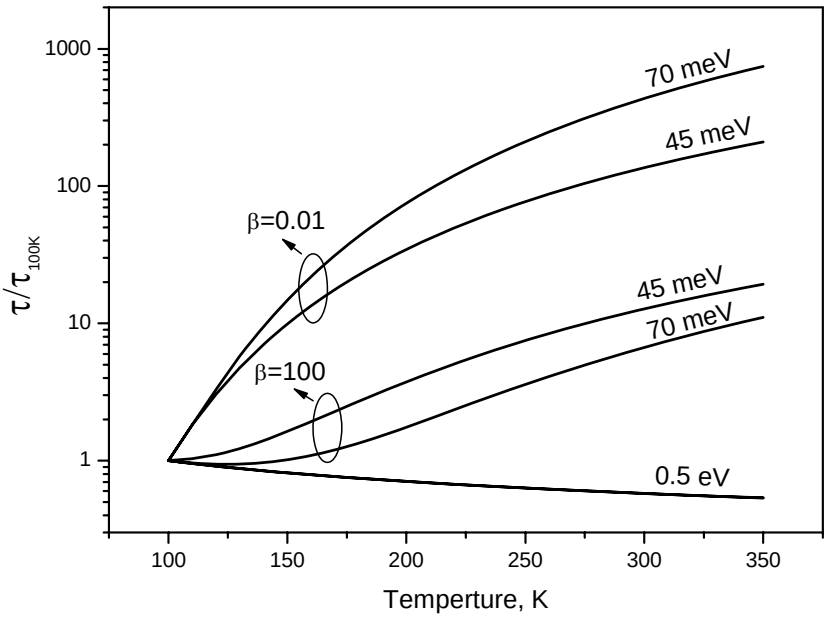

Figure 4.11. Temperature dependence of minority carrier lifetime calculated according to SRH theory for shallow levels at 45 meV and 70 meV from the conduction band gap. The lifetime increases by 1 to 2 orders of magnitude upon increasing the temperature from 100 K to room temperature. The increase of the lifetime can thus overcompensate the temperature quenching of band-to-band radiative recombination. For comparison the temperature dependence of the lifetime calculated for a deep level at 0.5 eV is also given.

The anomalous temperature behaviour is related to shallow recombination centres and their strong activity at low temperature. It will be interesting to see how this recombination centres are influenced by gettering.

4.3. Role of gettering

Phosphorous diffusion gettering (PDG) is widely used in the photovoltaic industry for gettering of metallic impurities [Spi1997, Cue1997]. It has been extensively studied and the mechanisms governing the gettering in dislocation free silicon are relatively well understood [Goe1980]. However, it has been found that in multicrystalline silicon PDG is predominantly effective for sample areas, free of dislocations or with low dislocation densities [Cue1997]. It has been pointed out, that dislocation-rich regions do not exhibit or show just a minor enhancement of minority carrier lifetime after PDG, although the transition metal impurities are gettered from the bulk. The removal of the recombination centres by the gettering leads to a situation in which the recombination activity of the dislocations becomes limiting for the minority carrier lifetime after gettering. It is known that dislocations can significantly increase their activity upon contamination with metals [Kit1993a, Kit1995d] and the metal contamination cannot be

removed completely from the dislocation sites by gettering [McH1997]. Kittler and Seifert [Kit2004a] suggested a model of accommodation of the impurities at the dislocations, situated partially as a cloud surrounding the dislocation and partially integrated in the core (Figure 4.12). One can distinguish between both states of the defects by their specific behaviour in deep level transient spectroscopy [Kno2003]. The impurities at the core cannot be gettered and thus impose the upper limit of PDG efficiency [Cue1997].

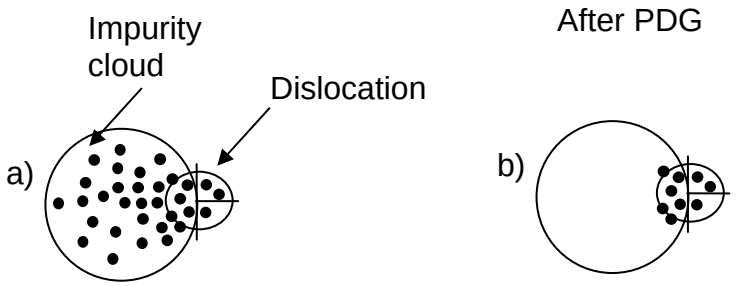

Figure 4.12. Effect of gettering on impurity states at a dislocation: a) initial state with impurity atoms in the core and in the cloud. b) Dislocation after gettering process – the impurities in the cloud removed. (After [Kit2004z])

Beside the dislocation also the shallow centres may be influenced by the gettering. That is why we studied the band-to-band luminescence on as-grown samples and after PDG. The dislocation contamination level is related to the band-to-band luminescence intensity that is why band-to-band luminescence yields information about the dislocation activity.

4.3.1. Influence of PDG on the anomalous temperature behaviour of band-to-band luminescence

The influence of the gettering on the anomalous temperature behaviour of band-to-band luminescence is studied on n-type EFG, subjected to PDG. Figure 4.13 shows the dependence of the peak area on temperature for both as.- grown and PDG samples. The anomalous temperature behaviour observed on as-grown material is enhanced after PDG.

In order to explain that enhancement one should consider two effects, which occur during PDG. First, the gettering removes the metal impurities from the bulk, which are deep recombination centres, and second, it changes the temperature behaviour of the dislocations from mixed type to predominantly type 2 [Kit2004a]. If deep recombination centres are not present in the material the shallow ones (also those induced by the doping) will be decisive for the temperature dependence of the minority carrier lifetime. The dislocations of type 2 which are predominant after the PDG are also active at low temperature and will contribute for the increase of the recombination at low temperature. Thus, both gettering of the metal impurities from the bulk and changing the dislocation temperature behaviour to type 2 contribute to

increasing of the minority carrier lifetime with increasing temperature and respectively to the anomalous temperature behaviour of the band-to-band luminescence.

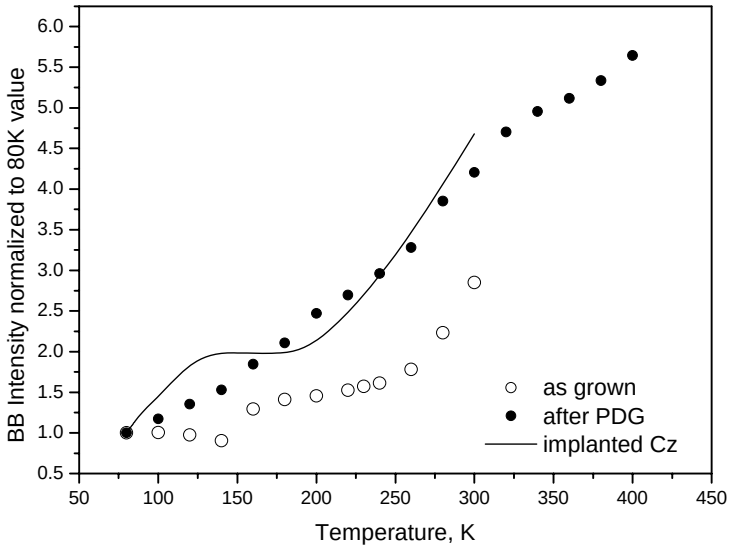

Figure 4.13. Band-to-band luminescence from n-type EFG samples shows anomalous temperature behaviour, which is enhanced after PDG. The model sample, prepared on n-type CZ silicon, containing dislocation loops shows similar behaviour.

To exclude the possibility, that other contaminants in EFG, not related with the dislocations or with the dopants, are responsible for the anomalous temperature behaviour, a model experiment on n-type, microelectronics grade CZ silicon is carried out. Dislocation loops are created by implantation of phosphorous in silicon (implantation energy 750 keV and dose $2x10^{14}$ cm^{-2}) and annealing in a furnace (1000°C for 30 min). The n-type CZ sample, shows a similar anomalous temperature behaviour of the band-to-band luminescence as that observed on n-type EFG subjected to PDG (Figure 4.13).

As the model sample can be regarded free from contaminants, the temperature behaviour of its band-to-band luminescence should be related only to the presence of dislocation loops and donors. The similar anomalous behaviour in EFG concludes that the presence of dislocations and/or shallow levels introduced by the dopants [Lea1976] is the reason for such anomalous temperature behaviour of band-to-band luminescence.

PDG does not only influence the band-to-band recombination, but also the dislocation related one. It is interesting to see how the spectral features related to the dislocations are influenced by the PDG.

4.3.2. Influence of PDG on the dislocation radiation

D3 and D4 are characteristic for transition between the dislocation one-dimensional bands, while D1 and D2 are related to an interaction of the dislocations with metal contamination. Although, the impurities at the dislocation core are not efficiently gettered, it could be expected, that after PDG the dislocations will become less contaminated due to a removal of the impurities in the dislocation cloud. As a result, the radiation D1/D2 should be suppressed, while D3/D4 should increase.

The spectra of n-type EFG samples in as-grown state and after PDG are given in Figure 4.14. Indeed, at 80 K, D3 and D4 dominate the sub-band-gap luminescence from PDG treated sample, while D1 and D2 are almost not present. Oppositely, in the 80 K spectrum of as-grown sample, the defect luminescence in the range of 0.8 - 0.9 eV (D1 and D2) is stronger than that of D3/D4. Moreover, the defect luminescence in the range of 0.8 - 0.9 eV from PDG treated sample remains up to room temperature and is stronger than that from as-grown sample in the entire temperature interval 80 – 300 K.

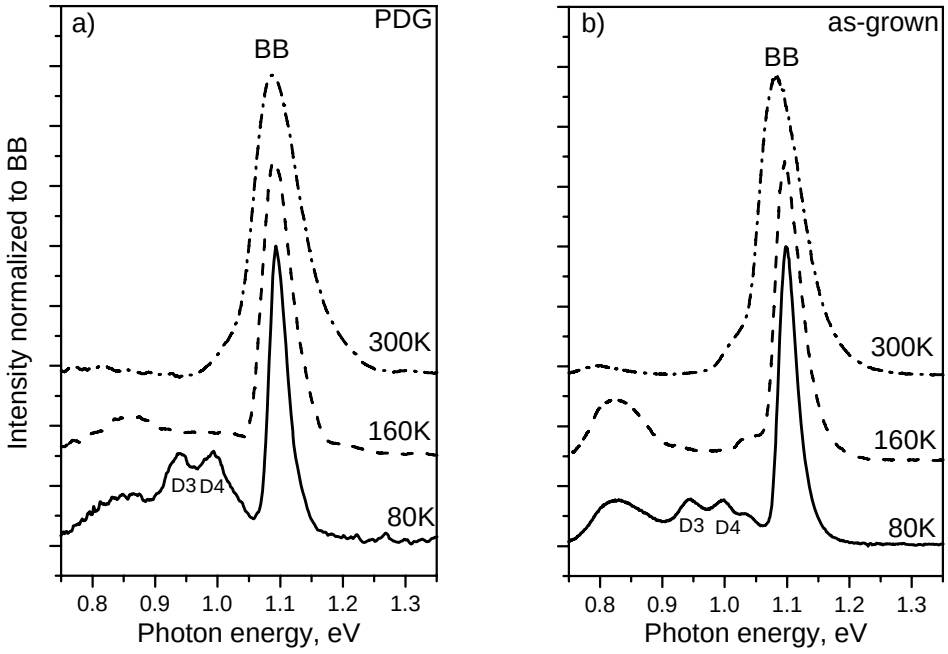

Figure 4.14. Typical spectra taken from the n-type ribbon samples and normalized to the band-to-band intensity. a) The samples subjected to phosphorous diffusion gettering show distinct D3 and D4 features at 80K and the defect luminescence in the range of 0.8 - 0.9 eV is relatively weak. b) As-grown sample exhibit defect related luminescence in the range 0.8 - 0.9 eV, which is well detectable even at room temperature.

It seems that the D1 and D2 are influenced by impurities loosely bound to the dislocation, which can be removed by the gettering. Both lines are related to the presence of the impurity cloud at the dislocations. After PDG, the impurity cloud is removed [Kit2004a] and D1/D2 luminescence becomes less. This suggestion is supported by the cathodoluminescence

observations of Higgs et al., showing that the D1 and D2 lines appear in the vicinity of the dislocations and D3 and D4 close to the dislocation core [Hig1992a].

One can expect that the D1 and D2 lines will be strongly influenced by the surrounding in which the dislocations are (local electric field, mechanical stress). It can be expected that the dislocations in different regions of an EFG sample "see" different local surroundings, and this should have an influence on their D1 and D2 radiation. In contrast, D3 and D4 originate from the dislocation core and should not be influenced by the local surrounding. That can be proven by analysing the profile of the intensities of the dislocation lines along a defect-rich region, in which the dislocations appear in different surroundings due to the local inhomogeneities of the material.

4.4. Relation between D3 and D4 spatial distribution of intensities

It was pointed out (Chapter 2) that the dislocation emission lines behave as pairs in many aspects. One can verify the relation between them, taking advantage of the inhomogeneity of the EFG material.

4.4.1. Spatial distribution of D band luminescence

The inhomogeneity of the EFG sample allows to study the relation between the intensity of the dislocation radiation from dislocations situated in different local environment. As the local conditions for the dislocations vary from point to point, one can expect also variations in the intensity of the lines. It is of special interest the intensity relation between D1 and D2 as well the relation between D3 and D4, because it has been considered that those behave in many aspects as pairs. Figure 4.15 shows two profiles of the ratios of the peak areas for D2/D1 and D4/D3 measured in a defect-rich area on p-type EFG sample.

The intensity ratio of D4/D3 is nearly constant (close to one), over the whole investigated range. In comparison, the D2/D1 one is very scattered and there is no detectable correlation in their peak areas across the sample. This result confirms the relation between D3 and D4, but it rather disproves a relation between D1 and D2 (Chapter 2, 2.2.5).

D1 and D2 intensity variation along the sample is caused due to their sensitivity to the environment of the dislocations. The dislocation vicinities are stronger influenced by the neighbouring dislocations and the local conditions (dislocation density, material stress) than the dislocation cores, thus the local conditions affect the D1 and D2 to a greater extend than D3 and D4.

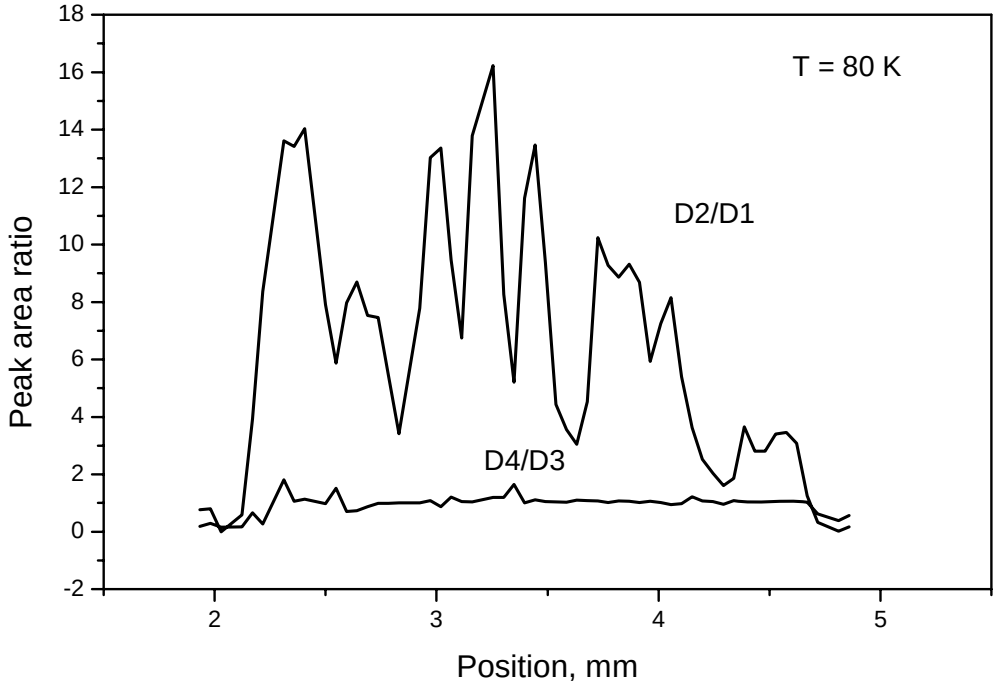

Figure 4.15. Spatial distribution of D2/D1 and D4/D3 peak area ratios along the defect part of the sample between position A and B (see Fig. 4.6) at 80 K. D2/D1 strongly varies, where D4/D3 remains nearly constant.

4.4.2. Exception in the spatial correlation of D3 and D4 intensities. Indication for high residual mechanical stress.

In some cases the correlation between D3 and D4 lines seems to be violated. Figure 4.16a reveals an area, where the intensity of the D4 line exceeds the intensity of the D3. The area of peculiarly strong intensity follows the typical pattern of the crystalline grains. A closer look at the low temperature spectra (Figure 4.16b) shows that the effect is caused by an additional peak close to the D4 line, which influences the overall intensity of the radiation at that energy (1.0eV). That additional peak can be related either to phonon replica of the band-to-band or to radiation from defects.

Emission in the same energy range has been reported. A photoluminescence peak at about 1.04 eV has been observed from CZ silicon, subjected to several hours annealing at 650°C, under compressive stress of several GPa [Bin2005y]. The appearance of that peak correlates with the formation of individual self-interstitials or clusters. Silicon subjected to irradiation with electrons shows distinct features in the range 1.03 - 1.1 eV of the spectrum, which can be related to the formation of self-interstitials, too [Dav2002]. The X line (1041 meV), related to interstitial complexes, fits quite well to the observed spectral feature. However, the line observed on multicrystalline silicon is well detectable at temperatures up to about 100 K and does not deactivate rapidly with temperature. In contrast, the implantation-induced and the

electron-irradiation-induced radiative transition are rapidly quenched with temperature due to thermal ionisation of the very shallow electronic states in the band gap. Thus, the line at 1.04 eV is probably not related to point defects, but presents a band-to-band phonon replica.

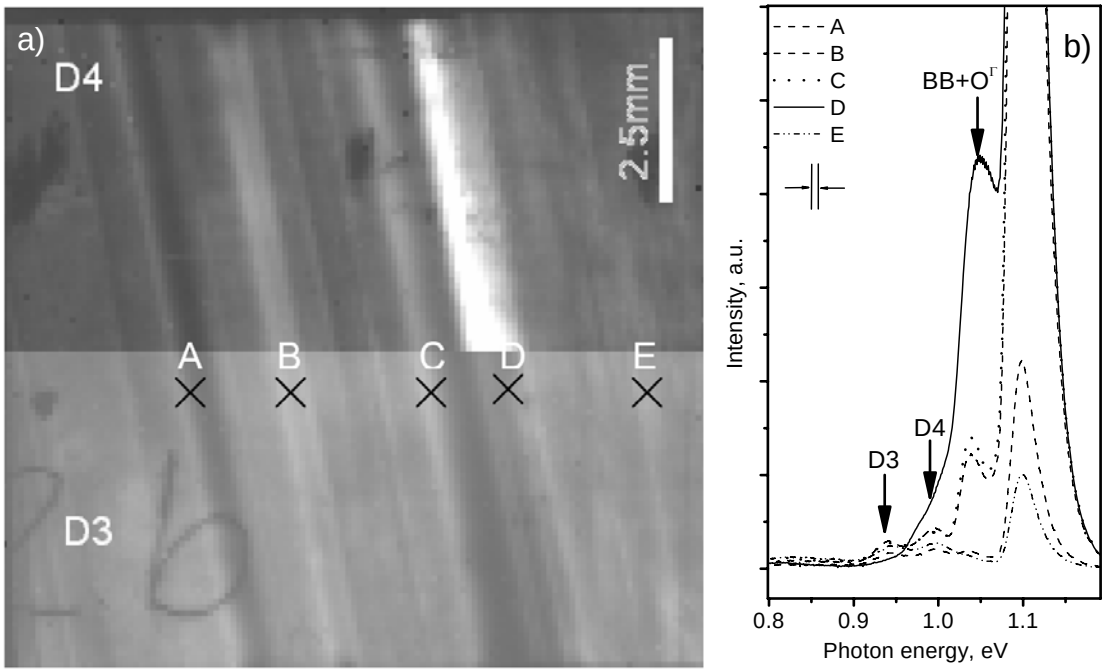

Figure 4.16. Correlation between D3 and D4 lines at 80K on n-type EFG in as-grown state. a) photoluminescence intensity maps of D3 (upper half) and D4 (bottom half). The letters A to E indicate the positions, where spectra are taken. b) photoluminescence spectra at the marked positions. The spectral width of the slit is indicated.

The silicon band-to-band radiation (one phonon assisted) is always accompanied by additional low energy peaks, which we attribute to multi-phonon assisted band-to-band transitions. The two phonon assisted peak has usually about ten times lower intensity [Tru2003, Vou1977], when compared to the band-to-band one and has similar non symmetric shape (Figure 4.17). It is either directly generated by band-to-band transition assisted by two phonons or is a result of a Raman Stokes shift of the band-to-band emission. In both cases two phonons are involved in the process. Measurements on FZ silicon at 80K show that also third peak with intensity one hundred times lower than that for band-to-band emission can be detected and ascribed to a three phonon assisted process (Figure 4.17) [Tru2003]. That third peak lies very close to the position of D4 line and at high temperatures, where all peaks are broadened, the two and three phonon assisted band-to-band gives a significant contributing to the intensity, measured at the D4 spectral position [Arg2007].

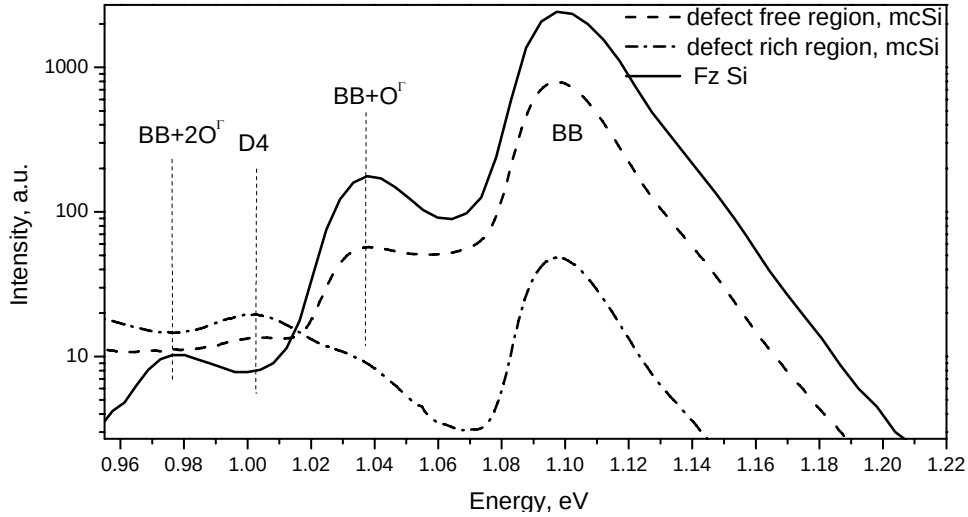

Figure 4.17. Comparison of the spectra in defect-rich and defect-free regions of p-type EFG sample with a spectrum of FZ-Si. Two lines related to multiple O^{Γ} phonon assisted band-to-band recombination are observed.

On places where the two and three phonon recombination is high, a quasi-enhancement of D4 intensity can be expected. Thus, at position 'D' marked on the map (Figure 4.16a), the intensity of the two and three phonon assisted peaks are much higher than those observed from the other positions (Figure 4.16b).

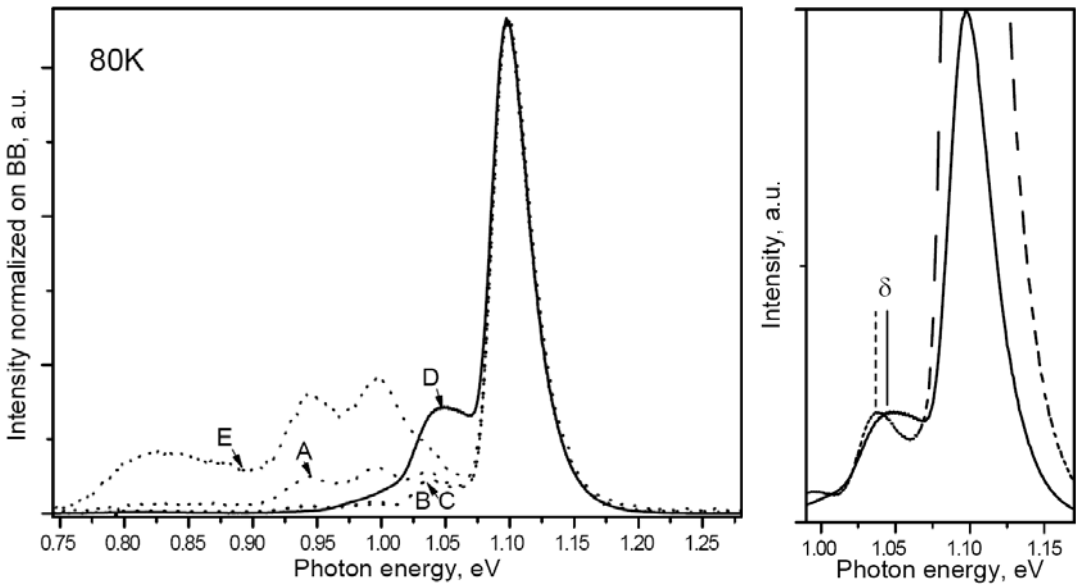

Figure 4.18. a) Spectra, normalized on band-to-band peak maximum, taken from the sample before PDG. The position D shows a strong feature at ~1.04 eV, which we relate to enhancement of the two phonon assisted radiative recombination. b) Intensity normalised on band-to-band luminescence shows a shift of the two phonon line, which indicates lower phonon energies.

The relation between band-to-band and phonon assisted peak intensities is about 4:1 (Figure 4.18a), not 10:1 as it is usually observed. The peak appears also slightly shifted (Figure 4.18b) to higher energy and lies closer to the position of the band-to-band one. If one assumes, that an

O^{Γ} phonon is responsible for the shift, its energy should be 10 meV less than that on standard silicon (64 meV at 80 K). Such lowering of the phonon energy we relate to a mechanical tensile stress of ~ 5 GPa [Dew1996].

The non correlation between the intensities of D3 and D4 in that case indicates a residual stress and is not caused by a violation of the relation between both lines, it appears due to strong multi-phonon mediated band-to-band luminescence.

4.5. Summary

There is a correlation between the dislocation recombination activity and their room temperature luminescence, which allows to use photoluminescence mapping for finding the dislocation rich regions in multicrystalline silicon. The dislocation and band-to-band luminescence are essentially anticorrelated. The band-to-band intensity is related to the diffusion length of minority carriers. However, it cannot be used for quantitative measurements without knowing the surface recombination rate. The surface recombination influences the luminescence intensity. If it is not homogeneously distributed, the information obtained by the band-to-band luminescence mapping is not related to the diffusion length of the carriers, but to the surface recombination. The enhanced surface recombination suppresses the dislocation-related radiation and the band-to-band radiation in equal extend.

- Anomalous temperature behaviour of band-to-band luminescence was observed on n-type EFG samples. It was related to the temperature dependent recombination rate of a nonradiative process, determining the excess carrier concentration. Such process can be related to recombination on shallow levels (e. g. dopants or dislocation one-dimensional bands) or to that of dislocations of type 2 EBIC temperature behaviour, in which the recombination through the shallow dislocation level is mediated by a low concentration of deep, impurity related centres in the dislocation vicinity.
- The dislocation lines D1 and D2 can be related to transitions via deep centres. In particular, D2 can be explained by a transition between a deep centre and the three dimensional band of the semiconductor, while D1transition is between a deep level and the dislocation one-dimensional bands. For both the transition is asymmetric. The deep levels are most probably located in the dislocation vicinity, which makes these lines sensitive to the local dislocation environment. Thus their radiation intensity is susceptible to gettering of the impurities.
- The spatial correlation between D3 and D4 is always established. Both appear together at nearly equal intensity. However a quasi non-correlation can appear on sites, where the two and three phonon assisted band-to-band recombination is strong. The strong two and three

phonon assisted radiative recombination appears to be related with a decreased phonon energy due to residual mechanical stress.

Chapter 5

Radiative defects in block cast and HEM silicon

This chapter deals with photoluminescence spatial distribution around grain boundaries and typical defects, detected by means of photoluminescence mapping.

A substantial amount of the materials for photovoltaic applications is produced by block casting and HEM methods [Sch2004]. However, they suffer from diffusing of contaminants from the crucible walls into the silicon ingot during cooling to room temperature. These impurities lead to short minority carrier lifetimes within a region of up to several centimetres in thickness at the borders of the ingot. Segregation of impurities in the melt also leads to their high concentration in the upper part of the block. Usually, the contaminated regions are removed, but because of fixed ingot and wafer sizes, deteriorated regions are sometimes also found in processed solar cells. Wafers of n-type HEM and p-type block cast silicon are examined by photoluminescence in order to find, which defects are specific for these types of materials.

5.1. Gettering zone around grain boundaries

In contrast to foil growth, the material obtained by crystallisation in blocks is subject to a relatively long cooling-down. The large amount of material requires lower solidification rates typically of order of 1 cm/h (weight rate for large ingots of about 10 kg /h) [Koch2003] and correspondingly long cooling time for the solidified material in order to prevent large temperature gradients and related thermally induced stress and cracks in the material. The structural defects in the crystal are sinks for the contaminants diffusion flow. Thus, gettering processes at the grain boundaries can occur during the cooling, leading to gradients in the concentration of impurities within the grains. Accordingly, a gradient in the recombination

activity could be expected. In the gettered areas, the total recombination activity should be low and the radiative recombination should be increased.

Figure 5.1 compares a band-to-band intensity map with an EBIC micrograph both taken on a sample from the bottom part of an n- type HEM wafer. Similar getter zones are found on bottom wafers of p-type, boron doped material, too (Figure 5.1d).

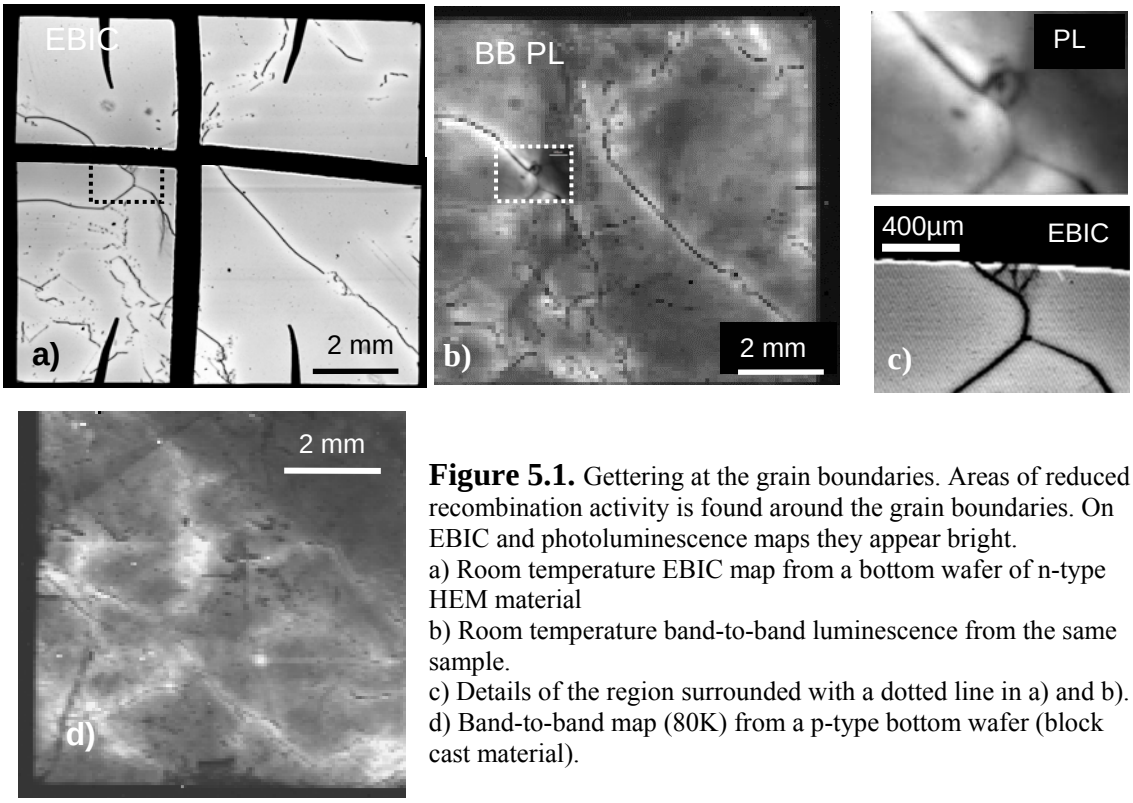

Figure 5.1. Gettering at the grain boundaries. Areas of reduced recombination activity is found around the grain boundaries. On EBIC and photoluminescence maps they appear bright.
a) Room temperature EBIC map from a bottom wafer of n-type HEM material
b) Room temperature band-to-band luminescence from the same sample.
c) Details of the region surrounded with a dotted line in a) and b).
d) Band-to-band map (80K) from a p-type bottom wafer (block cast material).

Both, EBIC and photoluminescence mapping reveal a bright halo around the grain boundaries. The haloes are zones with increased minority carrier lifetime and are usually related to gettering of metallic impurities at the grain boundaries. Such haloes have been often reported in EBIC micrographs of p-type multicrystalline material [Kit1995c, Kit1995a] and their appearance has been related to iron impurity gettering at the grain boundaries.

5.2. $\beta FeSi_2$ precipitates

Due to the slow cooling rates of the blocks during their crystallisation and the low solubility of the interstitial metallic impurities in silicon, not only gettering at the grain boundaries, but also formation of precipitates can occur.

Iron disilicide exhibits radiative properties and can be detected by photoluminescence. It has two stable polymorph phases orthorhombic β-phase and tetragonal α-phase [Mae1995, Gri1992]. The α–phase is metallic one and cannot contribute to the luminescence. The

β−phase is a quasidirect semiconductor, with an indirect band gap of 0.8 eV and a direct one, several meV wider [Fil1996, Fil1998]. Strong radiation related to $\beta FeSi_2$ has been observed only, when it is in form of small inclusions in silicon. Epitaxially grown films and bulk material exhibit low or no photoluminescence [Tak2004].

Metal inclusions and metal silicides are often detected in the multicrystalline silicon materials [Buo2006]. Usually, X-ray fluorescence microscopy is used to locate metal-rich particles and to determine their spatial distribution, elemental composition, and dimensions. A combination of this technique with X-ray beam induced current [Vyv2002] allows to correlate the location of the precipitates with the position of the recombination-active structural defects (dislocations and grain boundaries). Studies on multicrystalline material [Vyv2002, Buo2006] have shown that iron is predominantly concentrated at the grain boundaries in oxidised form (Fe_2O_3) or in form of silicide ($FeSi_2$). The first type builds larger precipitates containing other metallic impurities (Ca, Mn, Cr, Ti), while the second one forms nanoprecipitates of pure $FeSi_2$.

Block crystallised silicon exhibits a non uniform distribution of the contaminants along its direction of growth. Thus iron has been found to have its maximal concentration near the bottom of the block [Mac2005] mainly in form of precipitates. At the top of the block, it is mainly dissolved, forming interstitials in the silicon lattice.

5.2.1. Precipitates in n-type HEM sample

The sub-band-gap luminescence maps at low temperature from the bottom wafer of n-type HEM material show high intensity at some positions. The sub-band-gap luminescence there exceeds the band-to-band one of up to two orders of magnitude. Figures 5.2a and 5.2b compare two maps taken at 80 K one at spectrometer set to band-to-band (1.1 eV) and the other to the radiation at 1.0eV, where the D4 line is usually expected. The band-to-band luminescence map shows, clearly, the positions of the grain boundaries and the surrounding gettering zones. The sub-band-gap radiation map exhibits areas of intense luminescence radiation, which even saturate the detector. Two of these positions on the samples, where the centres of strong signal are concentrated and observed in several neighbouring scans, are measured spectrally resolved. The spectra are given in Figure 5.2b together with a typical spectrum obtained from a $\beta FeSi_2$ precipitate layer embedded in silicon matrix [Sch2003]. The broadening and the shift of the peaks obtained from the multicrystalline silicon as compared to the reference are probably related to the higher temperature of the sample at which the spectra are recorded, but the characteristic features of the peaks are similar to those observed in [Sch2003].

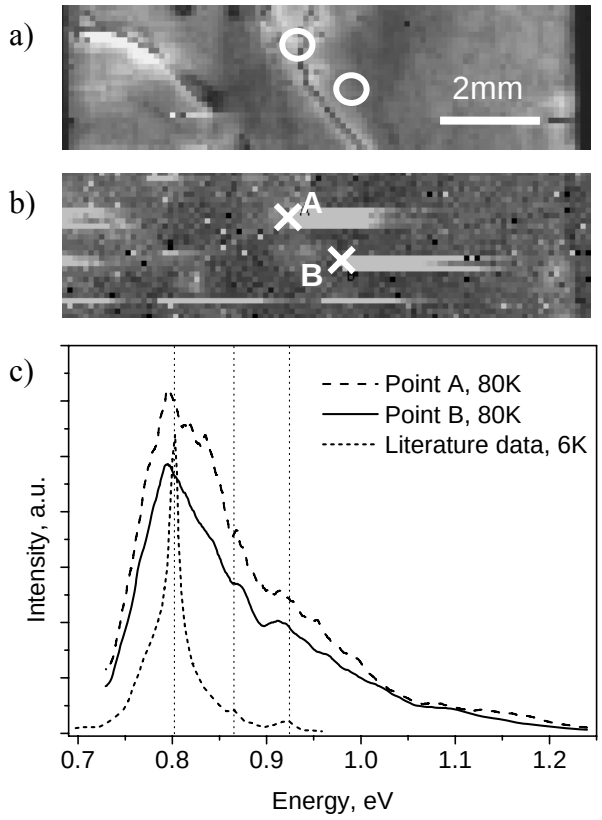

Figure 5.2. Luminescence from iron silicide precipitates embedded in n-type HEM silicon. a) Map of band-to-band luminescence intensity at 80 K. b) Map of the luminescence at 1.0 eV at 80 K. The positions marked 'A' and 'B' show very intense radiation, which saturates the detector. The white stripes on the image are artefacts caused by the saturation and the slow recovery of the detector, which is interpreted by the system as a signal coming from the next scanned points. c) Resolved spectra at position 'A' and 'B' reveal a very strong luminescence at about 0.8 eV. The spectra are compared to that from $\beta FeSi_2$ given in [Sch2003].

5.2.2. Precipitates in p-type block cast sample

Iron silicide precipitates are found not only n-type HEM, but also in p-type block cast materials. Figure 5.3 shows maps of the luminescence taken at 80 K on a wafer from the bottom part of a p-type block. The arrows on the band-to-band map in Figure 5.3a indicate the positions of $\beta FeSi_2$ precipitates, which were found by spectrally resolved measurements. Due to the long tail of their characteristic peak at 0.8 eV towards the high photon energies it is possible to detect the precipitates also with spectrometer set at 1.1 eV in case the overall band-to-band luminescence from the sample is low. Figures 5.3b and 5.3c show better resolved maps of a region where a precipitate is found. Very strong luminescence at 0.8 eV is detected. The size of the areas emitting intense luminescence at 0.8 eV is determined by the size of the spot of the excitation laser (diameter ~100 μm) and not by the size of the precipitates. It is unclear whether these regions contain one or more precipitates, because the lateral resolution of the scanning luminescence is limited due to the diffraction and is not sufficient to resolve nano-sized particles.

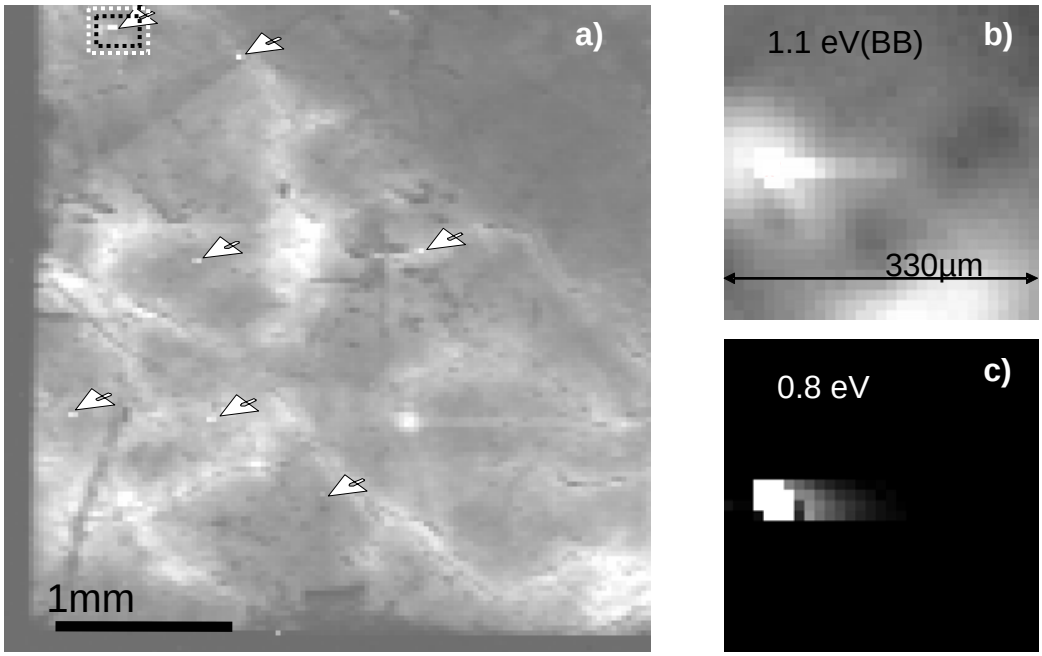

Figure 5.3. Band edge luminescence map from a bottom wafer of a p-type block cast material taken at 80 K. a) The arrows on the picture indicate the positions where $\beta FeSi_2$ precipitates are detected. Maps are taken at higher resolution from the region indicated by a rectangle.
b) Detail of a), showing an increased radiation at 1.1 eV from the precipitate in comparison to the surrounding.
c) Very strong luminescence at 0.8 eV is observed from the same precipitate. The defect luminescence at 0.8 eV from the region surrounding the precipitate is negligibly small. That is why in image c) it appears dark.

No correlation can be observed between the position of precipitates and the grain boundaries shown as dark lines surrounded by a brighter gettering zones on Figure 5.3. The precipitates appear predominantly inside the grains. At first glance this observation contrasts to the findings in [Buo2006], where precipitates are detected mostly at the grain boundaries. Two different reasons can cause such behaviour. First, there is luminescence from only one of both $FeSi_2$ polymorphs. If one assumes that the iron disilicide at the grain boundaries predominantly precipitates in its α-phase and in the grain bulk in its β-phase, then no luminescence from precipitates at the boundaries can be expected. However, a mechanism is not known, which can select one of the phases to be dominant at the grain boundaries and the other in the grain bulk. The second possibility is that charge carriers generated at the grain boundaries recombine nonradiativly through interfacial states. This recombination route is much more efficient than other recombination processes like band-to-band radiative recombination or recombination at iron silicide nanoprecipitates. The nonradiative recombination at the grain boundary prevails over all radiative processes there, and that can be the reason why the precipitates at the grain boundaries do not emit light.

Figure 5.4a shows temperature dependence of spectra measured at the point marked in Figure 5.3a. All spectra show a maximum at about 0.8 eV with a broad shoulder towards large

energies. Their intensity decreases upon increasing temperature and is not detectable at 160K. The luminescence in the sub-band-gap region of the spectra fluctuates strongly.

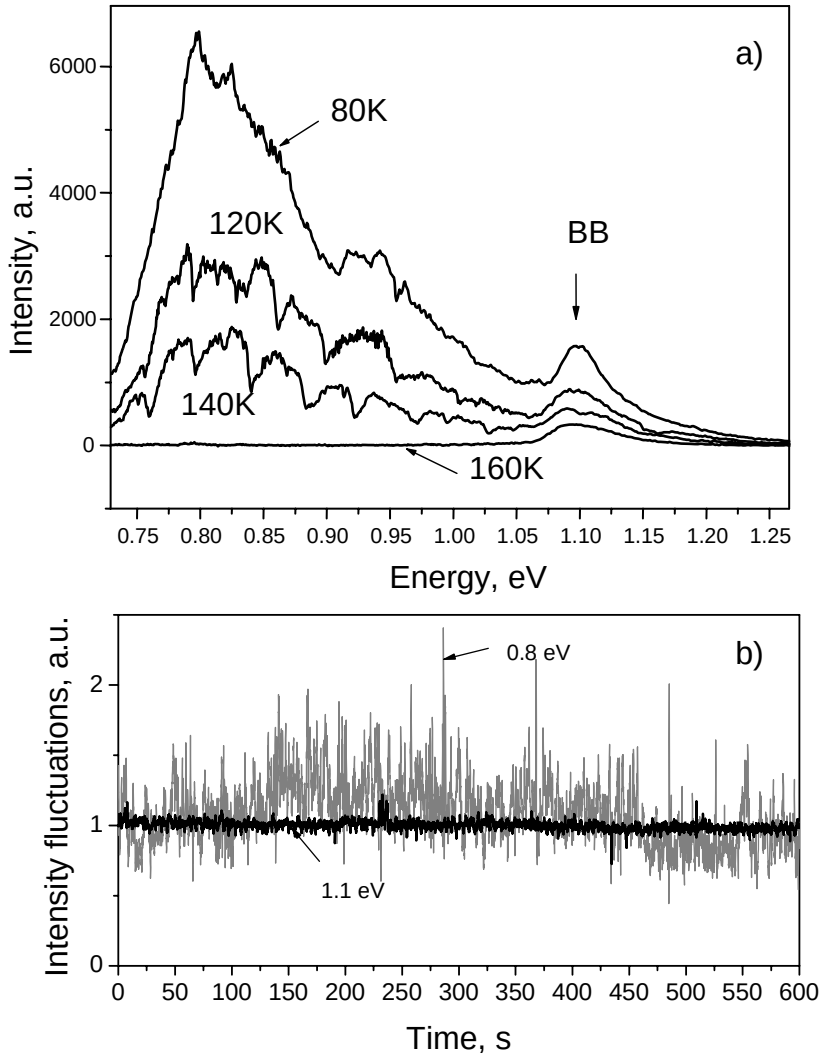

Figure 5.4. Spectral and time dependent measurements at the position showing strong luminescence at 0.8 eV, marked on Fig 5.6. a) Temperature dependence of the spectra. The luminescence at 0.8 eV is maximal at 80K and disappears at about 160 K. As shown in b) the modulation may be due to strong temporal fluctuations during the scan, indicating "blinking".
b) Fluctuation of 0.8 eV radiation and band-to-band radiation measured at 80K. The diagram compares the intensities normalized on the corresponding mean value.

It has been reported [Efr1997, Ban1999] that isolated semiconductor nanocrystals show typically blinking luminescence under continuous wave excitation, where the nanocrystals alternate between 'on' (luminescent) and 'off' (non-luminescent) state. The 'on' and 'off' periods stochastically vary resembling random telegraph noise. The origin of that behaviour is still a subject of research. The model presented in [Efr1997] relates the 'off' periods with the times when a nanocrystal is ionized and the luminescence is quenched by nonradiative Auger recombination. Thus, the duration of the 'on' periods depends on the ionization rate of the nanocrystal via thermal or Auger autoionization.

Figure 5.4b shows a comparison of the time dependences of the band-to-band and the defect luminescence. It is seen that the defect luminescence shows flickering, while band-to-band luminescence remains nearly unchanged. The 'noise' in the defect luminescence can be related to the typical blinking observed from quantum dots. The areas emitting strongly at 0.8 eV probably contain one or several $\beta FeSi_2$ precipitates, which are responsible for the fluctuation of the luminescence.

It has been frequently discussed in the literature whether the light emission in iron silicide containing samples is really due to radiative recombination in the silicide phase [Sch2003, Tak2004, Spi2000, Gao2003] or due to dislocations. First, the precipitates are never produced alone, without presence of extended defects, and second, their radiative recombination is expected in the spectral region, where the D1 line appears. The characteristic blinking luminescence originates from $\beta FeSi_2$ precipitates and not from dislocations. Such blinking has not been reported for dislocations. It can be used as an indication, whether a 0.8 eV emission is caused by presence of precipitates or dislocations.

5.3. Very intense, D3-like emission

Defect-related emission in the range 0.93-0.95 eV (spectral position of D3) is observed from a sample from the middle part of the p-type block. The images in Figure 5.5a,b present maps of the luminescence at 80 K recorded at photon energies 0.94 eV (a) and 1.1 eV (b). The defect-related radiation (bright on Figure 5.5a correlates with the positions of the grain boundaries, which appear as dark lines on the band-to-band luminescence map in Figure 5.5b.

However, detailed spectra taken from different positions differ substantially. As it is seen in Figure 5.5c, there are areas showing two lines (D3 and D4) of almost equal intensity in the sub-band-gap energy range of their spectra. Those areas are marked in the images in Figure 5.5a and 5.5b with circles. Other areas (marked with crosses) show instead, only one peak in the range 0.93 – 0.95 eV. It is seen (Figure 5.5c and 5.5d), that the new line is more intense than the typically observed D3. On some spots, its intensity is even higher than that of band-to-band radiation. The spectral position of the line, taken from different spots varies in the range of 0.93 to 0.95 eV. We consider new spectral feature as a defect related radiation, different from D3. Because it is in the spectral range of D3 we refer to it as very-intense-D3-like radiation (VID3).

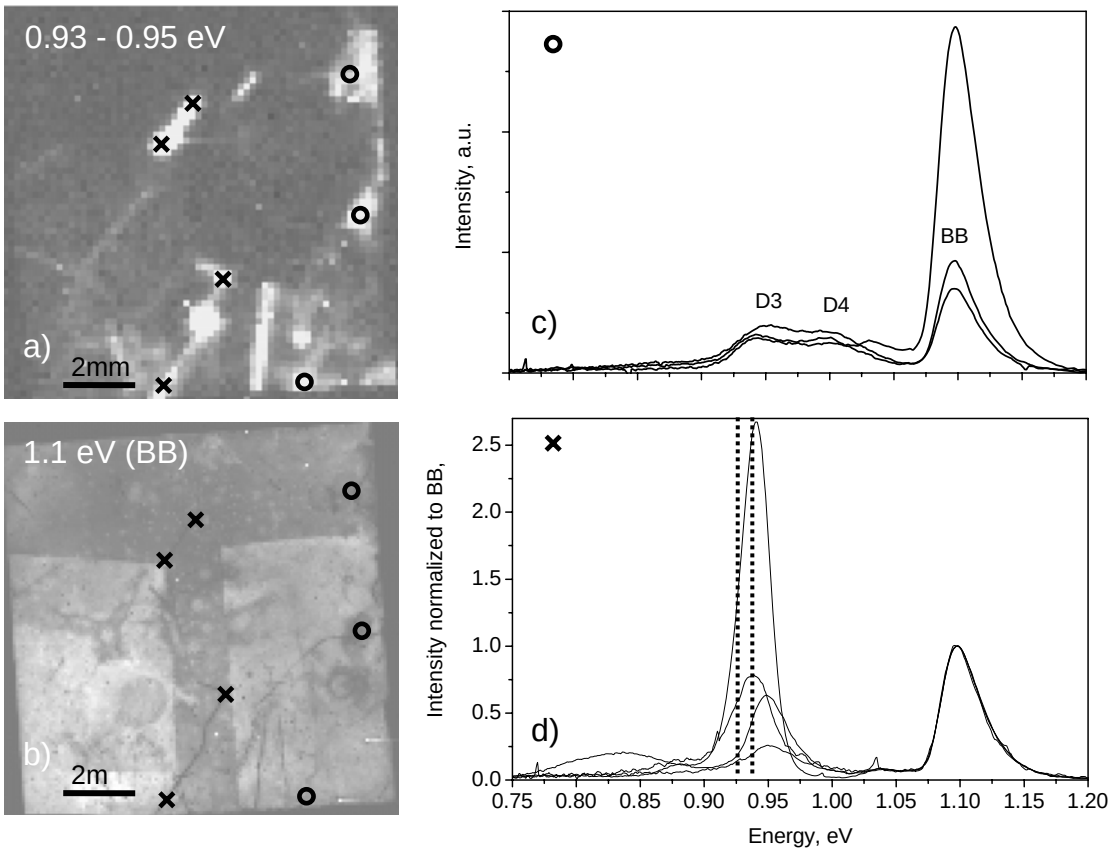

Figure 5.5. Intense luminescence at about 0.93 - 0.95 eV observed at 80K on a sample from the middle part of a p-type block silicon.
a) Map taken at spectrometer set at 0.94 eV (D3 line). The positions marked with circles show typically D3, D4 and band-to-band peaks in their spectra. Those marked with crosses typically show one peak at about 0.93 - 0.95 eV in the sub-band-gap part of the spectrum.
b) Map taken at spectrometer set to band-to-band (1.1 eV). The regions of strong defect luminescence correlate with the grain boundaries revealed in the band-to-band luminescence map. (Note that both brighter rectangular areas are artefacts due to lowered surface recombination).
c) Detailed spectra on the positions marked with circles.
d) Detailed spectra, normalized on the band-to-band, taken at the positions marked with crosses

Cathodoluminescence micrographs of one of the areas emitting VID3 are shown in Figure 5.6. The radiation is found at a grain boundary and is inhomogeneously distributed along its length. The presence of a VID3 line in the spectra is found to be independent on the doping type. It is observed in p-type block cast as well in n-type HEM samples. Although, spectrally, VID3 lies very close to D3, its temperature behaviour is different. Figure 5.7 shows the evolution of the spectra upon increasing the temperature. VID3 sustains up to temperature of 240 K, while D3 is usually detected only below 130 K. This fits well to a behaviour described by bound to bound transition Eq. (1.27) with deactivation energy of 117 meV.

The band-to-band luminescence in the spectra remains nearly constant within the entire temperature range.

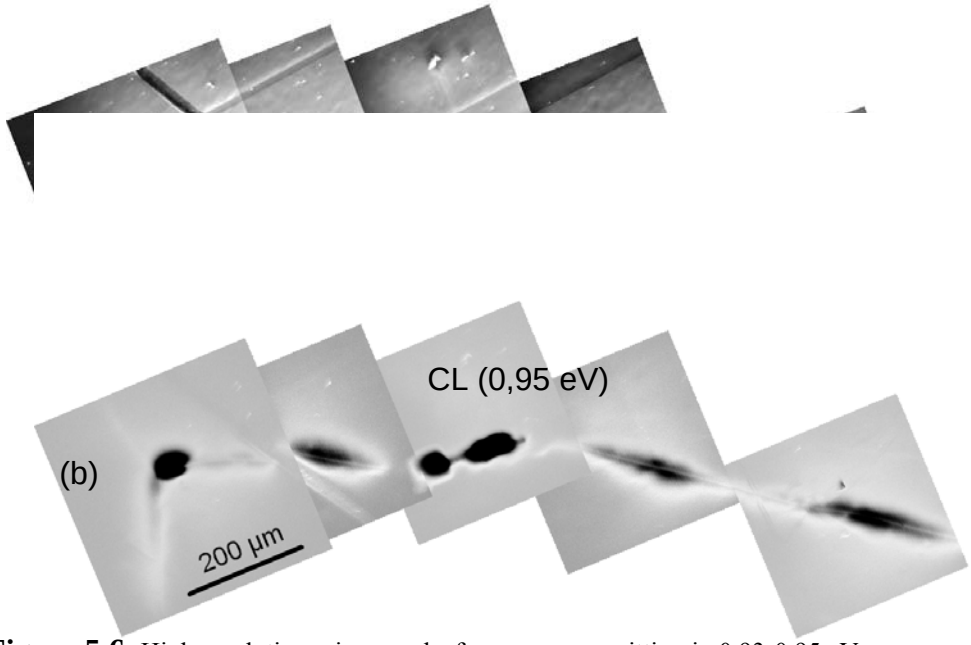

Figure 5.6. High resolution micrographs from an area emitting in 0.93-0.95 eV range.
a) Scanning electron microscope image. The line of black point marks a grain boundary.
b) Cathodoluminescence image from the same area, taken at spectrometer set at 0.95 eV at 80 K. The grain boundary marked in a) shows strong radiation. (The positions appearing dark on the micrograph show strong luminescence, overloading the detector).

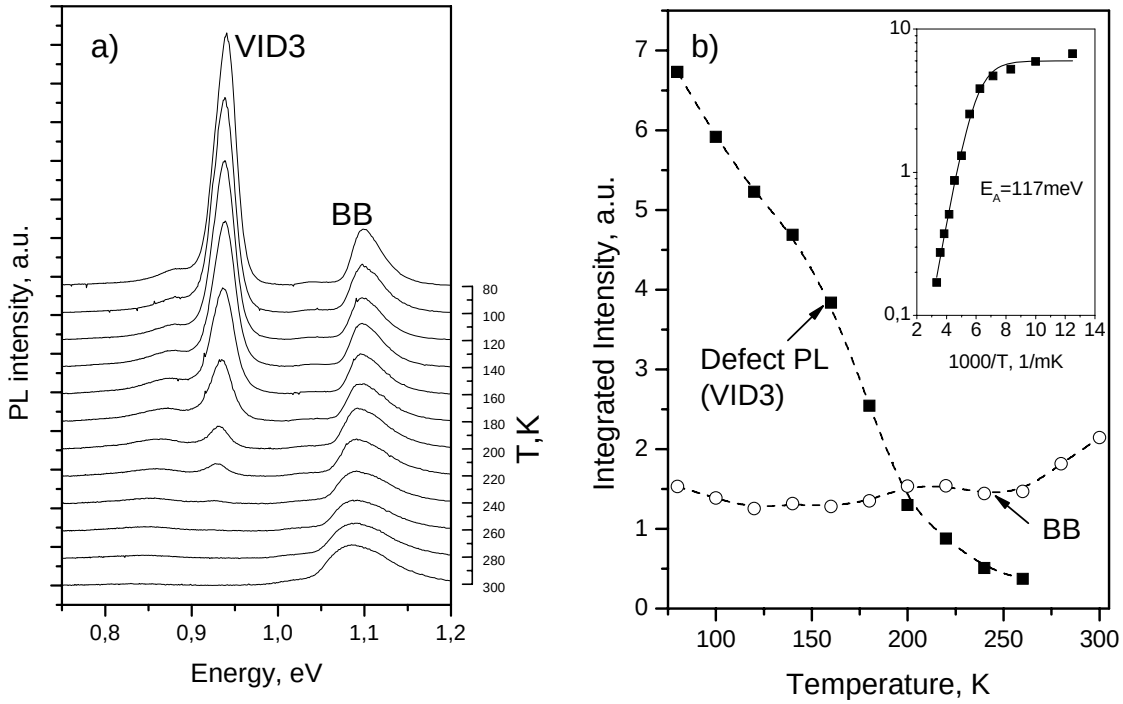

Figure 5.7. Temperature dependence of VID3 in n-type block cast material.
a) Evolution of the spectra upon increasing the temperature. The radiation at about 0.94 eV is the most intense feature in the spectrum at 80 K and is observable till 240 K.
b) Dependence of the integrated intensity of the band-to-band radiation and the defect radiation on temperature. The inset of the curve shows an Arrhenius plot of the intensity of defect related radiation. The deactivation energy estimated from the fit is 117 meV.

Four possible reasons were considered as origin for VID3 radiation:

1) *Dislocation and their modification upon mechanical deformation at low temperature*

It has been pointed out that non-relaxed dislocations, produced by a two-steps deformation, can give rise to D5 and D6 lines [Saue1985, Saue1986]. At low temperatures and high excitation levels, D5, which is nearly at the same spectral position as VID3, exhibits strong intensity. Unfortunately, there is no data in the literature on the temperature behaviour of D5, so there is no possibility to compare the temperature behaviour of VID3 and D5. However, as it is seen in Figure 5.6, there is a micro-crack formed nearby the VID3-emitting grain boundary. This crack is a result of stress release in the sample, and indicates a possible, low temperature deformation, occurred after its formation. The dislocations, created at high temperature, during the formation of the grain boundary, are subjected to a deformation at low (room) temperature after the formation of the crack. This deformation, possibly, drives the dislocations out of their relaxed state and causes them emitting D5 (VID3) radiation.

2) *Carbon contamination*

Strong luminescence at 1.3 μm (0.95 eV) can also be due to carbon contamination. The G line [Hay2004, Can1987, Dav1989], related to presence of carbon in silicon as a complex of two carbon atoms in substitution and interstitial state, can be even stronger then band-to-band in range of temperatures from 4.2 to 77 K [Bro1986]. Carbon is a contamination commonly present in block cast silicon. Its concentration in the material is usually far above its solubility. The source of carbon in ingots is both: carbon present as contaminant in the feedstock and carbon monoxide from the furnace environment [Sch2004]. However, luminescence from carbon related defects has been usually reported after implantation or irradiation with electrons. In the experiments reported here the samples have not been subjected to such treatment. It seems less probable that VID3 has its origin in carbon related centres.

3) *Copper contamination*

The spectrum of copper in silicon consists of a narrow no-phonon line, observable at temperatures below 20 K, which is replicated at lower energies by successively broader and weaker satellites, phonon-shifted to lower energies. That sharp line structure is superimposed on a broad band, centred at about 0.95 eV. The broad band alone persists at temperatures above 80 K [Web1982]. Despite the conscience of the spectral position to that of VID3 and thermal stability of the luminescence, one can consider copper as less probable candidate for the origin of VID3 radiation. The fact that the luminescence is observed on a wafer from the middle part of the block and that the dislocations, which are found in the surrounding material, are rather "clean", emitting predominantly D3 and D4 lines (Figure 5.5c), implies that the concentrations

of metallic impurities there is low. Thus, such extended regions contaminated with copper, (Figures 5.5a and 5.6) are improbable to be found close to clean dislocations, taking into account that copper is a fast diffusing element in silicon.

4) *Chalcogen impurities (S or Se)*

Strong luminescence from samples containing sulphur has been reported by Brown and Hall [Bro1986]. It has been found that there is no dependence on how the sulphur is introduced into the silicon, whether by diffusion or implantation and annealing. It gives rise to a peak at 1.32 μm (0.94 eV), which has deactivation energy of 139 meV. Selenium exhibits similar properties in silicon [Bra1998] - a peak at about 1.34 μm (0.925 eV) and deactivation energy of 113 meV. A general property, characteristic for both species, is their strong luminescence persistent at temperatures well above 80 K [Bro1986, Bra1998]. Maximal radiation intensity, exceeding the band-to-band one has been observed at about 80K.

The observed here deactivation energy (117 meV) and the position of the peak (0.95 eV) correspond to those reported for sulphur and selenium equally well. Strong sub-band-gap luminescence, persisting up to temperatures above 80 K is observed, too. According to these characteristics the observed VID3 line may be related to the presence of sulphur or selenium.

There is still a potential for more accurate identification of the VID3 related defect. Its relation to sulphur or selenium cannot be unambiguously proven by luminescence measurements, obtained at elevated temperatures. Below 10 K, the photoluminescence spectra of silicon containing these species should show additional features in the spectral range 0.80 – 0.85 eV [Bec1989, Hen1994].

5.4. Summary

Gettering zones around the grain boundaries are observed in both n-type HEM and p-type block cast material. They can be revealed by photoluminescence mapping of band-to-band intensity at room temperature. The presence of precipitated iron indicates that also iron dissolved in the crystal exists. Thus the getter zones are most probably due to gettering of iron at the grain boundaries.

The $\beta FeSi_2$ precipitates, showing 0.8 eV luminescence, are detected in the bulk of the grains. Characteristic blinking luminescence is related to the nanometric size of the precipitates.

At the grain boundaries strong radiation in the range 0.93-0.95 eV is detected and its appearance may be related to the presence of sulphur or selenium.

Part III

Silicon based light emitters

Chapter 6

Light emitting diodes based on silicon - different approaches

In this chapter, the use of silicon as a light source material is discussed. Different approaches are considered in view of their applicability for the on-chip optical interconnect.

Though an electrically pumped silicon based laser is still not available, work is being done worldwide on silicon light emitters in either the visible or the infrared range. To estimate the technological development of the different components is a rather difficult task, but according to the literature data, fast modulators are available working in the range over one GHz with a tendency of improvement of their performance in the next several years [Liu2004]. Waveguides made on silicon basis have been demonstrated and fast Ge detector that can be integrated in the silicon technology are also available [Oeh2006]. The silicon based light emitter is the only missing piece for monolithic integration.

A variety of ideas has been given of how silicon can be adopted for photonic applications. The research field is so broad that a detailed overview of all proposed emitters will go far beyond the frame of this work. In the following section the approaches are reviewed, which have the potential to be realised for light emitters for technological application. The main guiding lines are:

- *Efficient light emission at room temperature.* As the operating temperature of the microelectronic devices is even higher than room temperature, a stable operation of the emitter at room temperature is required, at least.

- *Possibility for electrical pumping at standard CMOS (Complementary Metal Oxide Semiconductor) voltages.* The standard voltages are below 5 V, and in order to use the emitter within a chip such voltages should be sufficient for its operation.
- *Devices should have a restricted size of the active regions*. In order to be coupled to a waveguide, the light should be generated in a defined volume, and not in the entire substrate wafer.
- *Production compatible with the established CMOS technology*. It should be possible to realize the emitter with the existing technology steps, and the device should be capable to sustain further processing steps, necessary for the production of the other electronic components on the wafer.
- *Availability of silicon based detectors, modulators and waveguides for the generated radiation*. The silicon should be transparent for the emission, for application of silicon based modulators and waveguides, which states the upper limit of the photon energy below 1.1 eV. Application of SiGe detectors requires photon energies higher than the Ge band gap (0.65 eV).

From structural considerations, the devices can be separated in three main groups:

- Devices employing *engineered silicon structures*

(Silicon nano structures and porous silicon, Brillouin zone folding in silicon- germanium superlattices, silicon- germanium quantum cascade emitters, and dislocation engineered emitter)

- Devices based on radiation induced by *foreign species embedded in the silicon*

(Semiconducting silicides, erbium emission, emission enhancement due to isoelectronic traps)

- Devices based on silicon *band-to-band radiation*

(Emitters utilizing bulk silicon band-to-band recombination, by applying of different approaches for its enhancement)

6.1. Engineered silicon structures

Structures with nanometric sizes allow to confine electrons and holes in small volume, so that the probability of finding nonradiative pathways for recombination decreases. Band gap and defect engineering additionally increases the probability for radiative recombination.

6.1.1. Silicon nanostructures and porous silicon

Since the discovery of room temperature photoluminescence from porous silicon [Can1990] the attention to quantum confinement effects in low dimensional silicon structures is rapidly growing. The use of porous silicon for devices is difficult because its high internal surface makes it very reactive and sensitive to the ambient conditions. Other systems based on low dimensional silicon structures like quantum dots, wires and wells appear more stable and suitable for technological application. The radiative recombination of excitons in quantum structures is efficient, because the electron and hole wave functions overlap in space. Auger recombination is also subdued due to the space separation of the excitons, unless two of them are created in one nano dot.

The quantum confinement requires embedding of silicon nanostructures in wide bandgap, dielectrics. For efficient electroluminescence, a balance between good light extraction and good electrical conduction should be found. The conduction is usually low due to the presence of the dielectric material. However, electroluminescence even in the visible range has been reported [Tsy1996, Hei2001], but the required high operation voltages (in the order of 10 V and above) are hampering on-chip application.

6.1.2. Brillouin zone folding in silicon - germanium superlattices

The idea of converting an indirect band gap material, like silicon, into a direct one by superimposing a second periodicity over the natural periodic structure of the crystal lattice has been given by Gnutzmann and Clausecker [Gnu1974].

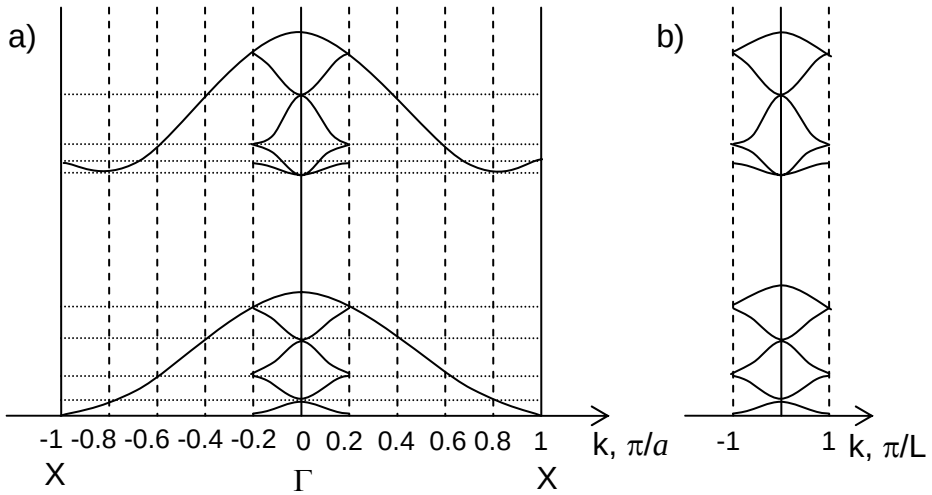

Figure 6.1. Schematic representation of the Brillouin zone folding. a) The periodicity of the superlattice leads to formation of mini-zones in the first Brillouin zone of silicon. The period of the superlattice, *L*, is chosen 5 times bigger than the silicon lattice constant, *a*, in order to obtain the minimum of the conduction band (0.8X in the k space) at the centre of the mini-zone. b) Brillouin zone of the superlattice with direct band structure.

Zone folding is a direct consequence of the new superlattice period imposed on that of the host crystal lattice. Within the first Brillouin zone mini-zones are formed. Their number can be

controlled by the thickness of the superlattice layers. For the right choice of the superlattice period the minimum of the conduction band appear in the centre of one mini-zone (Figure 6.1). Modern epitaxial growth techniques allow the fabrication of such structures by deposition of mixed SiGe layers of altering compositions. However, the effect of enhancement of no-phonon assisted radiative recombination due to zone folding has been observed mainly at low temperatures (5- 10 K) [Fuk1993, Gai1995]. Upon increasing temperature the luminescence rapidly decreases. It turns out that the efficiency is limited by localisation of holes in the germanium-rich layers and electrons in the silicon-rich layers.

The emission wavelength of these devices is in the sub-band-gap region of silicon and is suitable for on-chip application, but the room temperature electroluminescence of light emitting diodes prepared on such structures is below 10^{-3} % [Oss2003].

6.1.3. Silicon - germanium quantum cascade emitters

SiGe quantum cascade emitters are based on intersubband transitions in the superlattice [Pav2003, Oss2003] as it is the case in the quantum cascade lasers based on compound semiconductors.

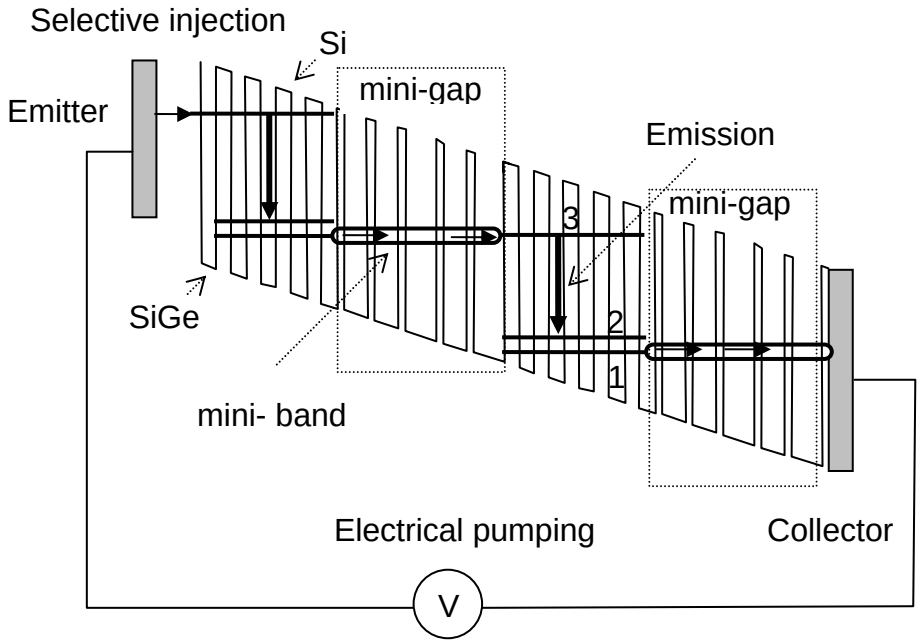

Figure 6.2. Silicon based quantum cascade light emitter (n-i-n device). The cascade is formed by changes in the periodicity in the superlattice, so that mini-bands and mini-gaps are formed. The transition responsible for the light emission is between the levels marked 3 and 2. The transition from 2 to 1 is resonant with a phonon, so that the level 2 is rapidly depopulated. After [OSS2003].

They are produced by epitaxial growth of strain compensated films of Si and SiGe, forming a superlattice. The transition occurs within one band (valence or conduction) and thus overcomes the problem with the indirect band structure of silicon. An example of such structure is shown

in Figure 6.2. Electrons transmited through the device produce multiple transitions in the steps of the cascade. For the intersubband transitions either valence band or conduction band offsets between Si and SiGe layers can be used and thus the highest photon energy of the radiation reported from such devices is about 325 meV [Oss2003]. Such an emitter will be of little use for the silicon photonics unless matching integrated waveguides and detectors are developed and the temperature stability of the radiation is improved, because Si/SiGe quantum cascades show electroluminescence only at temperatures below 80 K.

6.1.4. Dislocation engineered emitter

Dislocations formed in a controllable manner in silicon can significantly influence its radiative properties. They can either contribute for enhancement of band-to-band luminescence or their characteristic radiation can be utilized for a light emitter [Ng2001, Kve2005]. It was shown in the first part of this work, that the dislocation-related radiation D1 in some cases persists up to room temperature (Chapters 4 and 5). The D1 emission generated in regions of high dislocation density can be utilized for light emitting device [Kve2005]. Dislocation in defined regions within the wafers can be produced by implantation and annealing, wafer bonding, or by epitaxial growth of SiGe. Their formation does not require foreign species and they are capable to sustain high temperature treatments. An important advantage of the emitters based on dislocations is that they can be produced within standard processing technology, and the voltages necessary for electroluminescence are within 1-2V, due to the application of p-n junctions for carrier injection [Ng2001]. The electroluminescence is stable and efficient up to room temperature.

In the following chapters, we will discuss the role of the dislocation for the improvement of the luminescence of silicon in more detail.

6.2. LEDs based on radiation induced by foreign species

One other approach is doping with metals, giving strong luminescence. The foreign species can form either silicide precipitates or individual ions in the matrix.

6.2.1. Semiconducting silicides

In fact two metal silicides are considered possible candidates for light emission in silicon - $\beta FeSi_2$ and Ru_2Si_3 .

The first, $\beta FeSi_2$, which has been proposed by Schuller [Sch2003], has been already discussed in the first part of this work. It was found that $\beta FeSi_2$ precipitates exhibit strong luminescence at low temperatures which is quenched at room temperature. The strong recombination activity

and fast diffusivity [Web1983] of iron render it one of the most dreaded impurities on microelectronics, thus the applicability of $\beta FeSi_2$ in silicon photonics is highly questionable. The other silicide is Ru_2Si_3. Indeed, *ab initio* theoretical calculations [Fil1999] predicted the existence of a direct band gap, and adsorption measurements indicate the presence of such a direct band gap at about 0.9 eV [Sha1999]. However, to my knowledge no observation of Ru_2Si_3 luminescence has been reported yet.

6.2.2. Erbium emission

The rare earth erbium when ionised to a Er^{3+} state is characterised by an emission at 1.54 μm. This emission is due to a transition in the 4*f* shell of the ion between the its excited $^4I_{13/2}$ and the ground $^4I_{15/2}$ state. The 4*f* levels in the free ions are degenerate and the transition between them is forbidden. As soon as Er is introduced in a solid matrix the interaction with the neighbouring atoms partially removes the degeneracy and causes also partial mixing of the states of different parity and intrashell transitions become allowed [Oss2003]. For efficient Er^{3+} emission in silicon several important factors need to be taken into account. First of all, erbium should be incorporated in silicon at high concentration, but in its 3+ ionised donor state, without forming precipitates of the optically inactive silicide phase [Eag1991]. One should also ensure that the transitions in Er^{3+} can be excited by electron – hole pairs from the surrounding silicon. Hence, the Er^{3+} 4*f* shell and the Si electronic systems should be in contact. Finally the excited erbium should recombine radiatively. Due to its long radiative lifetime in silicon (about 2ms) [Pri1998] nonradiative processes and de-excitation can become extremely limiting. One should minimise the role of the competing nonradiative mechanisms (like Auger recombination or energy transfer to the Si electronic system).

The main limiting factor for an application of devices based on Er^{3+} doped silicon is the strong temperature quenching, which reduces the signal by three orders of magnitude on going from 77K to 300K [Cof1994]. Oxygen co-doping improves the temperature behaviour significantly, so thus the quenching within the same temperature interval is only 30 times [Pri1998].

The maximal reachable efficiency at room temperature is in the order of 0.3% [Pri1998, Fra1997].

A reduction of the de-excitation mechanisms influence and a respective enhancement of the luminescence efficiency can be reached by embedding erbium containing silicon nanocrystals in an insulating matrix. Thus, erbium doped nanocrystals incorporated in a SiO_2 matrix show nearly a 100 times enhancement of the photoluminescence when compared to samples of SiO_2 purely doped with erbium [Wat2001, Pri2001], because the excitation energy is preferentially transferred from the nanocrystals to the Er^{3+} ions.

In fact, MOS (Metal Oxide Semiconductor) devices showing efficient electroluminescence at room temperature have been demonstrated on such system [Ico2002]. The electroluminescence is mainly limited due to the difficulties of carrier injection in a semi-insulating material. However, by properly tailoring the mean radius as well as the density of the nanocrystals, it is possible to obtain an efficient carrier injection at voltages in the range of 20-30 V. Quantum efficiency of the electroluminescence about 1% at room temperature has been reported.

6.2.3. Emission enhancement due to isoelectronic traps

Localised impurity states can help to overcome the momentum conservation rule in the indirect semiconductors. If the electrons and holes are bound to a defect state, localised in real space, their quasi momentum in reciprocal space will be delocalised as a consequence of the uncertainty relation. Localised defect state in real space gives a constant energy level in reciprocal space. If the recombination is mediated by such level, no phonon assistance is necessary. An example of such process is the recombination of bound excitons (to a donor or acceptor state), where a no-phonon transition occurs.

A strategy to make the silicon luminescent is to introduce localised centres at high concentration, where excitons can be trapped. In order to maintain the Auger recombination low the localised centres should not contribute to the carrier concentration. Neutral isoelectronic centres are formed by substitution of silicon atoms with atoms or complexes of other species, but with the same valence.

Photoluminescence and, in some cases, electroluminescence has been reported from isoelectronic complexes related to sulphur, selenium [Bra1998, Bro1986], carbon [Can1987] (already mentioned in Chapter 5), and some others like oxygen (0.767 eV) and beryllium (1.076 eV) [Oss2003]. The luminescence quenches rapidly with temperature due to the strong thermal de-excitation of the traps with large radiative lifetimes (in the order of milliseconds). At 300K, only vanishingly weak luminescence is observed.

6.3. Band-to-band radiation enhancement

Green et al. [Gre2001] have demonstrated room temperature emission in bulk silicon with high efficiency in a forward biased solar cell, used as light emitter. Extremely low recombination rates are possible if one is able to reduce the competing nonradiative recombination in the bulk and at the surface to a minimum. Thus, the authors used ultra-high purity FZ material at low doping concentration to ensure minimal SRH recombination rates in the bulk. Small metal ohmic contacts on highly doped areas limited to the area of contact ensured that the recombination is restricted to the junction region.

To prevent reabsorption of emitted photons the doping level in the cell substrate was kept moderate (~$1.4x10^{16}$ cm^{-3}). Further efficiency improvement was reached by surface passivation with a thermal oxide and a surface texturing for a better optical coupling. Appling all these strategies together, an external efficiency of about 1% ws reached. Although, the device shows an ultimate external efficiency for bulk silicon, an on-chip application is not possible, because it active region includes the entire wafer depth.

An alternative approach was given by Ng et al. [Ng2001]. CZ silicon, n-type doped, was subjected to implantation of boron and an annealing step to prepare diodes. Because of this treatment, dislocation loops were introduced close to the junction in the device. The reduction of nonradiative recombination and enhancement of band-to-band, was explained by a restricted diffusion of carriers due to energy barriers, formed by the local strain field of the loops. Thus, potential pockets are formed close to the junction, which block the carrier motion and enhance the radiative decay by localizing them in defect-free regions. An internal quantum efficiency at room temperature of about 1% has been found for these light emitting devices. The electroluminescence spectrum does not present significant differences in line shape and peak position as compared to that of bulk Si.

It will be shown later that the band-to-band luminescence enhancement in samples containing dislocations, produced by means of implantation and annealing, has different origin as that pointed out in [Ng2001].

Enhanced band-to-band luminescence has been observed in (MOS) capacitors with a very thin (< 3nm) gate oxide [Liu2000, Lin2001, Che2001, Che2004]. By biasing the devices in accumulation mode a quasi 2D layer of majority carriers at the oxide / substrate interface is formed. The minority carriers are injected due to tunnelling through the oxide. The appearance of strong band-to-band luminescence has been explained by a confinement effects in the quasi 2D structure.

The external band-to-band quantum efficiency has been estimated to about 10^{-5} and the line shape and peak position are similar to those observed from bulk silicon.

The requirement of electrical pumping a priory excludes light sources and lasers based on stimulated Raman scattering in silicon [Boy2004, Ron2005].

6.4. Summary

The presented approaches illustrate the problems, which the development of silicon light emitter is facing. The main problems are related to the strong thermal quenching, to high operation voltages for electroluminescence and to the potential risk for contamination with species degrading the electric properties of the silicon. However, two approaches seem

promising for technological application. One is the enhancement of the band-to-band luminescence in presence of dislocations, and the other is the enhancement of the dislocation related radiation by engineering of their properties and structure. Both can be realized in a way compatible with the existing technology and can be excited via p-n junctions at low operation voltages. They do not involve species, which can degrade the electrical properties of silicon, and, because they are based on dislocations, they are expected to be stable upon thermal treatment. The photon energy for a light emitter based on D1 is in the range, where silicon is transparent, allowing to use other silicon based optoelectronic devices in combination with such emitter. The demonstrated quantum efficiency at room temperature (~ 1%) is also promising for application as light emitter.

In the following, these two approaches are further explored in view of their applicability for light emitting devices for on-chip interconnects.

Chapter 7

Discussion of the parameters

In this chapter, the parameters, which are used to characterise the silicon light emitting diodes, are reviewed and the method for calibration of the photoluminescence system for absolute measurements of the radiant flux is described.

Three different values are used for characterisation of the emitters: internal and external quantum efficiencies and power efficiency. The power efficiency and external quantum efficiency are experimentally accessible. However, they depend on the geometry and the construction of the emitter and are not directly related to the radiative recombination process in the semiconductor. As we are interested in the properties of the silicon as light emitting material, a more relevant parameter is the internal quantum efficiency, which is directly related to the radiative transitions in silicon. In this chapter, a relation between the external and internal efficiency is established for planar emitters, which are predominantly used in this study.

The external quantum efficiency is derived from spectrally resolved electroluminescence measurements at known current trough the emitter. The calibration procedure is described, which is necessary for calculation of the external efficiency.

7.1. Internal, external and power efficiency

The internal efficiency, η_{int}, of a light emitter is defined as a ratio of the number of generated photons, N_{ph}, per unit of time and the number of the electrons, N_{el}, injected. An ideal emitter with unity efficiency will thus produce one photon for each injected electron.

$$\eta_{\text{int}} = \frac{N_{ph}}{N_{el}}. \qquad (7.1.)$$

The internal quantum is related directly to the recombination mechanisms, but it is not accessible experimentally. One can measure the radiation, escaping the device, which is usually just a fraction of the radiation, which is generated. The external efficiency, η_{ext}, is then defined as the number of photons escaped the light emitter, $N_{e\,ph}$, over the injected electrons:

$$\eta_{ext} = \frac{N_{e\,ph}}{N_{el}}. \qquad (7.\ 2.)$$

The power efficiency, η_{pow}, of a light emitter relates the optical power of the emitted radiation to the electrical power, which is necessary to produce it:

$$\eta_{pow} = \frac{P}{U\,I}, \qquad (7.\ 3.)$$

where U, I, and P stands for the voltage and current through and the measured radiant flux, respectively.

7.2. Light escape cone, Lambertian emission pattern, extraction coefficient

The light generated in the semiconductor suffers partial internal reflection from the surface. The angle of total internal reflection defines the light escape cone (Fig. 7.1). The light emitted into the cone can escape from the semiconductor, whereas the light emitted at larger angles is subject to total internal reflection. For silicon the refractive index for the band gap radiation is 3.6 and this corresponds to an angle of the escape cone, θ_c=16°.

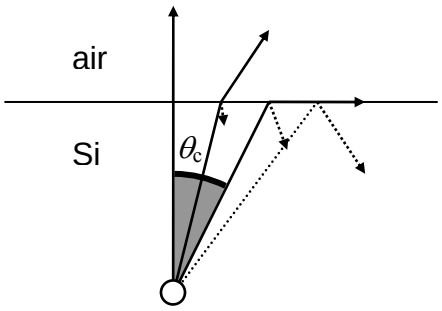

Figure 7.1. Escape cone of the radiation generated in the semiconductor. Due to total internal reflection only light emitted in the escape cone defined by θ_c can be detected.

From a planar source, the light is emitted in a Lambertian pattern, (Figure 7.2). For a quantitative estimate, it assumed that the light reaches the surface from a source of unity intensity inside the silicon substrate. The light from the source is emitted uniformly in all directions and its wavelength is that of the silicon bang gap radiation (1.127 μm).

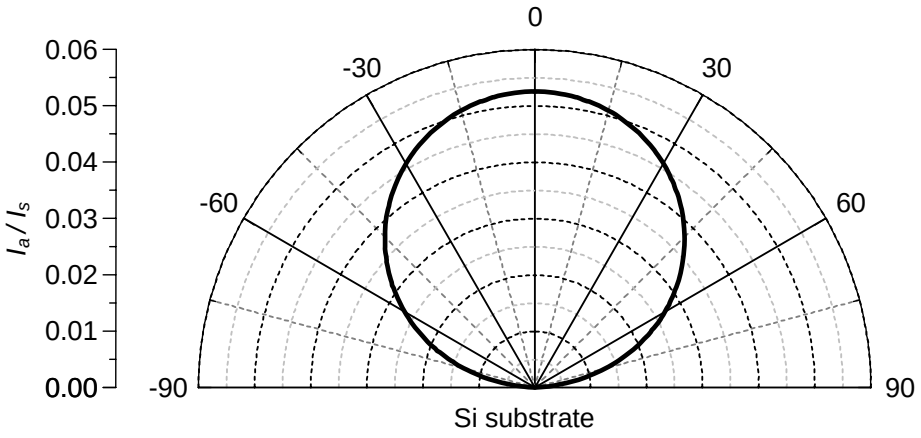

Figure 7.2. Angular distribution calculated for silicon band-to-band radiation for a planar emitter with unity intensity. The curve presents a Lambertian pattern.

The radiant flux (power), P_{Source}, emitted from the source is isotropic distributed in a solid angle 4π inside silicon, with radiant intensity, I_S,

$$I_S = P_{source}/4\pi. \qquad (7.\ 4.)$$

The radiant flux within the escape cone, defined by θ_c (solid angle $2\pi(1-\cos\theta_c)$) is then: $P_{Source}\,(1-\cos\theta_c)/2$. Due to the partial reflection, only a part, T, of the light is transmitted. As θ_c is a small angle, one can use the Fresnel's formula for normal incidence:

$$T = \frac{4n_a n_S}{(n_S + n_a)^2} \qquad (7.\ 5.)$$

The radiant flux in the air P_{air} is then:

$$P_{air} = P_{source}\frac{2n_s n_a(1-\cos\theta_c)}{(n_s+n_a)^2} \approx P_{source}\left(\frac{n_a}{n_S}\right)^2 \frac{n_s n_a}{(n_s+n_a)^2} \qquad (7.\ 6.)$$

A more precise calculation requires accounting for the dependence of the radiant intensity in air on the angle of incidence, α, and the angle of refraction, β. It is accounted by involving angular dependencies of the transmission coefficient, $T(\alpha(\beta), \beta)$ and the solid angle of vision (Figure 7.3).

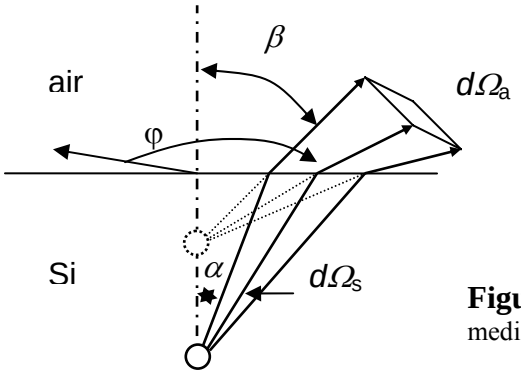

Figure 7.3. Change of the angle of vision is in the second media due to refraction

The radiant flux element of light in a solid angle element in air, $d\Omega_a$ ($d\Omega_a = \sin\beta\, d\varphi\, d\beta$), equals that in the substrate solid angle element, $d\Omega_s$ ($d\Omega_s = \sin\alpha\, d\varphi\, d\alpha$), accounting for the transmission coefficient through the interface:

$$I_a\, d\Omega_a = T\; I_S\, d\Omega_S\,, \qquad (7.\ 7.)$$

where I_a and I_S stand for radiant intensity in air and silicon, respectively.

The angular dependence of the transmission coefficient is given by the Fresnel's formulas for non-polarised emission:

$$T = \frac{1}{2}(T_{\parallel} + T_{\perp})\,, \text{ where } T_{\perp} = 1 - \left[\frac{\sin(\alpha-\beta)}{\sin(\alpha+\beta)}\right]^2 \text{ and } T_{\parallel} = 1 - \left[\frac{\tan(\alpha-\beta)}{\tan(\alpha+\beta)}\right]^2, \qquad (7.\ 8.)$$

where $T_{\parallel}$ and $T_{\perp}$ denote the transmission coefficient for light polarised parallel and perpendicular to the plane of incidence.

Appling Snell's law it can be easily seen, that radiant intensities are related by the following equation:

$$I_a = I_S \left(\frac{n_a}{n_S}\right)^2 T(\alpha(\beta),\beta)\frac{\cos\beta}{\cos\alpha}$$

The extracted radiant flux, P_{Air}, is then obtained by integration of I_a over the entire hemisphere above the device

$$P_{Air} = \int_{\beta=0}^{\frac{\pi}{2}} \int_{\varphi=0}^{2\pi} \frac{P_{Source}}{4\pi}\left(\frac{n_a}{n_S}\right)^2 T(\alpha(\beta),\beta)\frac{\cos\beta}{\cos\alpha(\beta)}\sin\beta\; d\beta\, d\varphi\,. \qquad (7.\ 9.)$$

However, the result from a numerical integration of Eq. (7.9) and calculation with approximated formula Eq. (7.6) coincide within 6%.

The ratio between the radiant flux, P_{Air}, escaping the device and the radiant flux from the source P_{Source} represents the relation between the external and internal efficiencies.

Thus the relation between external and internal power efficiencies in silicon is given by:

$$\eta_{\text{int}} = \frac{\eta_{ext}}{0.013}\,. \qquad (7.\ 10.)$$

The same relation holds for the quantum efficiencies too, as the photon energy is not changed by the refraction at the surface. The ratio between the internal and external efficiencies represents the coefficient of extraction for the radiation generated in the planar emitter.

Calculation were made by accounting for the contribution of an oxide layer at the surface to the transmission coefficient, T. It was found that if the oxide thickness is below 20 nm it does not influence the coefficient of extraction.

Although this calculation is made for a refractive index, corresponding to a wavelength 1.127 μm (band-to-band emission) it can also be used to estimate the efficiency in the sub band gap range (down to 1.5 μm), because the refractive index there just slightly decreases and this is the only parameter which influences the coefficient of extraction.

7.3. Calibration for absolute measurements of the radiant flux

For the measurement of the quantum efficiency, the photoluminescence setup is calibrated with a source with known spectral radiance (Oriel 6580). The sample is replaced by an aperture illuminated by the calibrated source (Figure 7.2a). The resulting radiant flux into the detection system is then determined by the irradiance from the calibrated source and the aperture area. The multiplication factor curve, used for correction of the directly measured spectra (Fig 3.3b in Chapter 3) is calibrated (Figure 7.3), so that the spectra after correction with that multiplication factor represent the absolute spectral power density of the radiation. The power of the radiation in a defined spectral range is then given by the area of the corrected spectrum under the curve.

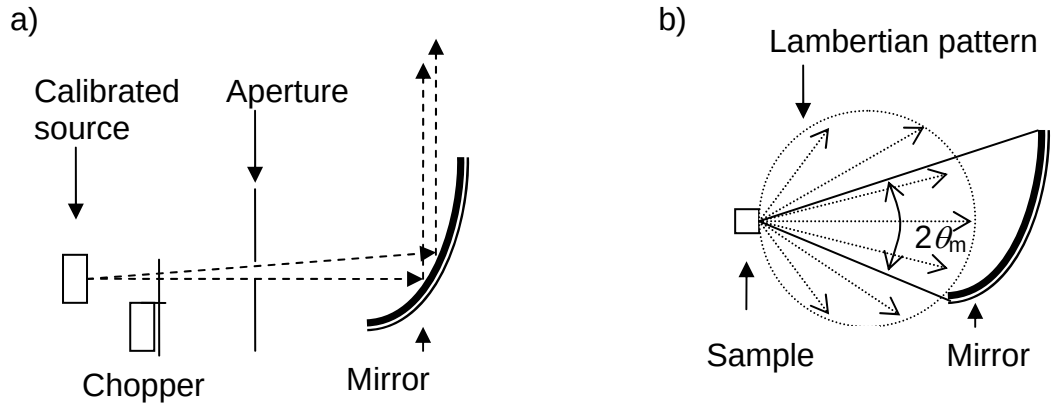

Figure 7.2. Setup for calibration and radiometric measurements. a) Illumination of the detection system with a defined radiant flux from the calibrated source. b) The total flux is higher than the measured one, because not all of the radiation is detected, requiring a correction accounting for the viewing angle of the mirror from the position of the sample.

The absolute measurements of the total radiant flux are carried out by measuring the radiant flux, which is emitted into the solid angle formed by the sample and the collecting parabolic mirror. To obtain the total radiant flux from the sample, the measured flux is multiplied by a factor, F, accounting for the Lambertian distribution of the radiation.

$$F = \frac{1}{\sin^2 \theta_m}, \qquad (7.\ 11.)$$

where $2\theta_m$ is the angle formed between the mirror diameter and the sample (Figure 7.2b).

The experimental error of the absolute measurements is estimated to about 30% by reproducing the measurements of one and same source after independent calibrations and readjustment.

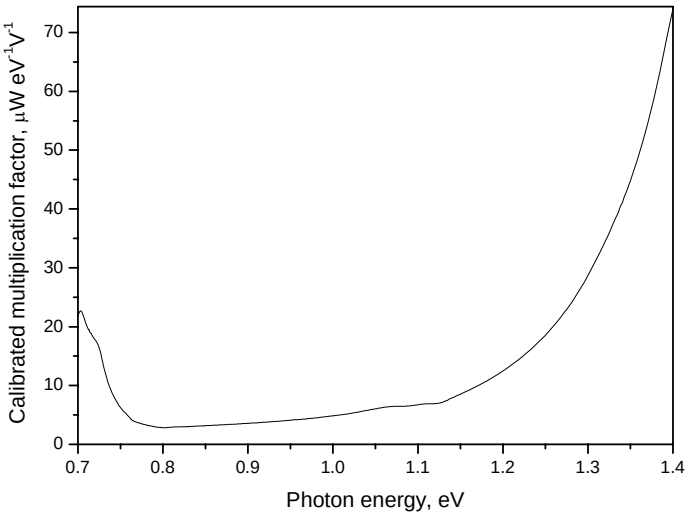

Figure 7.3 Calibrated multiplication factor for the system response. It gives the spectral power density (µW/eV) for a 1V electric signal on the detector.

The calibration was cross correlated by measurement of a commercial IR emitter with known radiant flux, emitting at 900 nm, at which the germanium detector used is still sensitive. The flux, determined by the spectral luminescence measurement was found to agree with the specified power of the source within the experimental error.

7.4. Summary

The calibration of the device for absolute measurements allows to estimate the internal quantum efficiency of the band-to-band luminescence from planar emitters based on their spectra. The quantum efficiency at different emission energies in the sub-band gap energy range of the silicon emission can be estimated from the peak areas in the sensitivity-corrected spectra. The lock-in technique, which is used for detection is strongly source selective and thus an influence by the thermal emission on the spectroscopic measurements, used for estimation efficiency, is excluded.

Chapter 8

Band-to-band light emitters prepared by implantation and annealing

In this chapter, the results of controllable dislocation formation by implantation and annealing are present. The observed enhancement of the band-to-band luminescence is analysed in view of competitive recombination mechanisms in silicon and optimal injection level. The role of dislocations and dopants for the enhancement of the band-to-band radiation is discussed.

The pioneering work of Ng et al. [Ng2001] triggered an intense research activity for finding the origin of the enhanced electroluminescence, which is observed from silicon samples subjected to implantation of boron with subsequent annealing. Additionally, their devices exhibit the interesting feature of increasing the efficiency with temperature.

The explanation of the luminescence enhancement in presence of extended defects, given originally in [Ng2001] and [Lou2004] is illustrated in Figure 8.1. After the implantation, a subsequent annealing step is necessary to electrically activate the boron dopants. Upon annealing, interstitial silicon atoms are generated and aggregate, forming an extrinsic stacking fault bordered by an edge dislocation loop (Figure 8.1a). At the edge, the lattice, just outside the loop is placed under negative hydrostatic pressure and just inside it is placed under positive hydrostatic pressure (Figure 8.1b). According to the estimations in [Lou2004] the maximal stress around the dislocation reaches 25-50 GPa. Due to the increase of the silicon band gap upon decreasing the pressure a modification of the band gap occurs, so the boundary of the dislocation loop represents a barrier of several hundred meV.

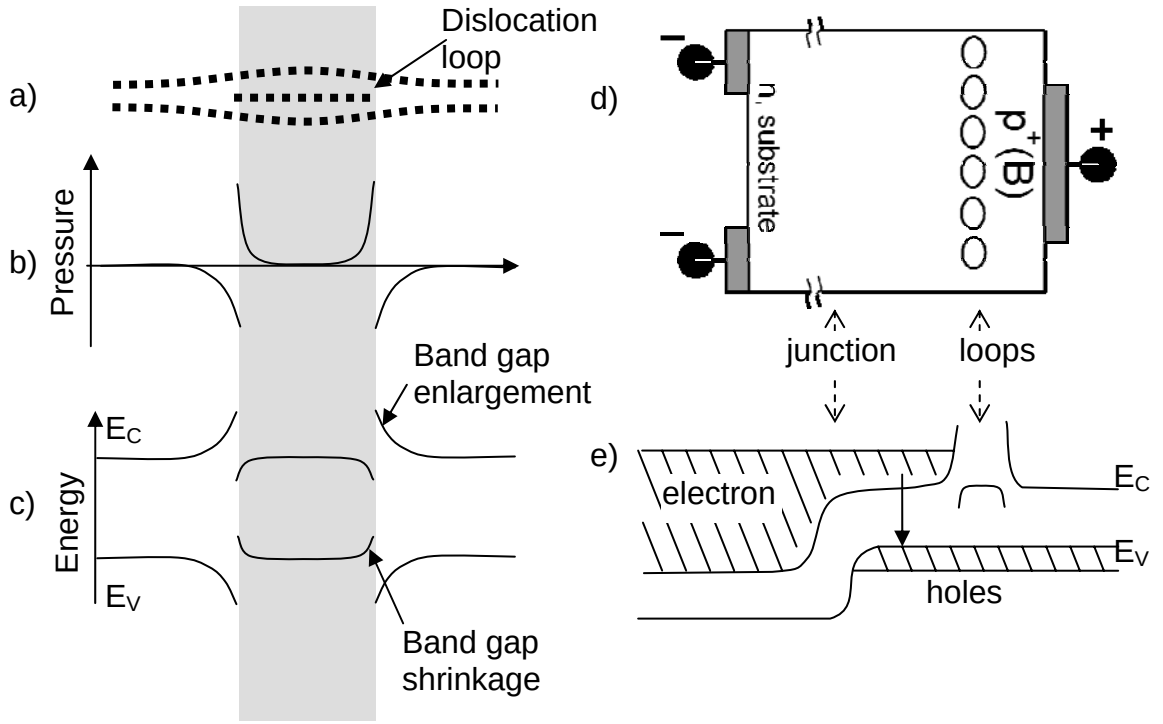

Figure 8.1. Dislocation loops in a light emitting diode prepared by implantation of boron. a) loop inserted in the Si lattice b) stress distribution across the loop c) band gap modification due to the induced stress d) position of the loops in the device e) device operating in forward bias. The potential barrier is due to an array of dislocation loops, parallel to the depletion region edge. (Schematic representation [Ng2001, Lou2004])

The key to the operation of the device (Figures 8.1d and e) is the utilization of the potential barrier at the dislocation loops to modify the injected carrier flow, by preventing carrier diffusion into the bulk of the device (Figure 8.1e). This explanation implies, that the strong band-to-band luminescence is generated in a small region of the sample where the injected carriers are confined by the strain field.

Further works of other authors have confirmed the effect of band-to-band luminescence enhancement, but giving different explanations of the effect.

Pan et al. [Pan2004] connected the luminescence enhancement to a specific type of extended defects (rodlike defects), which have been observed by transmission electron microscope (TEM) imaging in samples with significantly enhanced luminescence after implantation and annealing.

Sun et al. [Sun2003, Sun2004] attributed the luminescence enhancement to the formation of bound excitons at boron precipitates and boron doping spikes, formed by the processing. It has been suggested that the bound excitons are stable at room temperature and behave as a reservoir for minority carriers. Accordingly, the luminescence enhancement is caused by recombination of free excitons supplied from the bound excitons.

Sobolev et al. [Sob2003, Sob2004] pointed out that there is, probably, an indirect influence of the extended defects formed after the implantation and annealing. They studied samples with dislocation loops annealed at different temperatures and found that the maximal efficiency occurs on those samples, in which the defects formed due to implantation were annealed completely. The authors raised a hypothesis that the influence of defects/dislocations on the efficiency of the luminescence may be due to their gettering ability and not to confinement effects in the recombination process.

Obviously, the effect of extended defects in silicon on the luminescence enhancement needs further investigation. The model of confinement-induced enhancement given by Ng. et al. [Ng2001] leaves unclear points. For instance, the dislocation loops form a one-dimensional barrier for the three dimensional current flow. It is unclear why the carriers become confined due to the barrier at the edge of the dislocation loop and do not recombine in the inner part of the loops, where the band gap shrinkage causes an energetically more favourable (Figure 8.1.a) state.

Standard silicon is considered not suited for a light emitter, as the probability of phonon-assisted band-to-band luminescence is very low. Competitive nonradiative recombination rates are much higher and most of the excited electron-hole pairs recombine nonradiatively. However, optimal conditions can be found, where radiative transitions present a significant part in the recombination. The radiative efficiency in silicon can be estimated, considering classical recombination processes and the enhancement of the luminescence can be understood in view of the following model.

8.1. Model describing the efficiency

The recombination in silicon is due to mainly three components, each associated with a distinct mechanism, namely multiphonon SRH recombination via deep levels in the band-gap, Auger recombination with the energy given to a third carrier, and the radiative recombination [Kit2004]. The recombination rates of these mechanisms depend on the excess carrier concentration Δn in the following manner.

The SRH recombination rate, R_{SRH}, depend linearly on Δn, determined by the SRH lifetime, τ_{SRH} (Chapter 1):

$$R_{SRH} = \frac{\Delta n}{\tau_{SRH}}. \qquad (8.1)$$

The rate of radiative recombination gains importance in the high injection regime and therefore one, can consider the term including ‘bimolecular’ recombination to be characteristic for the radiative recombination rate:

$$R_{BB} = B\Delta n^2 . \tag{8.2}$$

The Auger recombination rate is determined by the third power of Δn, taking into account that at high excitation, the hole concentration is almost equal to the electron concentration:

$$R_{Auger} = C\Delta n^3 . \tag{8.3}$$

The internal quantum efficiency is obtained by the ratio of the radiative recombination rate R_{BB} and the overall recombiantion rate, i.e:

$$\eta_{\text{int}} = \frac{R_{BB}}{R_{\text{SHR}} + R_{BB} + R_{Auger}} . \tag{8.4}$$

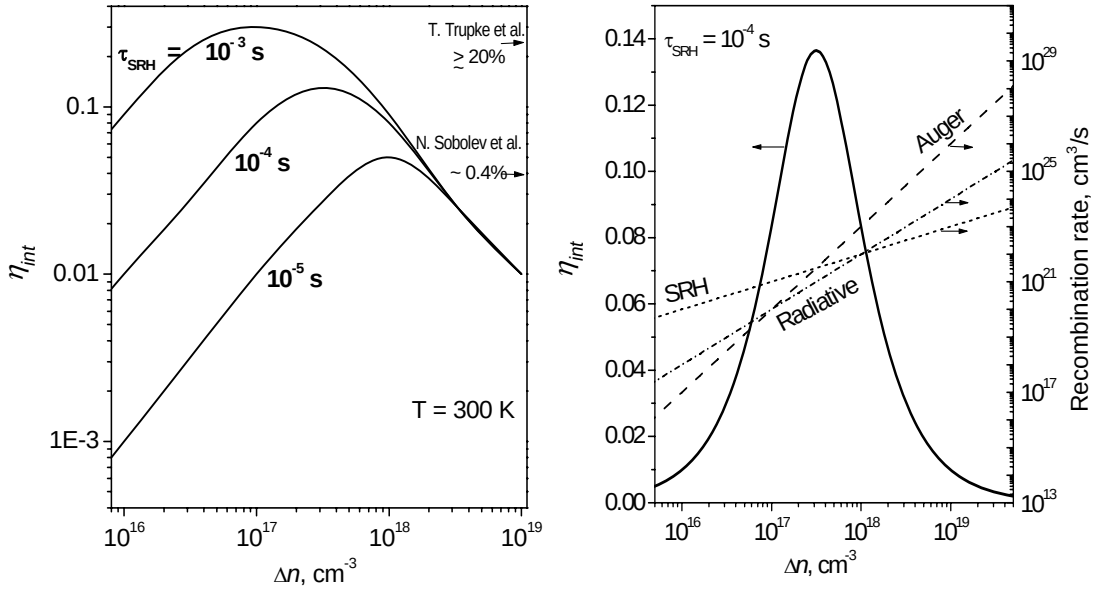

Figure 8.2. Internal quantum efficiency dependence on excess carrier concentration at room temperature.
a) Internal quantum efficiency is calculated using relation (8.4) with the SRH lifetime as parameter. Experimental quantum efficiencies reported by Trupke et al. [Tru2003a] and Sobolev et al.[Sob2004] are given for comparison.
b) Contribution of the three major recombination mechanisms. Maximal efficiency is obtained when SRH and Auger recombination are equally weak.

Figure 8.2a shows the internal quantum efficiency η_{int} as function of the excess charge carrier density Δn, using the data in Chapter 1. At room temperature, for the coefficient B a value 10^{-14} cm^3s^{-1} is taken and for Auger recombination coefficient a value for C of 10^{-31} cm^6s^{-1}. At low injections, the dominant recombination is SRH (branch with positive slope) and at high injection, the Auger processes are dominant (branch with negative slope). Optimal conditions for maximal band-to-band efficiency occur when both processes are equally weak (Figure 8.2b).

In nearly perfect Si material with τ_{SRH} = 10^{-3} s, the contribution of the radiative recombination to the overall recombination can be significant, so that the maximum of the internal quantum efficiency is expected about 30 %. This value is in agreement with the findings in [Tru2003a], where an internal quantum efficiency for Si at room temperature exceeding 20 % was estimated.

The model considers only the bulk recombination and does not account for confinement effects, which eventually can appear due to the presence of the dislocation loops. It shows that high efficiency of the luminescence is achievable even without such effects. Only high SRH lifetimes and sufficiently high injection concentrations are necessary to obtain internal efficiencies in the order of several percent.

The central question, which needs to be answered, is about the role of dislocation loops and the boron implantation for the band-to-band luminescence enhancement. In order to study this in detail a series of samples with different implantation and annealing conditions were prepared and the electroluminescence efficiency measured. The results from the measurements are analysed in view of the classical recombination scheme presented above.

8.2. Sample preparation

Silicon epilayers of a few micrometer thickness are grown by chemical vapour deposition on top of (100)-oriented 8 inch CZ silicon wafers. The resistivity of the substrates and of the epilayers was about 10 Ωcm and the conductivity was either n- or p-type. Implantation was done across a 15 nm thick scattering oxide. Boron was implanted into the n-type material at different energies ranging from 50 to 250 keV and doses from 2 x 10^{12} to 2 x 10^{14} cm^{-2}, while phosphorus was implanted into the p-type material at energies between 135 and 500 keV and doses in the range from 4 x 10^{12} to 4 x 10^{14} cm^{-2}. After implantation, the samples were heat treated in a furnace (1000°C, 20 min, nitrogen atmosphere) or by rapid thermal annealing (1040°C, 10 s, nitrogen atmosphere), respectively. Finally, the wafers were annealed at 400°C for 30 min in hydrogen atmosphere. A list of the samples prepared for this study is given in Table 8.1. The implantation and annealing of boron and phosphorous in p- and n- type wafers results in p-n junctions close to the surface. It will be shown later, that after the annealing step crystal defects, predominantly at the depth of the maximum dopant concentration are formed. The defect density is found to be higher for larger implantation doses.

Sample #	Sub-strate	EPI, type	Scattering Oxide Thickness, nm	Implan-tation type	Dose, cm^{-2}	Ion energy, keV	Anneal
S1	p-Si	B	14.5	P	4E12	500	RTA
S2	p-Si	B	14.5	P	4E13	500	RTA
S3	p-Si	B	14.5	P	4E14	500	RTA
S4	p-Si	B	14.5	P	4E12	500	Furnace
S5	p-Si	B	14.5	P	4E13	500	Furnace
S6	p-Si	B	14.5	P	4E14	500	Furnace
S7	p-Si	B	10	P	4E12	135	RTA
S8	p-Si	B	10	P	4E13	135	RTA
S9	p-Si	B	10	P	4E14	135	RTA
S10	p-Si	B	10	P	4E12	135	Furnace
S11	p-Si	B	10	P	4E13	135	Furnace
S12	p-Si	B	10	P	4E14	135	Furnace
S13	n-Si	P	14.5	B	2E12	240	RTA
S14	n-Si	P	14.5	B	2E13	240	RTA
S15	n-Si	P	14.5	B	2E14	240	RTA
S16	n-Si	P	14.5	B	2E12	240	Furnace
S17	n-Si	P	14.5	B	2E13	240	Furnace
S18	n-Si	P	14.5	B	2E14	240	Furnace
S19	n-Si	P	10	B	2E12	50	RTA
S20	n-Si	P	10	B	2E13	50	RTA
S21	n-Si	P	10	B	2E14	50	RTA
S22	n-Si	P	10	B	2E12	50	Furnace
S23	n-Si	P	10	B	2E13	50	Furnace
S24	n-Si	P	10	B	2E14	50	Furnace

Table 8.1. List of the samples prepared for investigation of the electroluminescence.

8.3. Formation of extended defects

The density of the defects depends on the treatment. After implantation and annealing, dislocation loops with different density are observed. Figure 8.3 shows cross sectional TEM images from samples implanted with phosphorous at an energy of 135 keV. Predominantly, prismatic dislocation loops are formed with sizes in the range 20 – 100 nm and density varying from 0 to ~ $5x10^{10}$ cm^{-2}, depending on the implantation dose and on the type of annealing. Furnace annealing leads to a lower defect density as compared to RTA and the lower the initial implantation dose the lower the final density of the dislocation loops in the samples.

Electroluminescence investigation on samples prepared from the wafers is carried out in order to find the effect of the loop density on the luminescence enhancement.

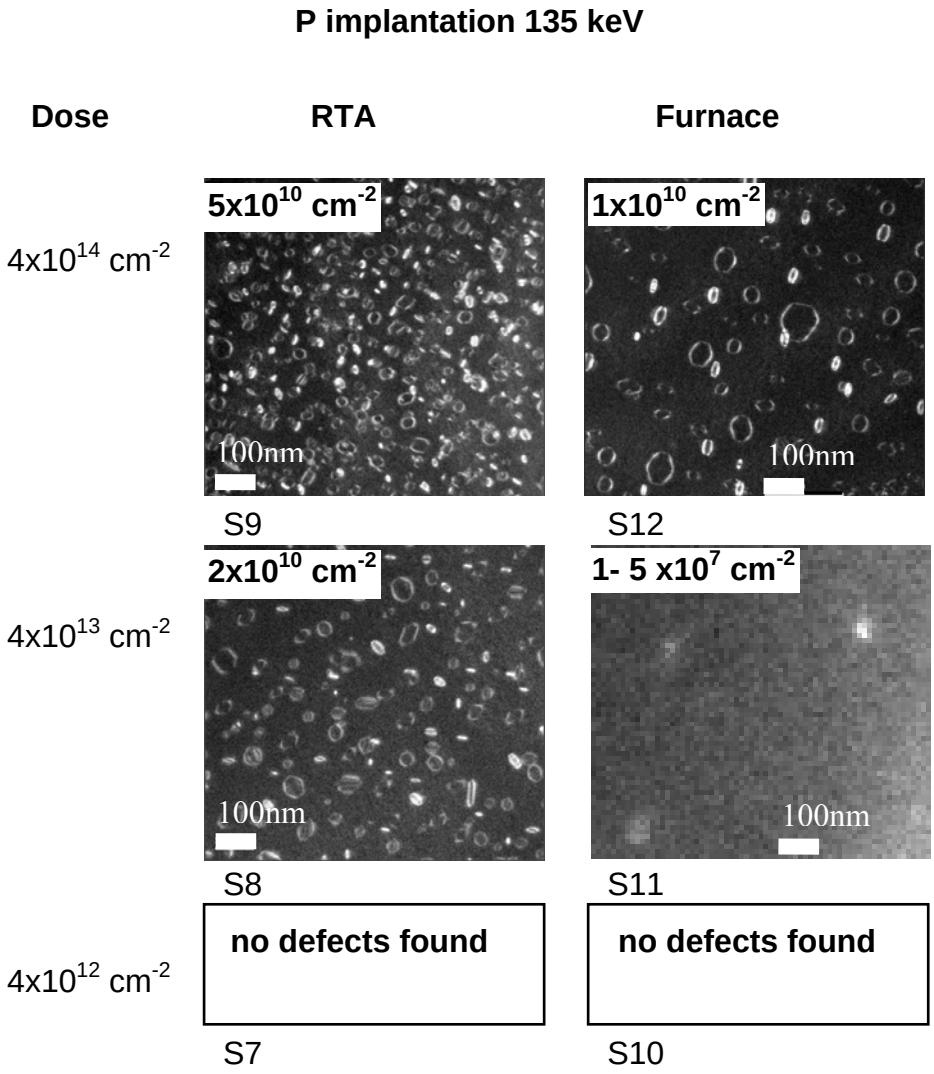

Figure 8.3. Extended defects, revealed by TEM on samples prepared by implantation of phosphorous in a boron doped substrate. The implantation energy was 135 keV. The dose and the estimated defect density are noted in the figures. The images reveal presence of perfect prismatic and faulted Frank loops.

As it is discussed in the following paragraph, if the dislocation loops were directly involved in the radiative recombination process, one would expect the sample with the maximal dislocation loop density to show also maximal efficiency of the electroluminescence. In the samples with higher density of the loops, the barrier, which the carriers are exposed to, would be spatially denser. Thus the effect of restricting the carrier motion would be stronger. However, the measurements of electroluminescence efficiency show a different picture.

8.4. Correlation of the room temperature electroluminescence with the extended defects concentration

The electroluminescence measurements are carried out on 4x4 mm pieces cleaved from the wafers. Prior to contacting, they are treated in hydrofluoric acid to remove the oxide layer.

Two aluminium contacts are deposited on the front side of each diode by evaporation through a mask, leaving a 0.8 mm wide slit between the contacts. The backside contact is prepared by rubbing of InGa alloy. The electroluminescence is measured through the slit between the contacts on the front side, observing 2 mm of the slit length. The diodes are forward biased so that the current density during the measurement is 0.8 Acm^{-2}. It is assumed that the current is distributed uniformly in the plane of the diode due to the highly doped region in the diode emitter. The luminescence is generated in the entire diode area, but only the part, which is generated beneath the slit contributes to the measured signal. An important observation which should be noted is that the effect of enhanced electroluminescence is found for both boron as well as for phosphorous implantation.

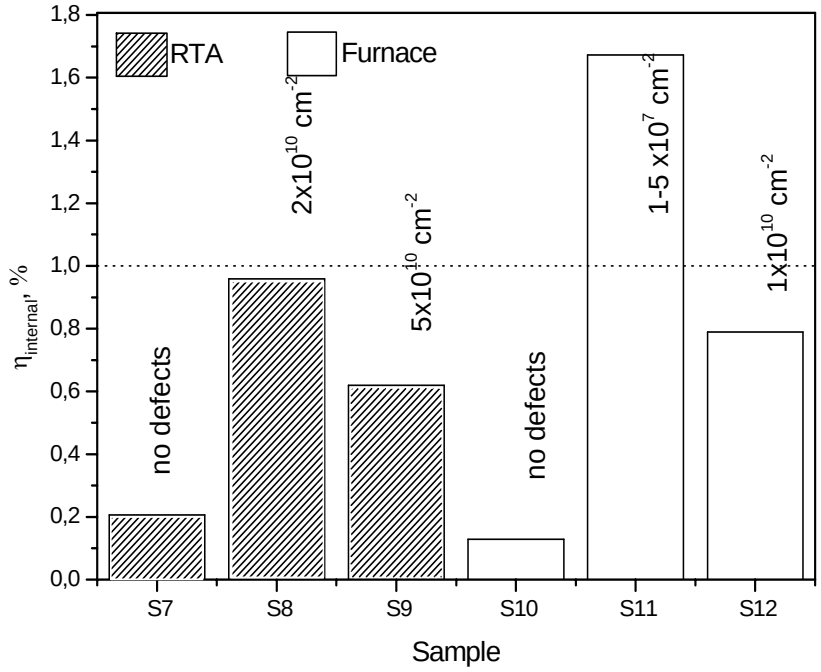

Figure 8.4. Internal efficiency of phosphorous implanted samples at energy 135 keV after furnace and RTA annealing. The loop density found by the TEM imaging is indicated above the columns.

Figure 8.4 shows the room temperature efficiency of the electroluminescence of the samples, whose images are present in Figure 8.3. The samples are measured at identical conditions.

According to the model of carrier localisation at the dislocation sites [Ng2001] the luminescence efficiency should be larger, when the dislocation loop density is higher. However, the experimental observations in Figure 8.4 deviate from this picture. It appears that there is an optimal concentration of extended defects, giving a maximal luminescence, which depends on the annealing procedure and the implantation dose. Thus the RTA treated sample, with dislocation loop density of $2x10^{10}$ cm^{-2} shows an efficiency of only 0.9 %, while the furnace annealed one, with only $5x10^{7}$ cm^{-2} dislocation loop density shows the maximal

efficiency of about 1.6%. The samples where no defects were found by the TEM imaging exhibit an efficiency of about 0.2% which a factor of two lower than that observed by Sobolev et al. [Sob2004] for a similar sample preparation.

It is seen that the quantum efficiency is not related directly to the density of the loops in the implanted layer. However, it appears related to the annealing procedure and the implantation dose, i.e. to parameters, which influence the electrical properties of the diodes and the gettering properties of the dislocations.

8.5. Correlation of the luminescence efficiency with annealing and implantation parameters

Figure 8.5 shows the internal quantum efficiency for different boron implanted p^+-n light emitting diodes. A clear influence of the implantation and the annealing conditions can be seen. Furnace annealing always causes a higher efficiency than RTA for identical implantation conditions. The highest efficiency in our boron-implanted samples - close to 1 % - appears for 50 keV, i.e. for the smallest implantation energy, and at the highest implantation dose of 2 x 10^{14} cm^{-2}. This trend, i.e. increase of efficiency with decreasing energy and increasing dose, is in agreement with data reported in [Ng2001], where an efficiency of about 1.6 % was measured at room temperature for boron implantation at 30 keV and a dose 1 x 10^{15} cm^{-2}.

A similar influence of the annealing type was observed for phosphorous implanted samples. Figure 8.6 shows the internal quantum efficiencies of electroluminescence at room temperature for four phosphorus implanted n^+-p diodes. Again, furnace annealing yields a higher efficiency than RTA and a reduction of implantation energy and an increase of implantation dose result in an increase of efficiency.

Higher implantation doses and lower implantation energies are favourable for formation of regions with high defect density during the implantation. During the annealing, the crystal is recovered to a different extend, depending on the procedure parameters. We observe, that the effect of enhanced luminescence is more pronounced on better-recovered crystals with lower dislocation loop densities. Increase of SRH lifetime (Paragraph 8.1) could explain our observation. Such increase could be caused due to gettering of impurities at the dislocations or due to gettering induced by the dopants (Chapter 4). Longer thermal treatment (furnace anneal) favours the gettering, leading to a more pronounced enhancement of the band-to-band efficiency.

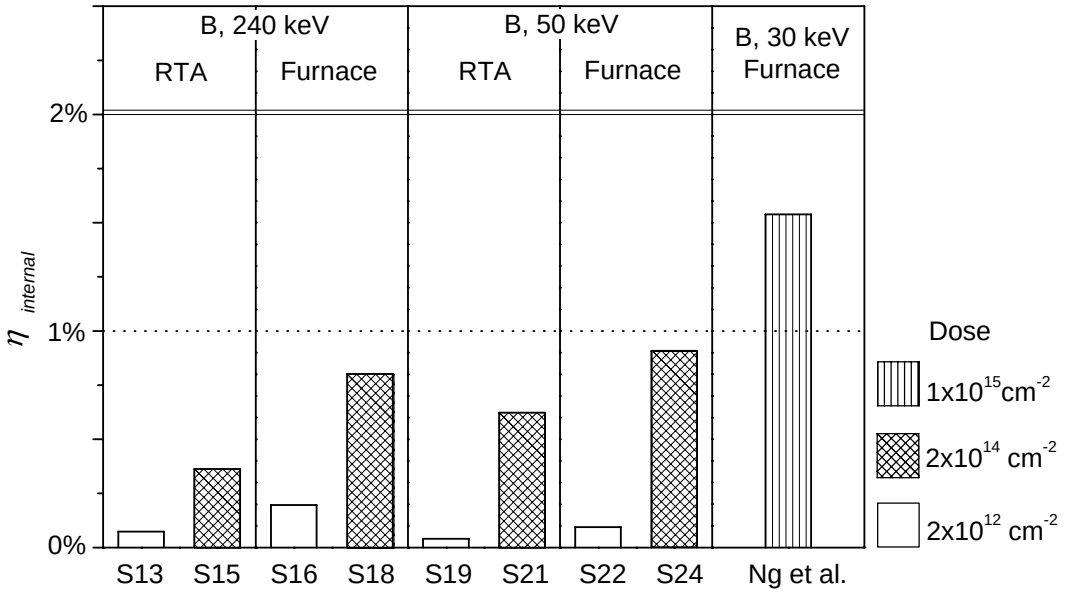

Figure 8.5. Internal quantum efficiency (T = 300 K) of the band-to-band electroluminescence for boron implanted p^+-n diodes for different implantation and annealing conditions. The efficiency is larger for small implantation energies and increases with the implantation dose. For comparison, experimental data reported by Ng et al. [Ng2001] are given, too. Unfortunately, an exact comparison with the [Ng2001] is not possible, because the exactly same conditions could not be met for technical reasons.

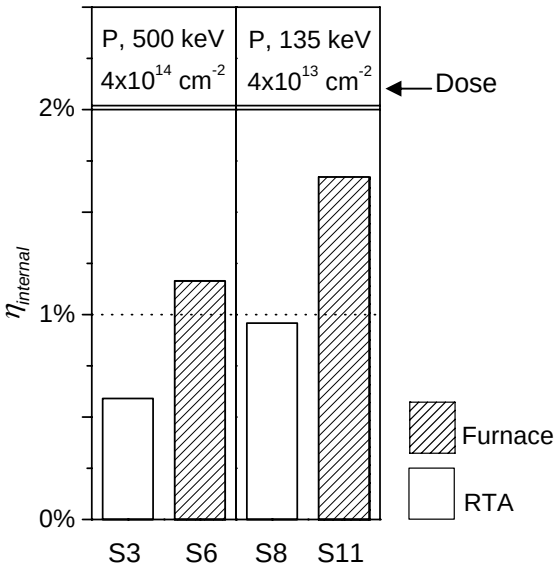

Figure 8.6. Internal quantum efficiency of the band-to-band electroluminescence for different implantation and annealing conditions of phosphorus implanted n^+-p diodes at T = 300 K. The furnace annealing and low implantation energy yield the best results.

8.6. Anomalous temperature dependence of the luminescence

It has been found that the electro- and photo- luminescence of the diodes prepared by implantation and annealing show anomalous temperature dependence, namely the internal efficiency of band-to band luminescence and, consequently, its intensity increases with temperature [Ng2001] (Chapter 4). Similar anomalous behaviour is also detected on our samples. Figure 8.7 shows the temperature dependence of the electroluminescence internal efficiency of the phosphorous implanted sample S11, exhibiting maximal room temperature efficiency from the entire series. Although there are extended defects present in the sample (as detected by TEM imaging), dislocation-related radiation is not observed (Figure 8.7. inset) in the temperature range 80 – 300 K. Dislocation-related radiation, namely the D4 line, is observed from the sample S12, where the density of the defects is three orders of magnitude higher (Figure 8.8, inset) than in S11. The well established anomalous temperature behaviour (Figures 8.7 and 8.8) observed in these two cases is characteristic for all samples. However, there are significant differences between the magnitudes of the efficiency change upon increasing the temperature. For sample S11, the efficiency increases about 3 times upon change in the temperature from 80 to 300K, while for sample S12 the change in the same temperature range is more than 30 times. The efficiency in sample S11 is mostly changed by the variation of the band-to-band peak *width* with temperature, while for S12 both, the peak *amplitude* and its *width* are strongly influenced. That is reflected in the different temperature dependences. For S11 nearly linear dependence is observed, while for S12 the dependence is nearly quadratic. The magnitude at which the efficiency changes with temperature can be related to concentration of the extended defects present in the sample and to the doping concentration in the emitter (determined by the implantation dose).

In the following we try to evaluate the role of the dislocation loops. The presence of the characteristic dislocation line D4 in the low temperature spectrum of S12 is a clear indication that dislocations are involved in the recombination process. The anomalous temperature behaviour is much more pronounced in the sample where dislocation loops at high concentration are present. As it has been previously in this work (Chapter 4), the anomalous temperature behaviour can be caused due to recombination on the shallow dislocation bands and/or dopant levels. Thus, the sample with a high dislocation concentration and high emitter doping is expected to show a more pronounced anomalous temperature behaviour. And, indeed, such behaviour is observed on our samples.

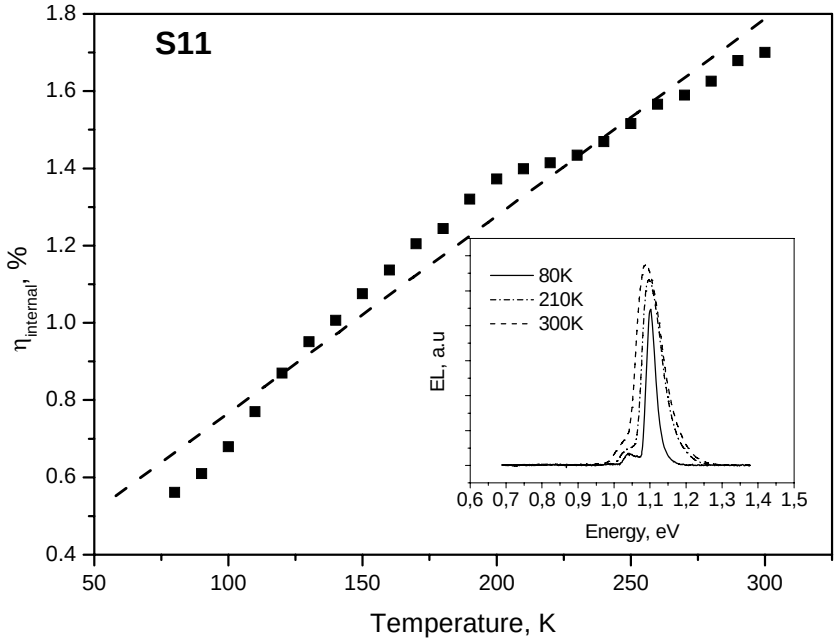

Figure 8.7. Temperature dependence of the internal efficiency of electroluminescence measured on n^+-p diode S11. The dotted line is linear dependence on T and is guide for the eye. The inset shows the EL spectra at 300 K, 210K and 80 K, respectively. Only a band-to-band peak and its phonon replica of is observed.

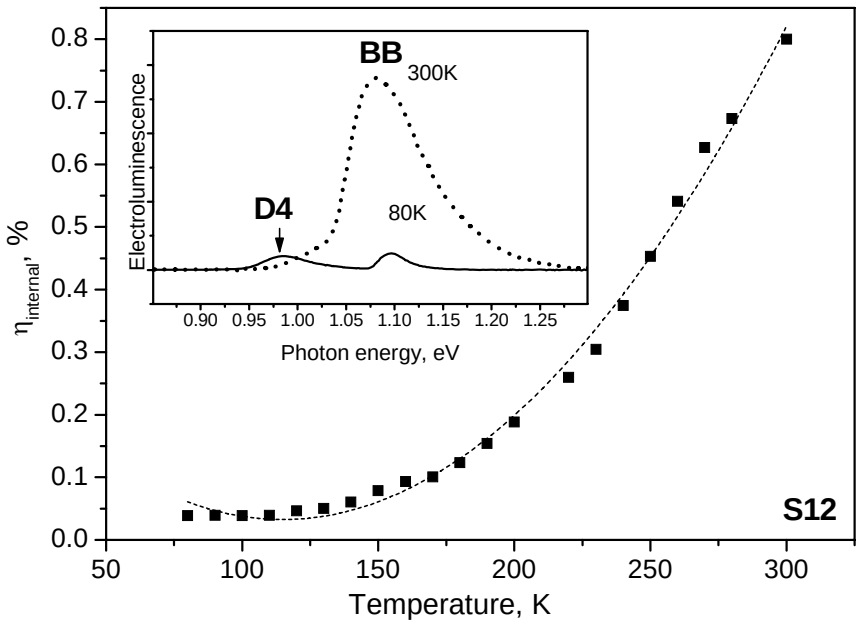

Figure 8.8. Temperature dependence of the integrated intensity of the band-to-band electroluminescence of S12 n+-p diode. The dotted line is quadratic dependence on T and is guide for the eye. The inset shows the EL spectra at 300 K and 80 K, respectively.

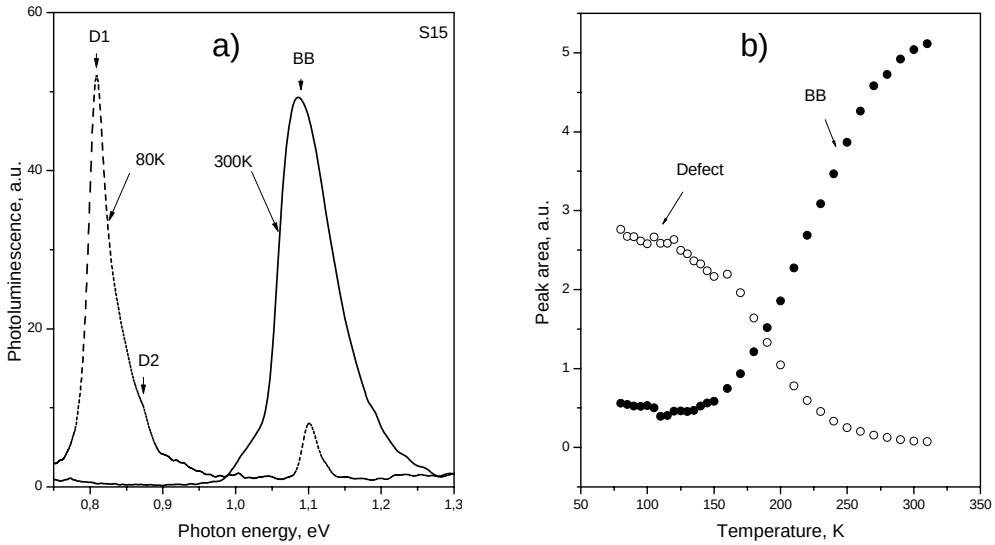

Figure 8.9. Photoluminescence temperature dependence. a) Strong dislocation-related luminescence is observed in the low temperature spectrum of sample S15. D1 and D2 dislocation features can be distinguished. b) Upon increasing the temperature the dislocation-related radiation decreases and band-to-band radiation becomes stronger.

Strong anomalous temperature behaviour is observed not only in the case of electroluminescence, but also in the case of photoluminescence. The presence of recombination-active dislocations is clearly seen in the spectra taken on boron implanted, RTA annealed sample S15 (Figure 8.9a) where, at low temperature, D1 and D2 features are observed. The thermal quenching of the dislocation radiation is accompanied by a strong anomalous increase of the band-to-band radiation (Figure 8.9b). The recombination at the dislocations appears to be the limiting mechanism, which determines the band-to-band radiative recombination in that case. The decrease of the competitive recombination rate at the defects leads to an increase of the band-to-band radiative recombination rate.

Recombination on shallow dopant (or dislocation-related) levels as a possible origin for the anomalous temperature behaviour of band-to-band luminescence has been considered previously (See Chapter 4). The recombination process is dominated by the SRH recombination when the excess carrier density is less than 10^{17} cm^{-3}. Consequently, the temperature behaviour of the internal quantum efficiency is strongly affected by the temperature behaviour of the SRH-lifetime, τ_{SRH}(T). As the Auger recombination is almost independent on the temperature (Chapter 1), an increase of internal efficiency will appear if τ_{SRH} increases with temperature (See Figure 8.2). Indeed, according to the SRH statistics, τ_{SRH} increases with temperature if shallow levels dominate the recombination (See Figure 4.11 in Chapter 4). Although the radiative recombination coefficient lowers upon increasing temperature (See Table 1.1 in Chapter 1), the lifetime increase overcompensates this lowering.

8.7. Role of the dopant profile in the diode emitter

The excess carrier concentration, which is established during the forward biasing of the diodes is a parameter, which is not accessible experimentally. However, it influences significantly the electroluminescence efficiency. One needs to know the injection level at the base of the diodes and the difference in the excess carrier concentration, caused by the different processing of the diodes. Figure 8.10a illustrates the difference in the dopants distribution in the emitter by two different processing of silicon implanted with phosphorous [Arg2004].

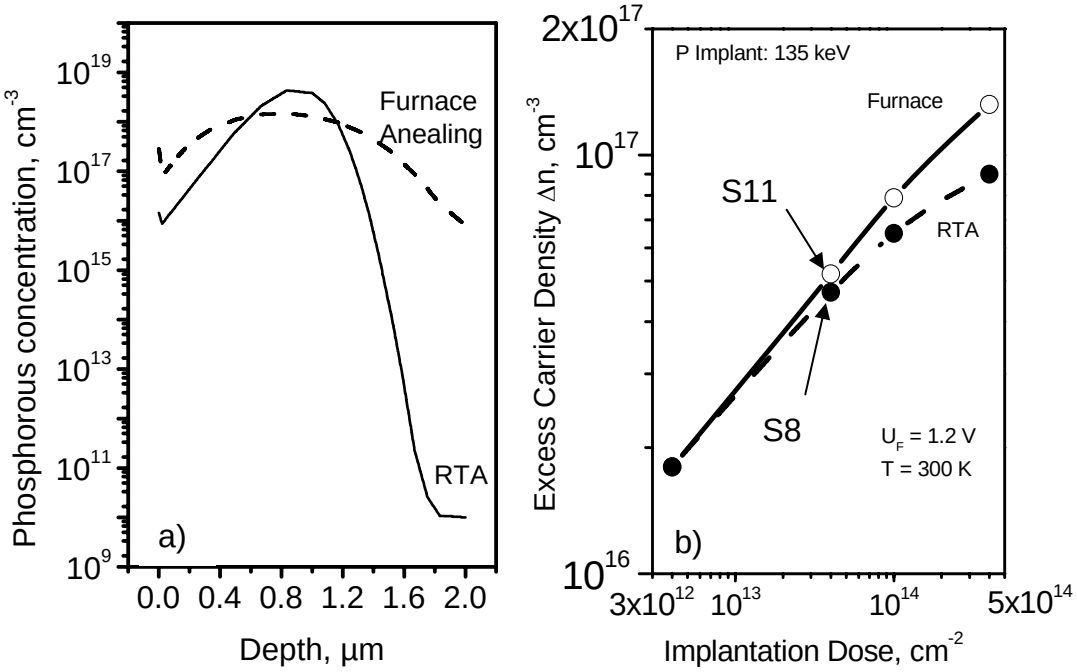

Figure 8.10. Distribution of the dopants in the emitter. Influence on the injection efficiency.
a) Phosphorous concentration profiles obtained by RTA and furnace annealing for samples implanted with the same implantation dose and energy (2×10^{-14} cm^{-2} and 750 keV, respectively)
b) Excess carrier density at the diode base. Dependence on the phosphorus implantation dose.

The excess carrier concentration can be estimated by modelling [Kit2005]. Results of a calculation for n^+-p diodes obtained with the process and device simulator "ISE TCAD" [ISE2001] are given in Figure 8.10b. The calculation assumes phosphorus implantation at 135 keV into a (100)-oriented substrate, doped with boron at concentration of 5×10^{14} cm^{-3}. The annealing conditions are taken in agreement with those given above for RTA or furnace annealing. The diode forward bias is assumed, U_F = 1.2 V. The calculation shows that at constant applied bias the excess carrier density Δn at the base increases with the implantation dose. Furthermore, furnace annealing yields a higher excess carrier density injection than RTA. The reason for the better carrier injection is the dopant profile in the diode emitter. Due the high peak concentration of dopants, not all of them are electrically activated. The dopant

concentration in RTA treated samples shows a higher maximum then that in furnace annealed ones and, consequently, less dopants are electrically activated by RTA. The phosphorus depth profile from the furnace anneal produces a higher injection than the corresponding RTA profile, because, effectively, more of the donors are active.

Thus, emitters produced by furnace annealing exhibit better injection properties than those produced by RTA. As the diodes operate in a regime, were the efficiency is mainly limited by nonradiative SRH processes ($\Delta n < 10^{17}$ cm^{-3}) (Figure 8.2), the higher injection level at the base leads to a higher efficiency. This is one reason, why furnace annealed samples show higher efficiency than those processed by RTA.

8.8. Gettering effect during the annealing step

To understand the role of local material quality (characterised by τ_{SRH}), which is modified during the annealing step, one should study the luminescence in samples under similar injection. One can compare the electroluminescence efficiency from furnace annealed or RTA processed samples, with similar excess carrier concentrations at the base under injection. The effect of the sample preparation and, respectively, the local material quality on the luminescence efficiency is studied ruling out the effect of the different injection levels on two phosphorus implanted samples, one prepared by RTA (sample S8) and the other by furnace annealing (sample S11). The implantation dose and energy in both samples are equal and under equal biasing, the injection levels are nearly equal, too (Figure 8.10b). The efficiency data are presented in the plot on Figure 8.11 as open and full circles. The difference in the efficiency of sample S11 (1.6%) and S8 (0.9%), is, obviously, related to the difference in their minority carrier lifetimes, $\tau_{SRH} \sim 30$ µs and ~20 µs, respectively. The higher minority carrier lifetime in S11 is a result of the improvement of the local material quality due to the treatment. We suppose that the main contribution is due to gettering effect during the annealing procedure, caused by the extended defects or by the phosphorus in the device emitter.

The furnace annealing, carried out for sample S11, is a relatively long process, which favours the diffusion of impurities into the implanted layer, cleaning the substrate and increasing the minority carrier lifetime. In contrast, the RTA procedure is only short time diffusion and the gettering effect do not occur to the same extend, as for the furnace annealing.

To verify the simulation results, similar analysis was performed on the data reported by Ng et al. [Ng2001] (Figure 8.11). One obtains an excess carrier concentration of $2\text{x}10^{17}$ cm^{-3} at bias of $U_F = 1.2$ V for their implantation and annealing conditions. Accordingly, a SRH lifetime of approximately 10 µs is expected in order to obtain the reported efficiency of 1.6%. This value is close to the device response time of 18 µs that was determined by the authors

experimentally. One can conclude, that the simulated excess carrier concentrations are close to those really existing in the samples.

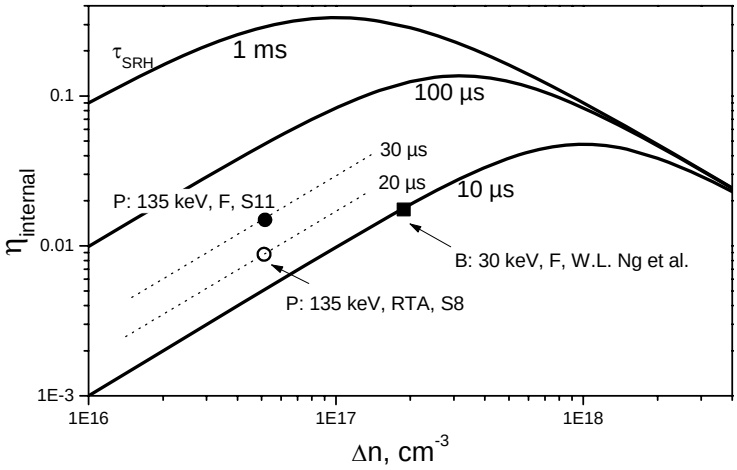

Figure 8.11. Internal quantum efficiency versus excess carrier concentration. Experimental data points for two n^+-p diodes are indicated, together with data from Ng et al. [Ng2001]. The position of the experimental data in the plot allows to give an indication about the SRH lifetime.

8.9. Internal quantum efficiency dependence on the injection

According to the model of bulk recombination (Paragraph 8.1) at low injection, the excess carrier concentration in the base is low and the predominant recombination mechanism is SRH recombination. Upon increasing the injection, the excess carrier concentration at the base increases, so does the band-to-band recombination contribution to the total recombination. Indeed, such behaviour is detected and it is demonstrated in Figure 8.12 for sample S11. The dependence of the electroluminescence efficiency on the current through the diode is measured for two temperatures 100 and 300 K. The behaviour of the efficiency curves upon increasing the current nearly resembles the behaviour of the efficiency upon increasing the excess carrier concentration in the base of the diodes (Figure 8.2).

The current dependence of the internal electroluminescence efficiency is in agreement with the prediction of the classical bulk recombination model (Paragraph 8.1).

At low temperature the SRH recombination is larger and the SRH lifetime is shorter as compared to those at room temperature. Therefore, the efficiency curve measured at 100 K is below that measured at 300 K. In fact, this observation reflects the anomalous temperature dependence of the band-to-band luminescence, which as discussed previously (Paragraph 8.6) is a result from SRH recombination at shallow levels.

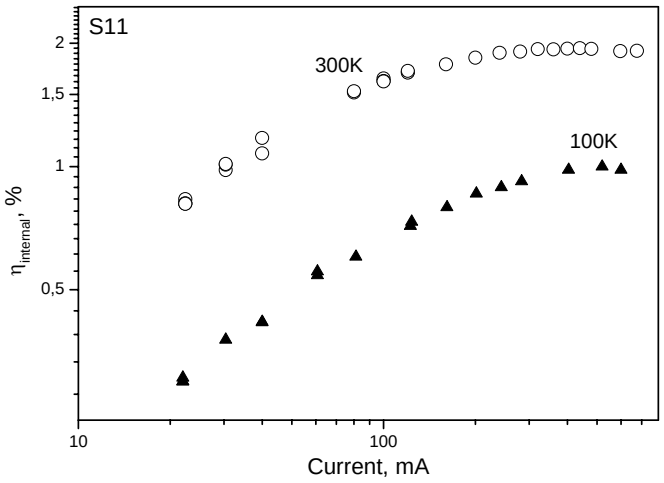

Figure 8.12. Internal efficiency dependence upon the current through the diode (Sample S11). At low currents the efficiency is lower because SRH recombination predominates. The difference in the efficiency at low and high temperatures reflects the anomalous temperature behaviour of the luminescence.

8.10. Sample thinning and disappearance of the luminescence

One important consequence of the bulk recombination model is that it does not require a specific position for the recombination of carriers within the base of the diodes to explain the high efficiency of the luminescence. Contrarily, the models involving confinement at the dislocation loops, either due to the mechanical strain field and modification of the semiconductor bands [Ng2001] or due to formation of bound excitons at dopant clusters [Sun2003, Sun2004], assume that the recombination takes place close to the layer modified by the implantation. Thus the luminescence, in view of the confinement models, should be generated in a thin layer close to the surface of the sample and should not depend on the thickness of its base. This difference between the models allows to judge about their adequacy [Arg2005] simply, by observing the luminescence upon thinning the base.

We use photoluminescence to characterize the luminescence enhancement from a sample with laterally varying thickness of the substrate wafer. Samples without junctions are designed in order to rule out the influence of the electric field in the p-n junctions, which perturbs the distribution of the minority carriers, generated by photoexcitation. Thus, a wafer of phosphorous doped ($5x10^{14}$ cm^{-3}) CZ silicon, covered with a 3.5 μm thick CVD-grown silicon layer, is implanted with phosphorus at 750 keV through a 10 nm thick scattering oxide. Implantation dose of $2x10^{-14}$ cm^{-2} is used. After implantation the sample is treated by RTA for 10 s at 1030°C. Crystal defects, such as dislocation loops and rodlike defects are observed down to about 1 μm depth from the surface (Figure 8.13). The epitaxy is used to improve the quality of the silicon layer prior to phosphorous implantation, by decreasing the concentration

of nonradiative recombination centres. The above implantation and the annealing are chosen in order to obtain a significant structural damage and high concentration of extended defects.

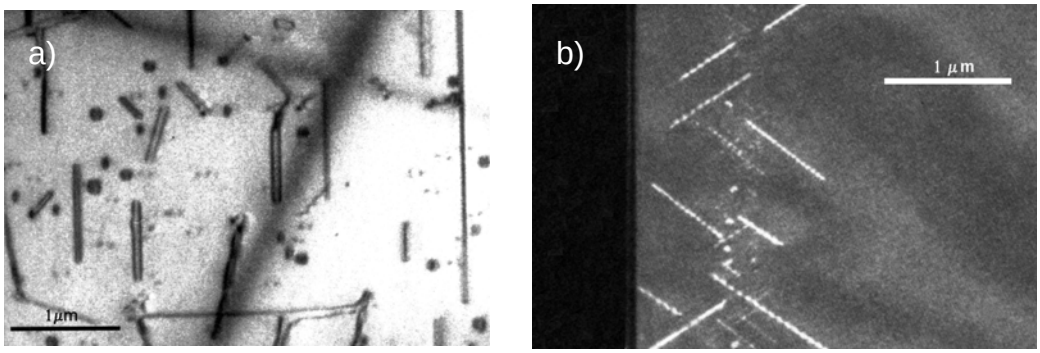

Figure 8.13. TEM images from the sample prepared by implantation with phosphorous in n-type substrates. a) plane view; b) crosssectional view.

Figure 8.14 shows that the temperature dependence of the band-to-band luminescence peak is anomalous, similarly to the observed anomalous temperature behaviour for the samples, previously discussed. The presence of extended defects and the anomalous temperature behaviour of band-to-band luminescence suggests that the radiative recombination in the samples with and without p-n junction is governed by the same processes.

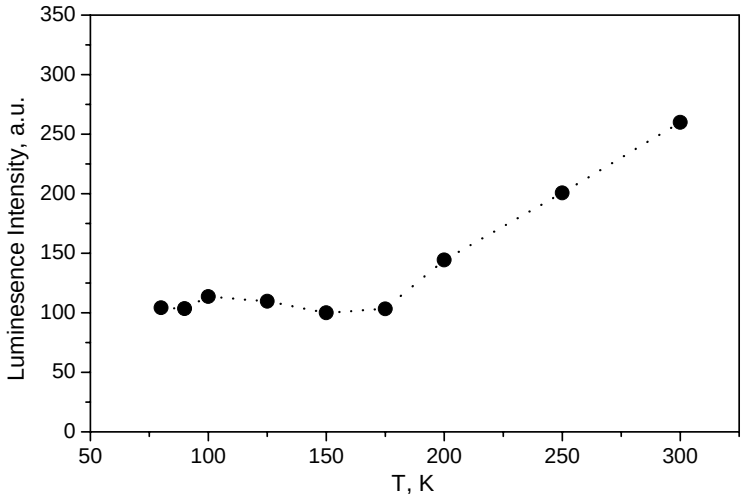

Figure 8.14. Anomalous temperature behaviour of band-to-band luminescence from phosphorous implanted sample without p-n junction.

To assess the contribution of the substrate and the implantation-modified layer to the luminescence enhancement material is removed from the rear side of the sample. The sample thickness is decreased to about 100 μm by grinding. The middle part of the sample is additionally thinned down to about 15 μm by a technique usually applied for TEM sample preparation (Figure 8.15a).

Photoluminescence mapping is carried out at 457 nm excitation wavelength (penetration depth in silicon ~ 0.4 μm) in order to generate the carriers as close as possible to the front surface. The excitation beam is directed to the front side, which contains the implantation modified layer. In order to minimize the surface recombination we removed the oxide by dipping in hydrofluoric acid and kept the sample during the measurement in a solution maintaining the silicon surfaces hydrogen terminated. Figure 8.15b shows the room temperature photoluminescence map. The luminescence in the thinned region is much lower than in the thick regions close to the edges. The intensity of the luminescence correlates with the thickness of the sample at the probed position.

Spectra taken in the centre of the sample and close to the edge (Figure 8.15c) show that the shape of the band-to-band peaks is similar, but the luminescence intensity from the thinned region is about 10 times lower than that of the thick regions at the edges. Thus, the contribution of the implantation modified layer to the readiative recombination in the sample does not exceed 10%.

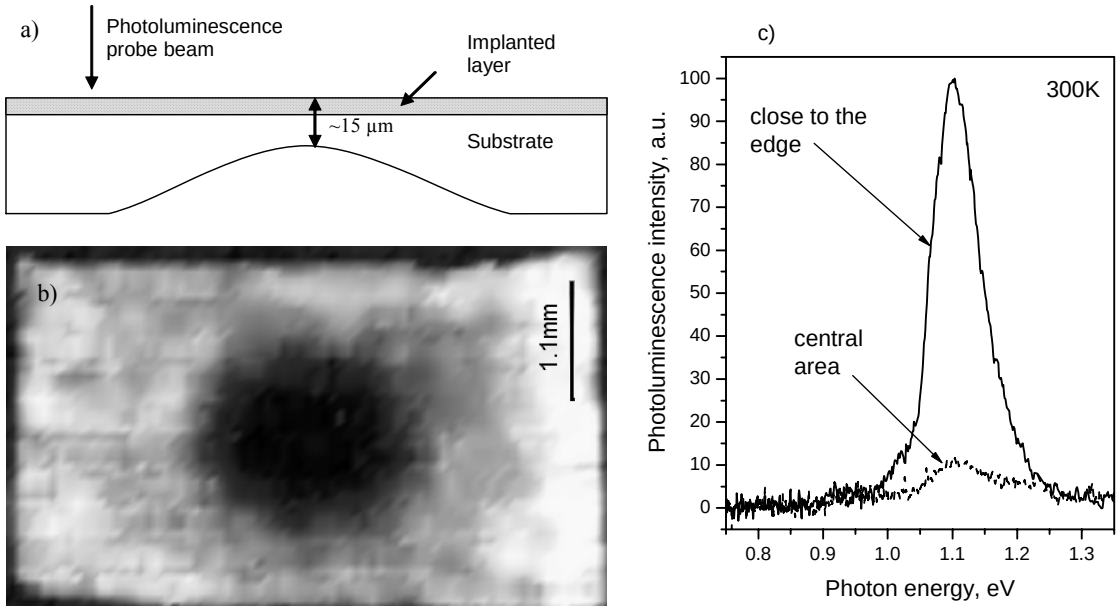

Figure 8.15. Dependence of the luminescence on the sample thickness. a) Sketch of the thinned sample profile. b) Room temperature photoluminescence map - darker areas correspond to a lower band-to-band luminescence. c) Spectra taken from the edge of the sample and from the middle of the tinned area.

Obviously, the enhancement of the band-to-band luminescence is caused mainly due to improvement of the radiative recombination efficiency in the substrate and not from implantation modified layer.

8.11. Summary

The processes leading to an enhancement of the band-to-band recombination in devices prepared by implantation and annealing are not related to a confinement effect at the implantation layer. The main factor contributing to the improvement of the luminescence appears to be the gettering effect of the implantation layer, which causes a decrease of the trap density in the substrate and thus decreases the nonradiative SRH recombination. As a result of that cleaning effect the radiative recombination gains on importance in the total recombination and thus the internal quantum efficiency of the light emitters is increased.

The doping profile in the implantation layer is an additional factor, influencing the efficiency. E.g. the furnace annealing results in a flatter dopant profile in comparison to RTA, which allows the device emitter to inject carriers more effectively at the base, reaching injection levels close to the optimal point for maximal radiative recombination efficiency. In the series of samples studied, the phosphorous implanted ones show higher luminescence efficiency than those implanted with boron. This can be due to the less pronounced getter effect of boron, appearing mainly during cooling down process [Miy1997].

Furnace annealed samples show always a higher efficiencies than those RTA treated. The furnace annealing compared to RTA offers enough time for the diffusion and gettering in the implantation layer of the traps, responsible for the nonradiative recombination.

It turns out, that the silicon light emitter based on implantation of dopants and annealing is a device, which uses a big volume from the substrate for generation of light. The depth where the band-to-band luminescence is generated exceeds the thickness of the implanted layer. The non appropriate wavelength of the emission (1.13 μm) and the bulk generated luminescence renders the application of such light emitter in the microelectronics difficult.

Chapter 9

Light emitters based on dislocation-related radiation

In this chapter, the possibility for realizing a light emitter, based on dislocation activity of silicon is discussed. Different methods for preparation of the dislocation rich region in silicon wafers are used. The dislocation-related emission is characterized by photo- and electro-luminescence spectroscopy.

Dislocation-related radiation is a promising candidate for crating light emitting devices in the sub-band-gap energy range of silicon:

- The dislocation-related line D1 shows relatively low quenching upon increasing the temperature.
- Dislocation-rich areas can be created in a well defined depth of the wafers, resulting in a small active region of the devices.
- The wavelength of about 1.5 μm, which is characteristic of D1 radiation, coincides with the transparency window of the optical fibres used in the telecommunication [Kar2000].
- Silicon is transparent in that wavelength range and optical waveguides and modulators prepared on silicon can be utilized for on-chip signal transmission.

There are several reports in the literature, discussing the possibility of utilizing the dislocation-related radiation for silicon based light emitters. Sveinbjörnsson and Weber [Sve1996] found strong room temperature D1 electroluminescence from samples with dislocations, formed during recrystallization of a wafer surface. The dislocations were generated after the sample surface had been melted by fast scanning with a focused high power laser beam. Diodes

fabricated by diffusion of dopants on the dislocation-rich side of the wafer showed room temperature D1 luminescence under forward biasing.

Light emitting diodes, based on dislocations with a remarkable internal efficiency of nearly 5% at room temperature have been reported by Kveder et al. [Kve2004, Kve2005]. Dislocations in the devices were produced by a macroscopic plastic deformation, which is not is appropriate for microelectronic applications. A method acceptable for the technology should be found to produce dislocation-rich areas in a well-defined depth in order to have a localised active area of the devices.

Three different ways for the generation of dislocations will be discussed:

- *Extended defects, generated by implantation, followed by annealing*. As it was shown in Chapter 8, such treatment can produce dislocations in the subsurface region of the wafers.
- *Graded buffers between Si and SiGe.* One can make use of the different lattice constants of silicon and silicon-germanium mixed layers. The preparation of SiGe mixed layers on silicon wafers is associated with the growth of graded buffers, in which the alloy composition changes across the buffer from pure silicon to the composition of SiGe layer. Extended defects are formed in the buffer compensating for the lattice mismatch and they are well localised between both nearly defect free regions of the silicon substrate, at the bottom, and the silicon germanium mixed layer at the top.
- *Dislocations produced at the interface between two directly bonded silicon wafers*. The hydrophobic wafer direct bonding with well-defined misorientation is a method to create a well reproducible dislocation network at the bonding interface.

Samples prepared by these techniques are analysed and the possibility of electrical injection of carriers are studied.

9.1. Radiation from implantation induced extended defects

Extended defects generated by implantation and annealing treatment are one possibility to create a dislocation rich region in the silicon wafer. Not only dopants, but also silicon ions can be implanted in order to produce extended defects, without influencing the doping concentration. An additionally created p-n junction, close to the area rich on extended defects, can be used to excite the luminescence.

We prepare diodes by boron diffusion on n-type, phosphorous doped ($5x10^{15}$ cm^{-3}) wafers implanted with silicon ions at energy 200 keV and 450 keV and subsequently furnace annealed (950°C for 30 min) to form extended defects near the junction [Hoa2006]. The p-n junction formed by the boron-diffusion (dopant concentration $5x10^{19}$ cm^{-3}) is at a depth of about 400

nm. It is situated between two dislocation-loop-rich regions, resulting from the implantations (Figure 9.1).

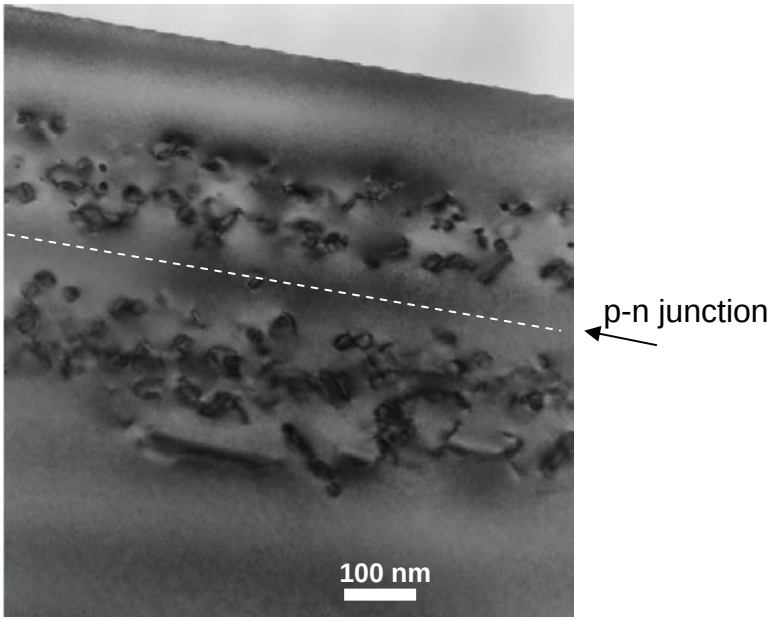

Figure 9.1. TEM image of the diode by prepared by boron diffusion. The damaged areas are due to implantation of silicon at 200 and 450 keV and subsequent annealing at 950°C. The line shows the position of the p-n junction.

Thus, under bias, injection of carriers occurs in dislocation rich regions on both sides of the junction. Electroluminescence, measured at high current densities (250 A/cm^2), reveals the presence of dislocation-related radiation. Figure 9.2a shows the evolution of the spectra upon increasing the temperature of the substrate. At low temperatures, the radiation is even dominated by the dislocation-related emission and the band-to-band luminescence is nearly not present. The dislocation radiation at 27 K is dominated by D1 at 0.81 eV, although D2 and D3 are also detected.

9.1.1. Thermally induced shift of D1 line

Upon increasing temperature, the D1 line shifts. In the range above 100 K it shows a red shift, which nearly coincides with the band gap narrowing [Web1999] upon increasing temperature (Figure 9.2b). The shift can be related to the energetic position of the levels in the band gap responsible for the D1 transition. D1 could be associated with one deep and one shallow level, so that the shallow one follows the temperature shift of the band gap while the deep level remains not influenced.

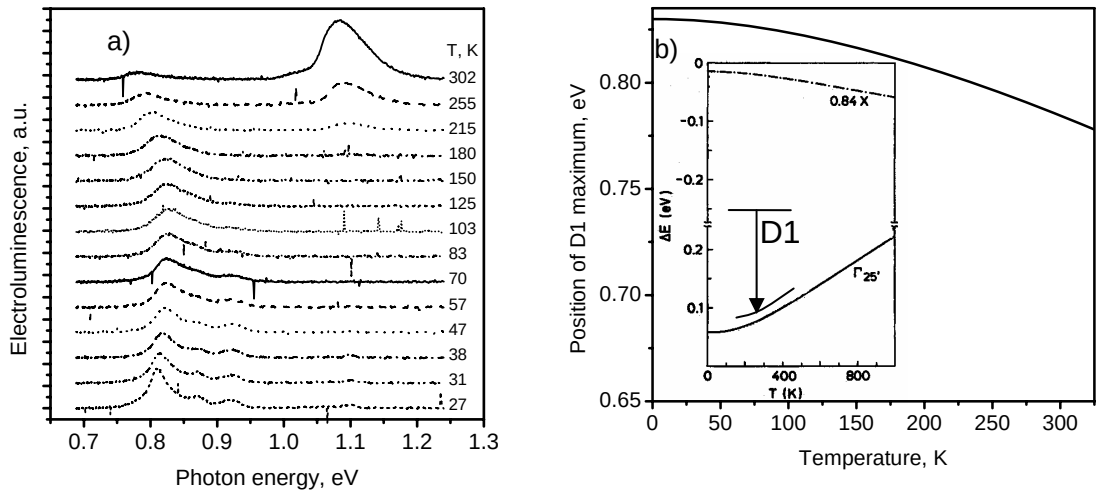

Figure 9.2. Electroluminescence from a silicon implanted diffusion diode. a) Evolution of the spectra upon increasing temperature b) Shift of D1 line with temperature. The solid cure represents the band gap shrinkage shifted with 0.33 eV down to the position of D1. Inset: Temperature shift of conduction and valence band edges [Lau1985] with temperature. The D1 transition is also indicated.

The difference in the temperature behaviour below and above 100 K is probably related with the mechanisms, which are responsible for the band gap narrowing. In the temperature interval below 100 K the band gap narrowing is dominated mainly by the elongation of the crystal bonds with temperature and is related to the pressure coefficient of the gap energy and the thermal expansion coefficient. In the interval above 100 K the phonon-electron coupling becomes the limiting mechanism [Web1999, Lau1985].

9.1.2. Temperature dependence of D1 and band-to-band electroluminescence intensity

The temperature dependence of the intensity for both, band-to-band and the D1 radiation is measured (Figure 9.3). In a broad temperature range from 80 K to about 210 K, only D1 is observed. Strong band-to-band luminescence appears above 210 K. At room temperature, the band-to-band luminescence dominates, although D1 is still present. The presence of strong anomalous temperature behaviour of band-to-band luminescence indicates strong recombination activity of the dislocations at low temperatures.

The internal quantum efficiency of band-to-band electroluminescence measured at room temperature is 0.2% and that for D1 radiation nearly 0.04%. As the integrated D1 emission at 80 K is nearly 3 times higher compared to that at 300 K (Figure 9.3), one can estimate the 80 K quantum efficiency of the D1 emission to about 0.12%.

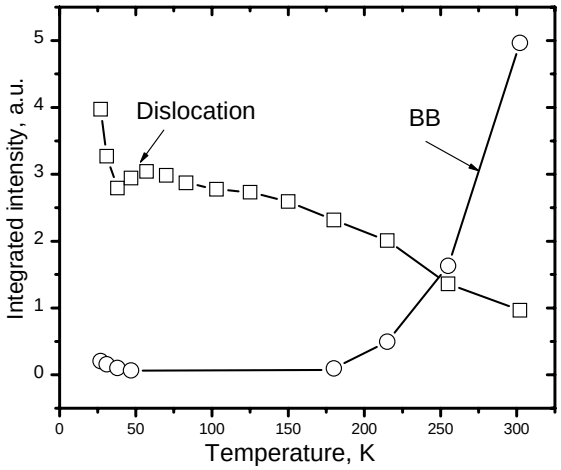

Figure 9.3. Temperature dependence of the integrated intensity of the electroluminescence. The dislocation-related luminescence shows quenching. Strong band-to-band luminescence is observable only at temperatures above 200 K.

The room temperature internal quantum efficiency at high current density is lower compared to the band-to-band one. It is expected that the efficiency of the dislocation radiation is injection dependent (as it was shown in Chapter 8 for band-to-band), which will give a possibility to find optimal injection conditions for efficient D1 emission.

9.1.3. Injection behaviour of D1 and band-to-band efficiencies

The efficiency dependence on the excitation level is different for the band-to-band and for the D1 radiation. The D1 efficiency decreases on increasing the current, while the band-to-band luminescence increases (Figure 9.4). Thus, an optimal efficiency for the D1 emission is expected at low injection levels. The D1 efficiency decrease upon increasing the injection can be attributed to a saturation of the recombination centres at the dislocations. As the dislocation recombination becomes less effective, more carriers are transferred in to the bulk, contributing to a higher band-to-band luminescence.

The carrier recombination in the diodes is dominated by nonradiative processes as the internal quantum efficiencies of the radiative ones are below 1%. Two possibilities come in mind to overcome the limitation of D1 efficiency imposed by the recombination saturation. One is to increase the radiative recombination activity of the dislocations, so saturation is prevented or is reached at higher injections, and the other is to increase the dislocation density, creating more centres for radiative recombination. The first possibility could be achieved by a controlled decoration with metals, so that dislocation recombination activity increases [Kit1995d, Hig1993a]. However, one should take into account that there is only a small range of

decoration concentrations, which leads to an improvement of the recombination without impairing the dislocation radiative properties. The second possibility could be achieved by the formation of an extended dislocations-rich region, so that the dislocations dominate the recombination.

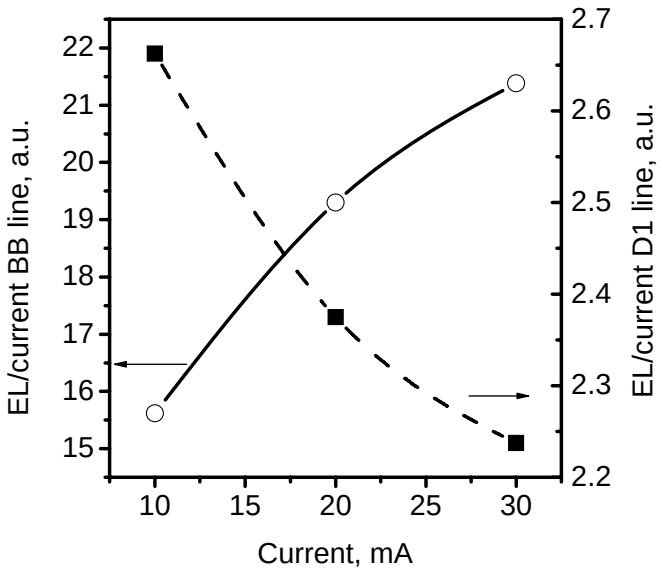

Figure 9.4. Injection dependence of the D1 and band to band emission from the diode. Upon increasing the current, the intensity/current ratio of the electroluminescence for D1 decreases, while for band-to-band radiation it increases.

9.2. Dislocation radiation from SiGe buffer layers

Silicon-germanium relaxed buffer layers offer a region rich in dislocations, which can be used as the active part of a light emitter [Arg2006]. Alternatively, the band-to-band radiative transition in the SiGe layers, grown on the buffer can be also utilized for light emission. The smaller band gap of SiGe leads to a red shift of the band-to-band radiation and, consequently, less absorption in silicon.

In our experiments, silicon wafers with an epitaxially grown 3 μm thick relaxed SiGe buffer, covered with a cap layer of uniform composition $Si_{80}Ge_{20}$, 4 μm thick, are investigated by means of photo- and electroluminescence. For electroluminescence measurements a p–n junction is prepared in the cap SiGe layer. Boron is implanted (at energy 50 keV, and a dose $5x10^{14}$ cm^{-2}) in the cap layer of an n–type SiGe sample and then the sample is annealed in a furnace (in N_2 ambient at 1000 °C, 20 min and finally in H_2 at 400°C for 60 min). The activity of the dislocations and their contamination level is determined by temperature dependent EBIC measurements.

The EBIC micrograph from the buffer, obtained after removal of the cap layer, is shown in Figure 9.5a. It illustrates the typical cross-hatch pattern of the dislocations. Temperature dependent EBIC investigation of the electrical recombination activity of these samples shows that dislocations are predominantly active at low temperatures (Figure 9.5b). According to the model of the dislocation electrical activity (See Chapter 1) their contamination is low, because their behaviour corresponds to type 2 (high activity at low temperature and low activity at room temperature). As it was shown in Chapter 4, room temperature D1 radiation from the dislocations can be expected, because of their EBIC type 2 temperature behaviour.

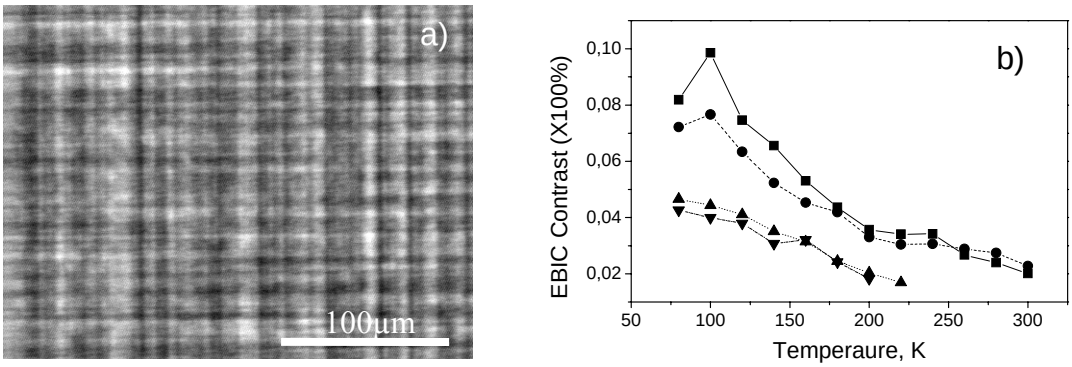

Figure 9.5. a) EBIC micrograph from the SiGe buffer layer, showing the typical cross hatch pattern of misfit dislocations. b) Temperature behaviour of the EBIC contrast from dislocation in the buffer. The different curves are measured from different places, randomly taken.

The photoluminescence spectra shown in Figure 9.6a, exhibit two broad peaks. The first at about 0.8 eV predominates at 80 K and decreases at higher temperatures. That peak can be attributed to the dislocations in the buffer. Besides the dislocation radiation, a broad emission band between 1.0 and 1.1 eV occurs, which is attributed to radiative band-to-band transitions in the buffer.

Room temperature electroluminescence spectra (Figure 9.6b) exhibit features similar to that of the photoluminescence - a peak at about 0.8 eV and a broad band-to-band feature.

The broad band-to-band peak in both electro- and photoluminescence is a attributed to radiative recombination in the buffer, because its maximum appears between those expected for silicon (1.1 eV) and for $Si_{80}Ge_{20}$ epitaxial layer (1.0 eV). In the buffer, the Ge content is less than 20% and thus the band gap is shifted towards that of silicon. Accordingly, the band-to-band peak is broadened due to the varying Ge and Si concentrations in the buffer.

The overall intensity of the electro-and photoluminescence in these samples is low compared to the band-to-band luminescence obtained from the samples implanted with dopants in pure silicon (Chapter 8). The room temperature internal quantum efficiency of the samples prepared

on SiGe mixed layers is estimated to about 0.01%. Although, the SiGe buffer layers are localised in depth at and emit at 1.5 μm (0.8 eV), the maximal efficiency which can be reached is too low. The dislocation radiation should be further enhanced for such structures to find an application as light emitters.

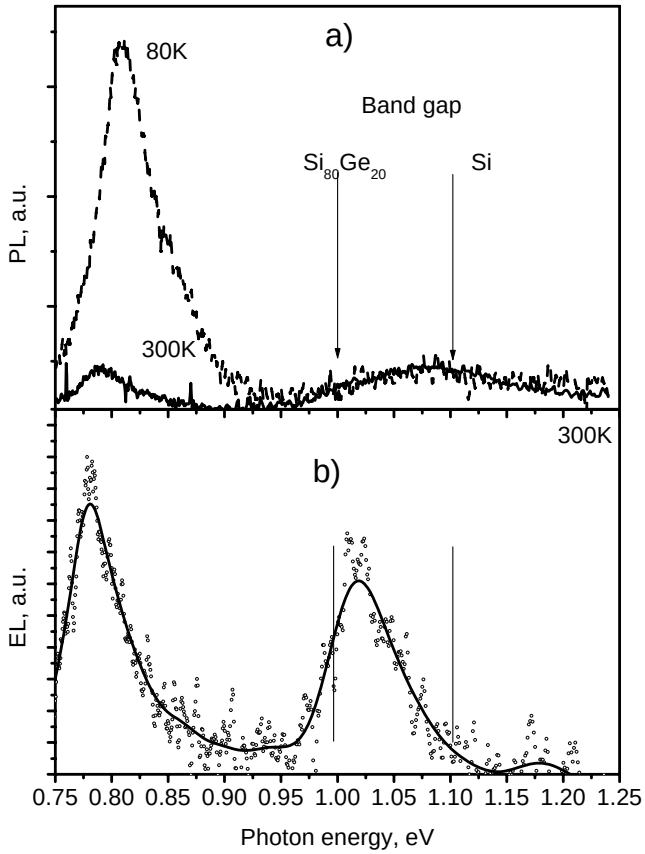

Figure 9.6. Luminescence from SiGe sample. a) photoluminescence spectra at 300K and 80K show band-to-band and D1 line radiation. b) EL on the same sample at current density of 8A/cm^2.

9.3. Light emission from dislocation networks prepared by direct wafer bonding

In this section the radiative properties of dislocations, created at the bonding interface between two direct bonded wafers are studied. The spectral features in the sub-band-gap energy region of the luminescence are shown to be correlated with the bonding parameters. The persistence of the dislocation-related radiation upon increasing temperature as well as its distribution across the bonding interface are investigated. Concepts for electrical injection of carriers into the network are discussed.

9.3.1. Preparation of two dimensional dislocation network

9.3.1.1. Principles

Semiconductor wafer direct bonding is a key process in the production of advanced substrates for integrated devices and in the production of three dimensional micro-electro-mechanical systems (MEMS) [Rei2006]. There are many different techniques for preparing a permanent contact between two silicon wafers, mainly including a layer of different material or different crystalline structure mediating the contact at the interface.

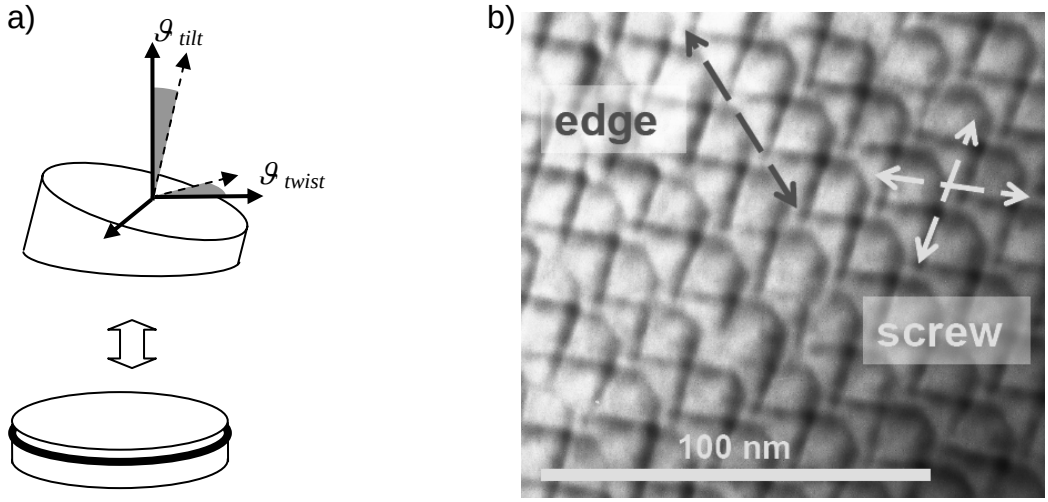

Figure 9.7. Formation of a regular dislocation network at the interface during direct wafer bonding. a) Schematic of wafer direct bonding. b) TEM plane view of a periodic dislocation network fabricated by direct bonding of (100) silicon wafers. The directions of screw and 60° dislocations (marked as edge) are indicated.

Bonded hydrophobic wafers are characterized by one completely different interface. The missing of mediating oxide at the interface means, that two silicon lattices are in contact, as in the case of bicrystals. Crystal defects (dislocations) are generated, forming a two-dimensional network in order to adapt both crystal lattices. The dislocation structure depends on the misorientation (Figure 9.7a). In general, the twist component causes a network of pure screw dislocations, while the tilt component is compensated by a periodic array of 60° dislocations. Figure 9.7b illustrates these two dislocation sets in a plane TEM image: The Burgers vector, *b*, of both dislocation is of the type

$$b = \frac{a}{2}\langle 110 \rangle . \qquad (9.1)$$

Here *a* stands for the lattice constant of silicon (a = 0.543 nm).The periodicity L_{tilt} and L_{twist} of both sets can be related to both misorientation angles ϑ_{tilt} and ϑ_{twist} in the following manner:

$$L_{tilt} = \frac{a}{\sqrt{2}} \frac{1}{\sin(\vartheta_{tilt})}, \text{ and } L_{twist} = \frac{a}{\sqrt{2}} \frac{1}{\sin(\vartheta_{twist})}. \qquad (9.2)$$

The larger the mismatch is the shorter the periods L_{tilt} and L_{twist} of the dislocation arrays. Wafers of different orientation can be bonded to each other, resulting in a mismatch of several degrees.

9.3.1.2. Experimental

CZ (100)-oriented silicon wafers with p-type conductivity and a resistivity of about 25 Ωcm are used for the experiments. After cleaning, the wafers are bonded using commercial bonding equipment 'CL 200'. The wafer pairs are then annealed for 2 hours at 1000 °C under inert atmosphere to increase the bonding strength. The dislocation network for the given misorientation (twist and tilt value, respectively) can be well reproduced [Kit2005a]. Since wafer bonding is carried out on standard Si wafers, the bonded interface is several hundred micometers below each outer surface. Therefore, thinning of one of the wafers is required to access the dislocation network.

Thin layers are produced by the so-called smart cut process [Bru1995, Bru1997]. Here, one of the wafers is implanted with hydrogen with a dose higher then $1x10^{16}$ cm^{-2} prior to bonding. After bonding, an annealing step follows that results in the formation of hydrogen bubbles located parallel to the bonded interface at a depth easily controlled by the implantation energy. The growing bubbles cause stress resulting in microcracks and finally in the removal of the thin top layer. Thus, the residual thickness of the upper layer is below 1 µm.

A further thinning of the layer, below 100 nm, can most effectively be done by oxidation and removing of the grown oxide.

The bonding of the samples investigated here is performed in air. The bonding parameters are listed in Table 9.1. The interfaces are 200 nm beneath the sample surface.

Sample	Interface	ϑ_{twist}	ϑ_{tilt}	L_{twist}, nm	L_{tilt}, nm
#1	(100)/(100)	6.5°	0.7°	3.4	31.4
#2	(100)/(100)	1.5°	0.53°	14.7	41.5
#3	(100)/(110)	30°	25°	0.8	0.9

Table 9.1. Bonding parameters for the wafers whose spectra are shown in Figure 9.8. The twist and tilt angles are measured with respect to <100> directions of the wafers.

Sample #1 and #2 are produced by bonding of wafers with (100) surfaces, while sample #3 is produced by bonding of two wafers one oriented to (100) and the other to (110) surface, which results in large misorientation angles between (100) planes.

9.3.2. Tailoring of the spectra by the misorientation angles

Fig. 9.8 shows photoluminescence spectra of bonded-wafer-samples measured at 80 K. We will show that the luminescence spectrum can be tailored by the misorientation angles.

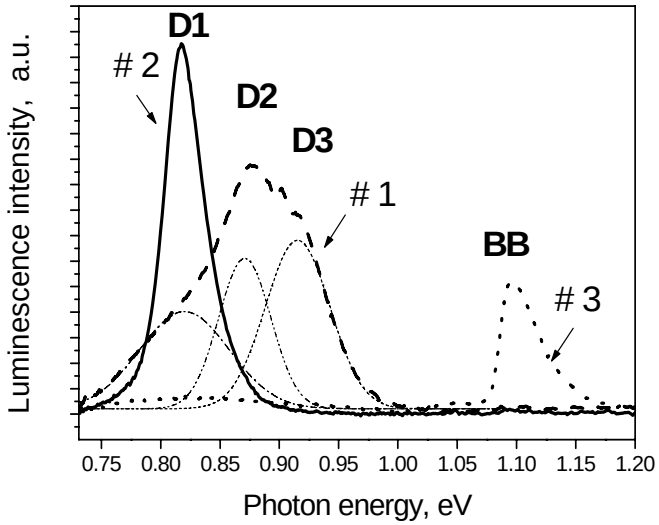

Figure 9.8. Tailoring the photoluminescence spectrum at 80 K by the choice of misorientation: Radiation from samples containing different dislocation networks, formed by direct bonding of p-type Si wafers (25 Ωcm) (See Table 9.1).

The combination of twist and tilt angles (Table 9.1) of sample #2 results in a dominance of the D1 line. The photoluminescence of all other dislocation-related features and the band-to-band transitions are strongly suppressed. Surprisingly, the dislocation network in this sample is not as dense as in the other two, but it gives the strongest D1 luminescence. Sample #3 exhibits the smallest period of the dislocation arrays, but it almost does not show D luminescence. One can assume that the dislocation network has an optimal density, and respectively, optimal distances between the dislocations in order to emit strong D1 radiation.

Sample #1 shows a broad peak with a maximum at about 0.87 eV (D2) and well seen shoulder at about 0.93 eV (D3). The presence of the D3 line without D4 is a peculiarity, which is difficult to explain, because all other experiments (See Chapters 4 and 5) show that D3 and D4 are strongly related indicating that D3 is a phonon replica of D4. The D3 line cannot be related to a contamination (like VID3 in Chapter 5), because spectra with the same shape are observed across the entire sample, and a contamination equally distributed over the entire surface is not probable. Not relaxed dislocations (Chapter 5) can be excluded too, because the samples have not been subjected to any low temperature deformation.

The well reproducible alignment which is possible to achieve by the misorientation angles allows to select the emission wavelength of the dislocation network and thus to create light emitters of different discrete colours.

The emission of sample #2 exhibits a spectrum with only one line at 0.8 eV, therefore, it seems very suitable for light emitting devices. However, the question of the temperature stability of the dislocations radiation in sample #2 needs to be answered.

9.3.3. Temperature stability of the D1 luminescence generated in the dislocation networks.

Figure 9.9 shows that the intensity of the D1 radiation from sample #2 decreases upon increasing the temperature. However, the D1 radiation is still the most intensive feature in the spectrum, and at room temperature it is about ten times stronger than the band-to-band luminescence. As shown in the inset of Figure 9.9, the temperature dependence of the peak position of the D1 line $E_{D1}(T)$ follows the temperature dependence of the band gap $E_g(T)$ [Web1999] red-shifted by 0.33 eV:

$$E_{D1}(T) = E_g(T) - 0.33 \text{ eV}. \qquad (9.3)$$

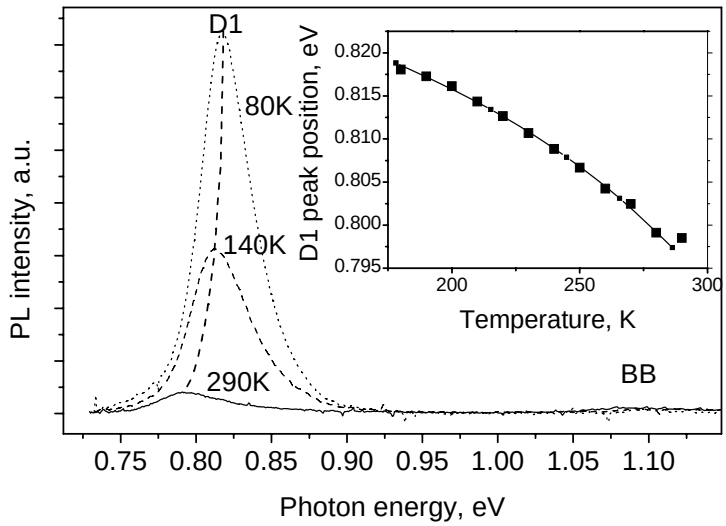

Figure 9.9. Temperature quenching of D1 luminescence. Inset: The shift of the D1 follows the band gap shrinkage of silicon on increasing the temperature.

Such behaviour is characteristic for an asymmetric position of the levels in the band gap responsible for D1 transition (See paragraph 9.1). This radiation is, indeed, typical D1 emission.

To estimate the achievable quantum efficiency of the D1 radiation, one can use the fact that the efficiency of the band-to-band emission, observed at room temperature, is at least 10 times smaller than that of D1. The dislocation network is surrounded by defect free crystal and the corresponding efficiency of the band-to-band luminescence is determined by the excess carrier

concentration and the nonradiative recombination processes (Chapter 8). The band-to-band efficiency exhibits an internal reference depending on SRH lifetime and the injected carrier concentration [Kit2005]. For a typical effective SRH lifetime of 5 μs [3], and an excess carrier density of 10^{17} cm^{-3}, one obtains an internal efficiency of band-to-band emission of ~ 0.5% (Figure 8.2). Since, the intensity of D1 in identical measurement conditions is 10 times stronger it should yield a D1 efficiency of about 5%. Thus one can expect that at achievable injection levels the dislocation luminescence at room temperature can reach an internal efficiency of several percent.

9.3.4. Macroscopic homogeneity

Failure in the bonding will destroy the homogeneity of the interface and this can cause the disappearance of dislocation luminescence. Photoluminescence mapping can be used to find areas of non-uniform wafer bonding. Figure 9.10 shows such a map on a piece of sample #2 where bonding inhomogeneities are present. The map of D1 intensity is taken at 80K. Circular areas are found in which the D1 intensity changes stepwise. Spectra taken at different positions inside the defected areas do not differ in shape from the spectrum taken outside.

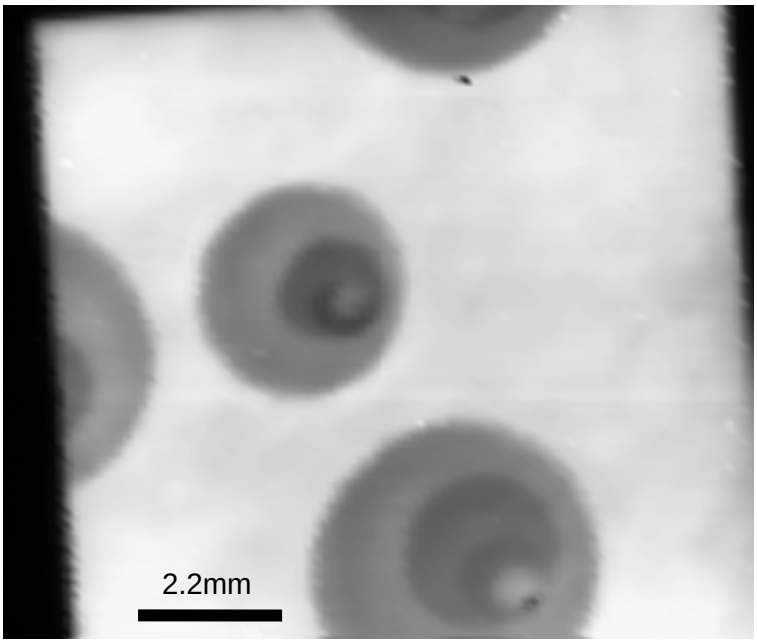

Figure 9.10. Circular inhomogeneities detected by photoluminescence mapping on sample with dislocation networks. The darker areas indicate a decreased D1 luminescence.

[3] The value of τ_{SRH} = 5 μs used here for the effective lifetime is based on a trap density $N_T = 2 \times 10^{13}$ cm^{-3}, a carrier capture cross-section $\sigma = 10^{-15}$ cm^2 and a carrier thermal velocity $V_{th} = 10^7$ cm/s one calculates from $\tau_{SRH} = 1 / (N_T \cdot \sigma \cdot V_{th})$ a lifetime of 5 μs. The trap density $N_T = 2 \times 10^{13}$ cm^{-3} results from the assumption that the dislocation network, with a distance of 10 nm between the dislocations, dominates the recombination in a volume of 100 μm thickness (~ diffusion length) and that each dislocation exhibits 10 states/traps per μm.

One possibility to explain the appearance of such circular areas is by the presence of micro-sized particles at the interface.

The wafer direct bonding is very sensitive to the flatness of the surfaces, which are subject to bonding, and to micrometer-sized particles accidentally appearing at the interface. As the forces governing the contact between both wafers are only short-range acting, it is possible to have non-bonded areas around such inclusions. Their lateral extension depends on the elastic properties of the wafers in contact and the height of the particle causing the disturbance. For example, a particle of about 1 μm in diameter, trapped between two silicon wafers (diameter 100 mm, thickness d = 525 μm), leads to an unbonded area of about 0.5 cm in diameter [Rei2006]. The gap caused by particles depends also on the thickness of the wafers. Because thinner wafers are more easily deformable, a reduction in wafer thickness results in a considerable decrease of the unbonded area. Nevertheless, the presence of dislocation-related luminescence inside the defected areas (Figure 9.10) shows that a dislocation network is present there. Its activity is influenced probably by contamination, which causes locally fluctuation in the luminescence intensity in these circular areas.

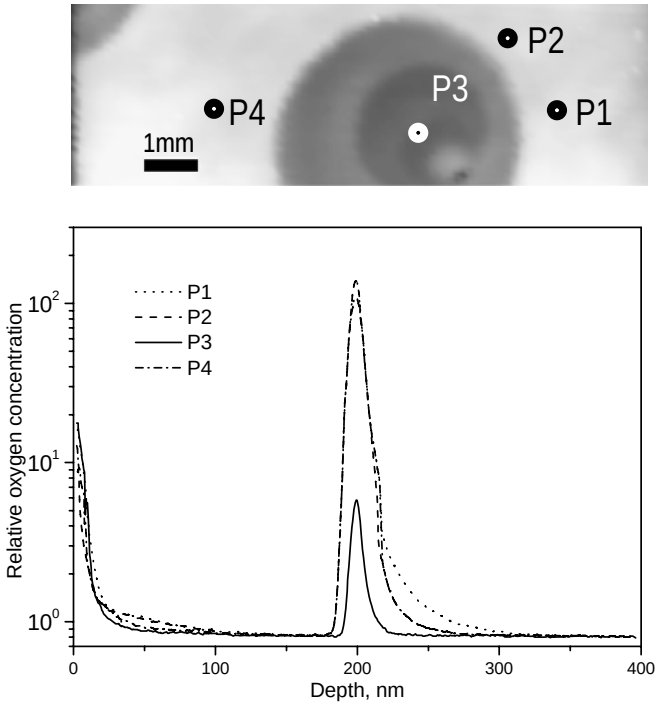

Figure 9.11. a) PL micrograph of the D1 line intensity across the sample shows non- uniform intensity distribution. b) SIMS profiles show an increased concentration of oxygen at the interface at the position of strong D1 luminescence. The oxygen concentration is measured relatively to the concentration of the oxygen in the substrate.

The stepwise distribution of the luminescence signal, forming not concentric circles in the defect areas, is an indication for a self-organised structuring. Anyway, it is found that the

intensity of the D1 line correlates with the oxygen concentration at the bonding interface (Figure 9.11). Secondary ion mass spectroscopy (SIMS) depth profiles, taken at positions of differing D1 intensity, reveal that the concentration of oxygen inside the circular area is nearly an order of magnitude lower than the concentration outside. It is seen, that the highest intensity in the photoluminescence map corresponds to the highest oxygen concentration at the interface. There are two ways to explain this observation. First, the D1 luminescence is enhanced due to the presence of oxygen (Chapter 2, Paragraph 2.14) or second, one can consider a process, which leads to decreasing of the oxygen concentration at the interface, and independently to that, is responsible for the decreasing of the dislocation radiation. That second suggestion is more relevant to the experience made on multi crystalline material, where metal contaminations and not oxygen appear responsible for the appearance of strong dislocation electrical activity and dislocation luminescence.

9.4. Concepts for electrical excitation of the dislocation network

The photoluminescence measurements show that the dislocation-related luminescence generated in a dislocation network might be sufficiently strong even at room temperature and, then, could be utilized for a light emitting device. The further problem, which needs to be solved, is the electrical injection of minority carriers. Two injection methods will be discussed here:

- Injection by a p-n junction just at the interface or in the vicinity of the network
- Injection by tunnelling through an oxide layer in a MOS structure

The most direct way to prepare p-n junction is to bond of two wafers with different type of conductivity. Under forward bias, part of the carriers flowing through the junction recombines at the dislocations in the network. Such devices have been demonstrated [Sve1998] giving strong electroluminescence in the range of 0.8 eV at low temperatures. However, the abrupt junction formed between the wafers does not allow optimization of the injected carrier concentration at the dislocations in the network (e.g. by adjustment of dopant concentration profile at the emitter (Chapter 8). Alternatively, a p-n junction just above the dislocation network, prepared by implantation and annealing, allows adjusting of optimum injection of carriers by the doping profile in the emitter. In addition, one can use the getter properties of the dopants and implantation induced extended defects to modify the activity of the dislocation in the network and the surrounding substrate material (Chapter 8).

Another method of injecting carriers into the sample is tunnelling through a thin silicon oxide layer [Liu2000, Lin2001, Che2001, Che2004] in a MOS structure. As recently demonstrated on defect free silicon, there is a possibility to obtain strong band-to-band luminescence by biasing the silicon substrate in a way that an accumulation layer is formed. In case of n-type doped substrate, the hole current occurs by tunnelling through the oxide and it is a source of minority carriers in the accumulation layer.

9.4.1. Electroluminescence from diodes prepared by implantation and annealing

Here we will discus devices with injection, prepared by implantation and annealing. Room temperature electroluminescence from dislocation networks prepared by wafer bonding is obtained from devices with a structure shown in Figure 9.12a. Two n-type wafers, doped to about $1x10^{15}$ cm^{-3}, form the bonding interface at a depth of 3 μm beneath the surface. The depth of 3 μm is necessary for the preparation of the junction. A p–n junction is prepared by boron implantation at energy 50keV and dose of $1x10^{15}$ cm^{-2}, furnace annealed at 1000°C in N_2 atmosphere. Aluminium for ohmic contacts are deposited at the front side of the diodes and the samples are annealed at 420°C for 30 min in hydrogen atmosphere. The back side contacts are prepared by rubbing InGa alloy after the annealing.

The effect of the dislocation network is seen when comparing the electroluminescence spectra from the devices containing a dislocation network with those, prepared without dislocation network. Here, a spectrum of sample S24 (Chapter 8) is taken as reference, because its implantation dose and annealing treatment are close to that of the sample containing the dislocation network. In the device with a bonding interface there are two regions, rich in extended defects, which can generate dislocation luminescence - the implantation region containing dislocation loops (Chapter 8) and the bonding interface with the dislocation network. Sample S24 contains only dislocation loops in the implanted region. Figure 9.12b compares the normalised electroluminescence spectra measured from the device with dislocation network with that from sample S24 at room temperature. Sub-band-gap radiation is detected only from the diode with dislocation network, indicating that the room temperature sub-band-gap radiation is related to the presence of the dislocation network.

The dislocations act as conductive channels, which are able to transport minority carriers without recombination at distances exceeding several millimetres [Yu2006 , Yu2006a]. The potential at the dislocation network is attractive for the minority carriers injected by the p-n junction and repulsive for the majority carrier (Chapter 1). Once, the minority carriers enter the dislocation network, they can move within the network until they recombine at a centre giving

D1 radiation, at a nonradiative centre, or they can escape the dislocation network and recombine in the bulk, contributing to band-to-band radiation. Thus, the minority carriers become spread over the entire network area and do not recombine locally under the junction.

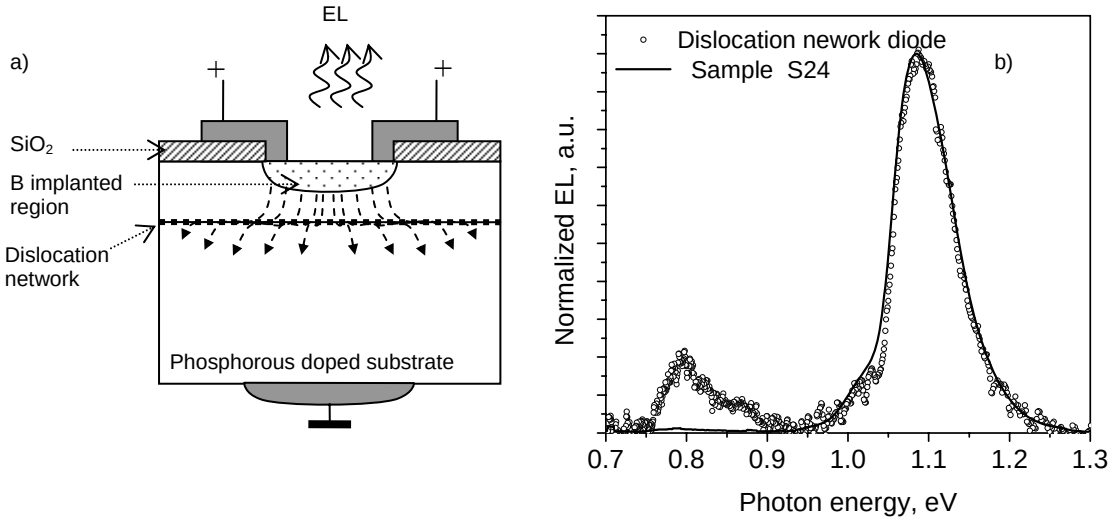

Figure 9.12. a) Structure of the diodes containing dislocation network close to the p-n junction. Electroluminescence at 300 K is measured by forward biasing. The minority carrier current spreading at the dislocation network is illustrated by dashed lines. b) Normalized electroluminescence spectra from the diode with dislocation network compared with the spectrum of a diode without dislocation network S24(Chapter 8).

It turns out, that the dislocation network leads to a spreading of the injected carriers over the entire area of the structure (Figure 9.12a). Thus, the intensity of radiation, gathered by the detection system is not the total generated radiation, but only a small part, coming from recombination just beneath the junction. That is why the overall radiation, detected on these diodes is low and a direct measurement of the electroluminescence efficiency of dislocation network diodes is not possible. However, an estimate of the achievable efficiency from the diode containing dislocation network can be made, based on the normalized electroluminescence spectra. We assume that the band-to-band internal efficiency is not influenced by the presence of the network and is the same for sample S24 (0.8%) and the diode containing the network. Taking the ratio of the areas of the dislocation-related peak and the band-to-band peak, one obtains internal quantum efficiency of about 0.1% for the dislocation-related radiation.

As shown, the injection of carriers by p-n junction leads to spreading of the current and to significant losses in the bulk, resulting, partially, in band-to-band radiation. An enhancement of the efficiency can be expected by a more local injection. One can make use of an accumulation layer at MOS structure for that purpose.

9.4.2. Electroluminescence from metal oxide silicon structures

Recombination in the dislocation network can be obtained by injecting minority carriers through a thin oxide layer [Kit2006]. The structure of the device is shown in Figure 9.13a. Silicon p-type substrate containing dislocation network at a depth of about 50 nm beneath the surface is covered with a 2 nm thin oxide layer. On top of the oxide a titanium contact is deposited.

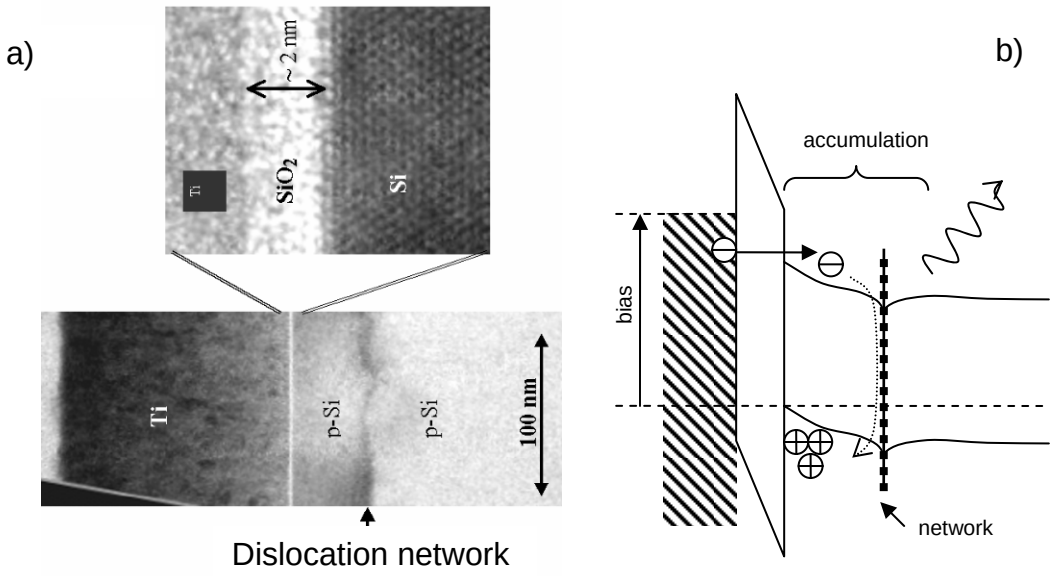

Figure 9.13. a) Cross sectional TEM image of a MOS LED consisting of a titanium contact deposited over a 2 nm Si oxide layer. The dislocation network is positioned in a depth about 50 nm by wafer bonding of p-type wafers with (100) orientation.
b) Schematic band diagram in the MOS diode under forward bias. The dislocation network is in (or close to) the accumulation layer and causes a band bending in its vicinity. Radiative recombination of carriers occurs at the dislocations.

The structure is a MOS tunnelling diode. When applying negative voltage on the Ti contact, holes are attracted building an accumulation layer close to the interface Si/oxide (Figure 9.13b). An electron current occurs due to tunnelling of electrons through the oxide. When a dislocation network is positioned near the Si/oxide interface, close to/within the accumulation layer, the minority carriers are attracted by the dislocation network due to the band bending and recombine predominantly at the dislocations. Thus the radiative recombination is dominated by the dislocation-related D1-line at about 1.5 μm. This is clearly visible from the EL spectra shown in Figure 9.14.

To estimate the efficiency the electroluminescence of the MOS light emitter, its spectrum is compared with that of a silicon diode under forward bias (Figure 9.14). The MOS device internal efficiency is about 0.1% at 80 K. The luminescence of the devices is purely dislocation dominated and persistent to temperatures about 220 K.

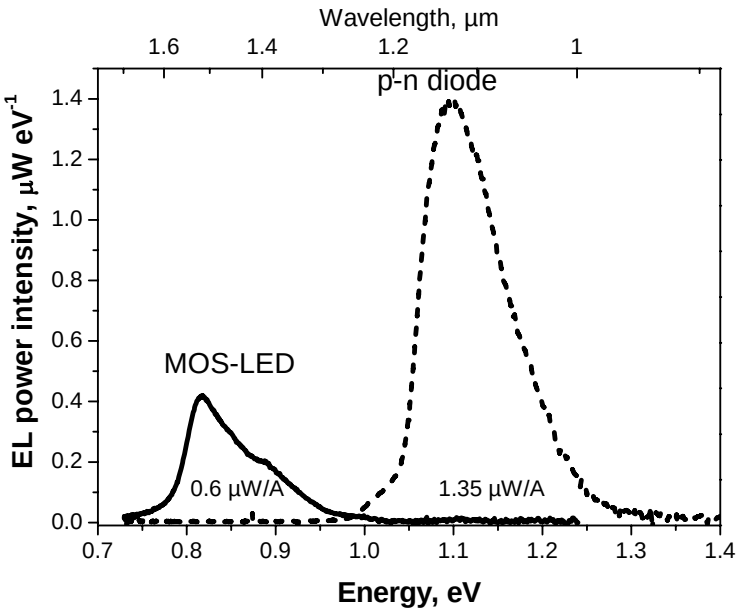

Figure 9.14. Band-to-band emission is suppressed because of the tunnelling injection. Comparison of the EL internal quantum efficiencies of a Si p-n diode and the MOS-emitter. The p-n diode was measured at 300 K under forward bias (yielding an efficiency of 0.15%. For the MOS-LED we estimated at 80 K an efficiency of about 0.1%.

9.5. Summary

Three different methods for reproducible formation of a dislocation-rich region beneath the surface of the wafer - silicon implantation and annealing, epitaxially grown SiGe buffer, and direct wafer bonding - have been investigated in view of their room temperature sub-band-gap radiation. All three dislocation-rich areas exhibit D1 emission at room temperature. Although, strong luminescence at 80K is present, the room temperature internal quantum efficiencies are less than expected several present.

In order to utilize the dislocation radiation for silicon based light emitters an improvement of the room temperature efficiency is necessary. There are two possibilities for such improvement. One is to increase the dislocation recombination activity by introducing a deliberate contamination and the other is to optimize the dislocation density (Paragraph 9.3).

Instead, an increase, the dislocation-related radiation tends to saturate upon increasing the injection. As that trend have been observed on the samples with low dislocation activity at relatively high injection currents (Paragraph 9.1), it is an indication that enhancement of the luminescence can be achieved by increasing the dislocation concentration. On the other hand, optimal D1 emission requires a certain spacing between the dislocations. The samples with dislocation networks show that single D1 emission can be obtained by a relatively large

spacing between the dislocations. Thus, one should find an optimal dislocation density, for efficient dislocation luminescence.

All three suggested methods for dislocation engineering allow to control the dislocation formation by the parameters of sample preparation (e.g. implantation dose and energy; type, time, and temperature of the annealing; germanium concentration gradients in the buffer; angles of misorientation, etc.). However, the most direct access to the dislocation formation is present in case of wafer direct bonding. The dislocation networks exhibit the unique property of adjusting the emission wavelength by the angles of misorientation.

The networks are two-dimensional structures and can be prepared several ten nanometers close to the surface. Stacks of dislocation networks, with a depth periodicity of several ten nanometers, can potentially be produced by multiple bonding. Thus, enhancement of the efficiency or ‘multicolour’ light emitters can be realised.

Because of the conductive properties of the dislocations in the network, an efficient local electrical injection of minority carriers cannot be established by means of a p-n junction. A possibility to enhance the injection is tunnelling through MOS structures. However, the electrical excitation through a thin oxide reveals a strong thermal quenching, which needs to be explored further.

The D1 emission maximum shows a wavelength shift upon increasing the temperature, which follows the silicon band gap shrinkage in the temperature range above 100 K. This observation can be explained by an asymmetric transition, between a deep level close to the conduction and a shallow one close the valence band edge.

Conclusions

It was shown that the recombination at dislocations is strongly influenced by the presence of metals at the dislocation sites and the dislocation recombination activity correlates with their electrical activity. That correlation allows to utilize photoluminescence mapping at room temperature for revealing and characterising of the dislocation-rich regions in multicrystalline silicon. The dislocation and band-to-band luminescence are essentially reversed. The band-to-band intensity is related to the diffusion length of minority carriers. Therefore it can be used for quantitative measurements of the diffusion length, in case the surface recombination rate is controlled.

Photoluminescence mapping can be used also for the detection of optically active defects in solar grade materials. Thus, $\beta FeSi_2$ precipitates, with a luminescence at 0.8 eV, were detected within the grains of block cast and HEM materials. They show a characteristic feature of quantum dots, namely blinking. At the grain boundaries strong radiation in the range 0.93-0.95 eV was detected, related to the presence of sulphur or selenium.

The dislocation lines D1 and D2 are due to transitions involving deep centres. D2 can be explained by a transition between a deep centre and a three dimensional band of the semiconductor, while D1 is a transition between a deep level and a dislocation one-dimensional band, representing a shallow level. Such asymmetric D1 transition leads to a temperature shift of the D1 emission maximum, which follows the band gap shrinkage of silicon.

The deep levels related to D1 and D2 are most probably located in the dislocation vicinity. Thus, they are influenced by the dislocation's local surrounding and gettering.

Anomalous temperature behaviour of band-to-band luminescence was detected for a variety of silicon materials. It is related to the presence of shallow nonradiative recombination levels. A possible origin of the shallow levels may be dopants or one-dimensional dislocation bands.

The relation between D3 and D4 is generally confirmed by their spatial correlation. Both appear together at nearly equal intensity. A quasi-non-correlation can appear on places where the two- and three-phonon assisted band-to-band recombination is strong. This is indication for residual mechanical stress.

The properties of dislocations can be utilized for the preparation of light emitter based on silicon. Two main approaches were revealed. One is based on the enhancement band-to-band luminescence and the other on dislocation-related radiation.

An enhancement of the band-to-band radiation can be achieved by formation of dislocation loops in the emitter due to implantation of dopants and annealing. It was found, that the enhancement of the band-to-band recombination is due to reduction of the nonradiative recombination, caused by the getter effect of the implanted layer and is not related to confinement of carriers at the dislocation loops. Furnace annealing and phosphorous implantation are more favourable for the gettering and result in a more efficient band-to-band radiation than boron implantation and RTA. A second effect, related to the dopant profile in the emitter, allows devices produced by furnace annealing, to reach carriers injection levels in base close to the optimum for maximal radiative recombination efficiency.

It was found, that the silicon light emitter based on implantation of dopants and annealing uses a big volume from the substrate for generation of light. The luminescence, generated in the bulk and the non-appropriate wavelength of the emission (1.13 μm) renders the application of such light emitter in the microelectronics difficult.

Light emitters, utilizing the emission from dislocation-rich areas, created in a well localized wafer depth were explored. Three different methods for reproducible formation of dislocation-rich region beneath the wafer surface were investigated in view of their room temperature sub-band-gap radiation: (1) silicon implantation and annealing, (2) epitaxially grown SiGe buffer, and (3) direct wafer bonding. All three methods for dislocation engineering allow to control the dislocation formation by the parameters of the sample preparation.

The most direct access to the dislocation formation is by wafer direct bonding, where also the emission spectrum can be controlled by the angles of misorientation. Although strong luminescence at 80 K is present, the room temperature internal quantum efficiencies of the electroluminescence was found less than the expected several present.

The most promising dislocation based emitter is that, which utilizes dislocation network produced by wafer bonding. However, the problems with the electrical excitation of the luminescence should be solved in order to obtain efficient room temperature D1 emission, like that in the case of photoexcitation.

References

[Ale1990] H. Alexander; "Versetzungen in Halbleitern" in Festkörrperforschung für die Informationstechnik (ed. R. Hölzle and W. Schmitz), Vorlesungsmanuskripte (1990) 10.1.

[Arg2004] T. Arguirov, M. Kittler, W. Seifert, D. Bolze, K.–E. Ehwald, P. Formanek and J.Reif; Sol. Stat. Phen. 95-96 (2004) 289.

[Arg2005] T. Arguirov, M. Kittler, W. Seifert, X. Yu; Material Sci. and Engineering B 124-125 (2005) 431.

[Arg2006] T. Arguirov, M. Kittler, W. Seifert, X. Yu and M. Reiche; Material Sci. and Engineering B 134 (2006) 109.

[Arg2007] T. Arguirov, W. Seifert, G. Jia, M. Kittler; Semiconductors 41 (2007) 405.

[Bae2005] D. Baek, S. Rouvimov, B. Kim, T.-C. Jo, and D. K. Schroder; Appl. Phys. Lett. 86 (2005) 112110.

[Ban1999] U. Banin, M. Bruchez, A. P. Alivisatos, T. Ha, S. Weiss, and D. S. Chemla; J. Chem. Phys. 110 (1999) 1195.
K. T. Shimizu, R. G. Neuhauser, C. A.Leatherdale, S. A. Empedocles, W.K. Woo, and M. G. Bawendi; Phys. Rev. B 63 (2001) 205316.
M. Kuno, D. P. Fromm, H. F. Hamann, A. Gallagher, and D. J. Nesbitt; J. Chem. Phys. 115 (2001) 1028.
M. Pelton, D. G. Grier, and P. Guyot-Sionnest; Appl. Phys. Lett. 85 (2004) 819.

[Bec1989] D. S. J. Beckett, M. K. Nissen, and M. L. W. Thewalt; Phys. Rev. B 40 (1989) 9618.

[Bin2002] S. Binetti, S. Pizzini, E. Leoni, R. Somaschini, A. Castaldini, and A. Cavallini ; J. Appl. Phys. 92 (2002) 2437.

[Bin2003] S. Binetti, A. Le Donne, V.V. Emtsev, and S. Pizzini; J. Appl. Phys. 94 (2003) 7476.

[Bin2005y] S. Binetti, private communication; .

[Bir2005] J. E. Birkholz, K. Bothe, D. Macdonald, and J. Schmidt; J. Appl. Phys. 97 (2005) 103708.

[Blu2000] A. Blumenau, R. Jones, S. Öberg, T. Frauenheim, and P.R. Briddon; J. Phys.: Condens. Matter 12 (2000) 10123.

[Blu2001] A. Blumenau, R. Jones, S. Öberg, P.R. Briddon, T. Frauenheim; Phys. Rev. Lett. 87 (2001) 187404.

[Boy2004] O.Boyraz and B. Jalali; Opt. Express 12 (2004) 5269.

[Bra1998] P.L. Bradfield, T.G. Brown, and D.G. Hall; Phys. Rev. B 38 (1988) 3533.

[Bro1986] T.G. Brown and D.G. Hall; Appl. Phys. Lett. 49 (1986) 245.

[Bru1995] M. Bruel; Electronics Letters 31 (1995) 1201.

[Bru1997] M. Bruel, B. Aspar and A.-J. Auberton-Hervé ; Jpn. J. Appl. Phys. 36 (1997) 1636.

[Buo2006] T. Buonassisi, A. A. Istratov, M. D. Pickett, M. Heuer, J. P. Kalejs, G. Hahn, M.A. Marcus, B. Lai, Z. Cai, S. M. Heald, T. F. Ciszek, R. F. Clark, D. W. Cunningham, A. M. Gabor, R. Jonczyk, S. Narayanan, E. Sauer and E. R. Weber; Prog. Photovolt:Res. and Appl. 14 (2006) 513.

T. Buonassisi, A. A. Istratov, M. D. Pickett, M. A.Marcus, T. F. Ciszek, and E. R. Weber; Appl. Phys. Lett. 89 (2006) 042102.
T. Buonassisi, A. A. Istratov, S. Peters, C. Ballif, J. Isenberg, S. Riepe, W. Warta, R. Schindler, G. Willeke, Z. Cai, B. Lai, and E. R. Weber; Appl. Phys. Lett. 87 (2005) 121918.
T. Buonassisi, A. A. Istratov, M. Heuer, M. A. Marcus, R. Jonczyk, J.Isenberg, B. Lai, Z. Cai, S. Heald, W. Warta, R. Schindler, G. Willeke, E.R. Weber; J. Appl. Phys. 97 (2005) 074901.

[Can1987] L. T. Canham, K. G. Barraclough, and D. J. Robbins; Appl. Phys. Lett. 51 (1987) 1509.

[Can1990] L. T. Canham; Appl. Phys. Lett. 57 (1990) 1046.

[Cav1993] A. Cavallini, M. Vandini, F. Corticelli, A. Parisini, and A. Armigliato; Inst. Phys.Conf. Ser. 134 (1993) 115.

[Che1984] J. Chelikowsky, J. Spence; Phys. Rev. B 30 (1984) 694.

[Che2001] M.-J. Chen, C.-F. Lin, W. T. Liu, S. T. Chang, and C. W. Liu; J. Appl. Phys. 89 (2001) 323.

[Che2004] M.-J. Chen, E.-Z. Liang, S.-W. Chang, and C.-F. Lin; J. Appl. Phys. 90 (2001) 789.

[Cof1994] S. Coffa, G. Franzò, F. Priolo, A. Polman and R. Serna; Phys. Rev. B 49 (1994) 16313.

[Cue1997] A. Cuevas, M. Stocks, S. Armand, M. Stuckings, A. Blakers, and F. Ferrazza; Appl. Phys. Lett. 70 (1997) 1017.

[Dav1989] G. Davies, H. Brian, E C Lightowlers, K. Barraclough, and M. F. Thomaz; Semicond. Sci. Technol. 4 (1989) 200.

[Dav2002] G. Davies, R. Harding, T. Jin, A. Mainwood, and J. Leung-Wong; Nuclear Instr.and Methods in Phys. Research B 186 (2002) 1.

[Dew1996] I. De Wolf; Semicond. Sci. Technol. 11 (1996) 139.

[Dro1976] N.A. Drozdov, A.A. Patrin, V.D. Tkatchev; Sov.-Phys. JETP Lett. 23 (1976) 597.

[Dro1977] N.A. Drozdov, A.A. Patrin, V.D. Tkatchev; Phys. Stat. Sol.(b) 83 (1977) K137.

[Dro1981] N.A. Drozdov, A.A. Patrin, and V.D. Tkatchev; Phys. Stat. Sol.(a) 64 (1981) K63.

[Dum1957] W. P. Dumke; Phys. Rev. 105 (1957) 139.

[Dzi1977] J. Dziewior and W. Schmid; Appl. Phys. Lett. 31 (1977) 346.

[Ead1985] W. D. Eades and R. M. Swanson; J. Appl. Phys. 58 (1985) 4267.

[Eag1991] D. J. Eaglesham, J. Michel, E. A. Fitzgerald, D. C. Jacobson, J. M. Poate, J. L.Benton, A. Polman, Y.-H. Xie, and L. C. Kimerling; Appl. Phys. Lett. 58 (1991) 2797.

[Efr1997] Al. L. Efros and M. Rosen; Phys. Rev. Lett. 78 (1997) 1110.

[Ell1957] R. J. Elliott; Phys. Rev. 108 (1957) 1384.

[Fek1999] O.V. Feklisova, G. Mariani-Regula, B. Pichaud, and E.B. Yakimov; Phys. Stat. Sol. 171 (1999) 341.

[Fil1996] A. B. Filonov, D. B. Migas, V. L. Shaposhnikov, N. N. Dorozhkin, G. V. Petrov,V. E. Borisenko, W. Henrion, and H. Lange; J. Appl. Phys. 79 (1996) 7708.

[Fil1998] A. B. Filonov, D. B. Migas, V. L. Shaposhnikov, V. E. Borisenko, W. Henrion, M.Rebien, P. Stauss, H. Lange, G. Behr; J. Appl. Phys. 83 (1998) 4410.

[Fil1999] A. B. Filonov, D. B. Migas, V. L. Shaposhnikov, N. N. Dorozhkin, V. E.Borisenko, A. Heinrich, and H. Lange; Phys. Rev. B 90 (1999) 16494.

[Fra1997] G. Franzo, S. Coffa, F. Priolo, C. Spinella; J. Appl. Phys. 81 (1997) 2784.

[Fuk1993] S. Fukatsu, N. Usami, Y. Shiraki, A. Nishida, and K. Nakagawa; Appl. Phys. Lett. 63 (1993) 967.

[Fuk1996] S. Fukatsu, Y. Mera, M. Inoue, K. Maeda, H. Akiyama, and H. Sakaki; Appl. Phys. Lett. 68 (1996) 1889.

[Gai1995] M. Gail, G. Abstreiter, J. Olajos, J. Engvall, H. Grimmeiss, H. Kibbel and H.Presting; Appl. Phys. Lett. 66 (1995) 2978.

[Gao2003] Y. Gao, S. P. Wong, W. Y. Cheung, G. Shao, and K. P. Homewood; Appl. Phys. Lett. 83 (2003) 42.

[Gnu1974] U. Gnutzmann and K. Clausecker; App. Phys. 3 (1974) 9.

[Goe1980] U. Gosele, W. Frank, and A. Seeger; Appl. Phys. 23 (1980) 361.
A. G. Shaikh,W. Schröter, and W. Bergholz; J. Appl. Phys. 98 (1985) 2519.
G. B. Bronner, J. D.Plummer; J. Appl. Phys. 61 (1987) 5286.
W. Schröter and R. Kühnapfel; Appl. Phys.Lett. 56 (1990) 2207.
E. Ö. Sveinbjdrnsson, O. Engström, and U. Söddervall; J. Appl.Phys. 73 (1993) 7311.
S. Coffa, G. Franco, C. M. Camalleri, and A. Giraffa; J. Appl.Phys. 80 (1996) 161.

[Gre1987] M. A. Green ; High Efficiency Silicon Solar Cells, Trans Tech Publications Ltd, Switzerland (1987) 228-229.

[Gre2001] M. A. Green, J. Zhao, A. Wang, P. Reece, and M. Gal; Nature (London) 412 (2001) 805.

[Gri1992] M. G. Grimaldi, P. Baeri, C. Spinella, and S. Lagomarsino; Appl. Phys. Lett. 60 (1992) 1132.

[Hal1952] R. N. Hall; Phys. Rev. 87 (1952) 387.

[Hay2004] S. Hayama, G. Davies, and K. M. Itoh; J. Appl. Phys. 96 (2004) 1754.

[Hei2001] L. Heikkilä,T. Kuusela, and H.-P. Hedman; J. Appl. Phys. 89 (2001) 2179.

[Hen1994] A. Henry, E. Sörman, S. Andersson, W. M. Chen, B. Monemar, and E. Janzén; Phys. Rev. B 49 (1994) 1662.

[Hig1990] V. Higgs, C. E. Norman, E. C. Lightowlers, P. Kightley; Poceeding of 20thinternational conference Physics of semiconductors (ed. E.M. Anastassakis and J. D. Joanopoulos), Thessaloniki, Greece (1990) 706.

[Hig1991] V. Higgs, P. Kightley, P. J. Goodhew, P. D. Augustus; Appl. Phys. Lett. 59 (1991) 829.

[Hig1992] V. Higgs, M. Goulding, A. Brinklow, and P. Kighthley; Appl. Phys. Lett. 60 (1992) 1369.

[Hig1992a] V. Higgs, E. C. Lightowlers, S. Tajbakhsh, and P. J. Wright; Appl. Phys. Lett. 61(9) (1992) 1087.

[Hig1993] V. Higgs E.C. Lightowlers; Materials Research Society Symposium Proceedings 263 (1993) 305.

[Hig1993a] V. Higgs and M. Kittler ; Appl. Phys. Lett. 63 (1993) 2085.

[Hoa2006] T. Hoang, P. LeMinh, J. Holleman, J. Schmitz; IEEE Electron Device letters 27 (2006) 105.

[Ico2002] F. Icona, D. Pacifici, A. Irrera, M. Miritello, G. Franzò, F. Priolo, D. Sanfilippo, G.Di Stefano, and P. G. Fallica; Appl. Phys. Lett. 81 (2002) 3242.

[Ike1998] K. Ikeda, T. Sekiguchi, S. Ito, and M. Suezawa; Sol. Stat. Phen. 63-63 (1998) 481.

[ISE2001] ISE TCAD Release 7.0, V0l. 2b, DIOS; (2001) .

[Jon2000] R. Jones, B. J. Coomer, J. P. Goss , S. Öberg, and P.R. Briddon; Phys. Stat. Sol.(b) 22 (2000) 133.

[Kar2000] S. W. Kartalopoulos; Introduction to DWDM technology, Wiley IEEE Press, NewYork (2000) 55.

[Kit1993a] M Kittler and W. Seifert; Phys. Stat. Sol. 138 (1993) 687.

[Kit1993b] M Kittler, W. Seifert, and Z. J. Radzimski; Appl. Phys. Lett. 62 (1993) 2513.

[Kit1993c] M. Kittler, W. Seifert and W. Higgs; Phys. Stat. Sol.(a) 137 (1993) 327.

[Kit1995a] M. Kittler, W. Seifert, M. Stemmer, and J. Palm; J. Appl. Phys. 77 (1995) 3725.

[Kit1995b] M Kittler, W. Seifert and V. Higgs; Mat. Res. Soc. Symp. Proc. 378 (1995) 989.

[Kit1995c] M Kittler and W. Seifert; Scanning Microscopy 9 (1995) 677.

[Kit1995d] M. Kittler, C, Ulhaq-Bouillet, and V. Higgs; J. App. Phys. 78 (1995) 4573.

[Kit2002] M. Kittler, W. Seifert, T. Arguirov, I. Tarasov, S. Ostapenko; Solar Energy Materials and Solar Cells 72 (2002) 465.

[Kit2004] M. Kittler, T. Arguirov,W. Seifert; Proceedings of SPIE 5357 (2004) 164.

[Kit2004a] M. Kittler and W. Seifert; Sol. Stat. Phen. 95-96 (2004) 197.

[Kit2005] M. Kittler, T. Arguirov, A. Fischer, W. Seifert; Opt. Mater. 27 (2005) 967.

[Kit2005a] M. Kittler, M. Reiche, T. Arguirov, W. Seifert and X. Yu; IEDM Tech. Digest (2005) 1027.

[Kit2006a] M. Kittler, M. Reiche, X. Yu, T. Arguirov, O.F. Vyvenko, W. Seifert, T. Mchedlidze, G. Jia, T. Wilhelm; IEDM Technical Digest (2006) 845.

[Kno2003] K. Knobloch, M. Kittler, W. Seifert; J. Appl. Phys. 93 (2003) 1069.

[Koch2003] W. Koch, A.L. Endrös, D. Franke, C. Häßler, J. P. Kalejs, and H. J. Möller; Bulk crystal growth and wafering for PV in Handbook of photovoltaic science andengineering (ed. A. Luque and S. Hegedus) John Wiley & Sons. Ltd (2003) 205-254.

[Kos1999] Y. Koshka, S. Ostapenko, I. Tarasov, S. McHugo, and J. P. Kalejs; Appl. Phys. Lett. 74 (1999) 1555.

[Kus1992] S. Kusanagi, T. Sekiguchi, and K. Sumino; Appl. Phys. Lett. 61 (1992) 792.

[Kve1995] V.V. Kveder, E.A. Steinman, S. A. Shevchenko, and H.G. Grimmeiss; Phys. Rev. B. 51 (1995) 10520.

[Kve1996] V.V. Kveder, E.A. Steinman, and H.G. Grimmeiss; Sol. Stat. Phen. 47-48 (1996) 419.

[Kve2001] V. Kveder, M. Kittler, and W. Schröter; Phys. Rew. B 63 (2001) 115208.

[Kve2004] V. Kveder, M. Badylevich, E. Steinman, A. Izotov, M. Seibt, and W. Schröter; Appl. Phys. Lett. 84 (2004) 2106.

[Kve2005] V. Kveder, M. Badylevich, W. Schröter, M. Seibt, E. Steinman, A. Izotov; Phys. Stat. Sol.(a) 202 (2005) 901.

[Lau1985] P. Lautenschlager, P. B. Allen, and M. Cardona; Phys. Rev. B 31 (1985) 2163.

[Lea1976] H.J. Leamy, L.C. Kimerling, S.D. Ferris; Scanning Electron Microscopy (Part IV), Proc. Workshop on Microelectronic DeviceFabrication and Quality Control with the SEM (ed. O. Johari), IIT Research Institute, Chicago (1976) 529 - 538.

[Lea1985] H. J. Leamy; J. Appl. Phys. 53(6) (1982) R51.

[Lel1992] Yu. Lelikov, Yu. Rebane, S. Ruvimov, D. Tarhin, A. Sitnikova and Yu. Shreter; Mater. Sci. Forum 83-87 (1992) 1321.

[Lig1990] E. C. Lightowlers; Photoluminescence Characterisation in Growth and Characterisation of Semiconductors, Adam Hilger, New York (1990) 135–164.

[Lin2001] C.-F. Lin, M.-J. Chen, S.-W. Chang, P.-F. Chung, E.-Z. Liang, T.-W. Su, and C.W. Liu; Appl. Phys. Lett. 78 (2001) 1808.

[Liu2000] C. W. Liu, M. H. Lee, M.-J. Chen, I. C. Lin, and C.-F. Lin; Appl. Phys. Lett. 76 (2000) 1516.

[Liu2004] A. Liu, R. Jones, L. Liao, D. Samara-Rubio, D. Rubin, O. Cohen, R.Nicolaescu, and M. Pannicia; Nature 427 (2004) 615.

[Lou2004] M. A. Lourenço, M.S.A. Siddiqui, G. Shao, R .M. Gwilliam, and K. P.Homewood; Phys. Stat. Sol.(a) 201 (2004) 239.

[Mac1995] G. G. Macfarlane and V. Roberts; Phys. Rev. 98 (1955) 1865.

[Mac2004] D. Macdonald and L. J. Geerligs; Appl. Phys. Lett. 85 (2004) 4061.

[Mac2005] D. Macdonald, A. Cuevas, A. Kinomura, Y. Nakano, L. J. Geerligs; J. Appl. Phys. 97 (2005) 33523.

[Mae1995] K. Maex and B. L. Welss; Properties of metal silicides, INSPEC IEE, London (1995) 317.

[McH1997] S. A. McHugo; Appl. Phys. Lett. 71 (1997) 1984.

[Miy1997] M. Miyazaki, S. Miyazaki, S. Ogushi, t. Ochiai, M. Sano, T. Shigematsu; Jpn. J. Appl. Phys 36 (1997) L380.

[Möl1996] H.J. Möller; Sol. Stat. Phen. 78 (1996) 127.

[Mudr2002] A.V. Mudryi, A.I. Petuk, I. A. Shakin, A. G. Ulyashin, R. Job, W. R. Fahrner, A.Fedotov, A. Mazanik, N. Drozdov; Solar Energy Materials and Solar Cells 72 (2002) 503.

[New1957] R. Newman; Phys. Rev. 105 (1957) 1715.

[Ng2001] W. L. Ng, M. A. Lourenço, R .M. Gwilliam, S. Ledain, G. Shao and K. P.Homewood ; Nature(London) 410 (2001) 192.

[Nun1998] R. W. Nunes, J. Bennetto, D. Vanderbilt; Phys. Rev. B 58 (1998) 12563.

[Oeh2006] M. Oehme, J. Werner, M. Jutzi, G. Wöhl, E. Kasper, M. Berroth; Thin Solid Films 508 (2006) 393.

[Ort1990] J.W. Orton, P. Blood; The Electrical Characterization of Semiconductors: Measurement of Minority Carrier Properties, Academic Press, London (1990) .

[Oss2003] S. Ossicini, L. Pavesi, and F. Priolo ; Light Emitting Silicon for Microelectronics, Springer Tracts in Modern Physics Vol. 194, Springer, Berlin (2003) .

[Ost1999] S. Ostapenko; Appl. Phys. A 69 (1999) 225.

[Ost2000] S. Ostapenko, I. Tarasov, J. P. Kalejs, C. Haessler, and E.-U. Reisner; Semicond. Sci. Technol. 15 (2000) 840.

[Pan1975] J.L. Pankove; Optical Processes in Semiconductors, Dover, New York (1975) 165-166.

[Pan2004] G. Z. Pan, R. P. Ostroumov, Y. G. Lian, K. N. Tu and K.L. Wang; IEEE (2004) 343.

[Pav2003] L. Pavesi; J. Phys.: Condens. Matter 15 (2003) R1169.

[Pea1989] A. R. Peaker, B. Hamilton, G. R. Lahiji, I. E. Ture and G. Lorimer; Material Sci. and Engineering B 4 (1989) 123.

[Piz2000] S. Pizzini, M. Acciarri , E. Leoni, and A. Le Donne; Phys. Stat. Sol.(b) 22 (2000) 141.

[Piz2000a] S. Pizzini, M. Guzzi, E. Grilli, and G. Borionetti; J. Phys.: Condens. Matter 12 (2000) 10131.

[Piz2001] S. Pizzini, S. Binetti, A. Le Donne, E. Leoni, M. Acciarri, G. Salviati, and L.Lazzaroni; Sol. Stat. Phen. 78-79 (2001) 57.

[Pri1998] F. Priolo, G. Franzò, S. Coffa, and A. Carnera; Phys. Rev. B 57 (1998) 4443.

[Pri2001] F. Priolo, G. Franzò, D. Pacifici, V. Vinciguerra, F. Iacona, and A. Irrera; J. Appl. Phys. 89 (2001) 264.

[Rab1993] Y.T. Rabine, J.W.Steeds; Phys. Rev. B 48 (1993) 14963.

[Rad1992] Z. J. Radzimski, T. Q. Zhou, A. Buczkowski, G. A. Rozgonyi, D. Finn, L. G.Hellwig, and J. A. Ross; Appl. Phys. Lett. 60 (1992) 1096.

[Rap1962] P. Rappaport ; Radiation Damage to Silicon Solar Cells, Proc. 2nd IEEE PVSC (1962) 7.

[Rei2006] M. Reiche; Phys. Stat. Sol.(a) 203 (2006) 747.

[Ron2005] H. Rong, R. Jones, A. Liu, O. Cohen, D. Hak, A. Fang and M. Paniccia; Nature(London) 433 (2005) 725.

[Roo1954] W. van Roosbroeck and W. Shockley; Phys. Rev. 94 (1954) 1558.

[Saue1985] R. Sauer, J. Weber, J. Stolz, E.R. Weber, K.-H. Küsters, and H. Alexander; Appl. Phys. A 36 (1985) 1.

[Saue1986] R. Sauer, Ch. Kisielowski-Kemmerich, and H. Alexander; Phys. Rev. Lett. 57 (1986) 1472.

[Sch1974] H. Schlangenotto, H. Maeder, W. Gerlach; Phys. Stat. Sol.(a) 21 (1974) 357.

[Sch1998] J. Schmidt, A. G. Aberle, R.Hetzel; Appl. Phys. Lett. 73 (1998) 2167.

[Sch2003] B. Schuller, R. Carius, and S. Mantl; J. Appl. Phys. 94 (2003) 207.

[Sch2004] A. Schönecker, L. J. Geerligs, A. Müller; Sol. Stat. Phen. 95-96 (2004) 149.

[Sch2005] S. A. Schevchenko and A. N. Izotov; Phys. Stat. Sol.(c) 6 (2005) 1827.

[Sei1997] W. Seifert, K. Knobloch, and M. Kittler; Sol. Stat. Phen. 57-58 (1997) 287.

[Sek1994] T. Sekiguchi, V. V. Kveder, and K. Sumino; J. Appl. Phys. 76 (1994) 7882.

[Sek1996] T. Sekiguchi and K. Sumino; J. Appl. Phys. 79 (1996) 3253.

[Sha1999] J. S. Sharpe, Y. L. Chen, R. M. Gwilliam, A. K. Kewell, C. N. McKinty, M. A.Lourenço, G. Shao, K. P. Homewood, and K. R. Kirkby; Appl. Phys. Lett. 75 (1999) 1282.

[Sho1952] W. Shockley and W. T. Read; Phys. Rev. 87 (1952) 835.

[Sob2003] N. A. Sobolev, A. M. Emel'yanov, E. I. Shek and V. I. Vdovin; Physica B:Condensed Matter 340-342 (2003) 1031.

[Sob2004] N. A. Sobolev, A. M. Emel'yanov, E. I. Shek, and V. I.Vodovin; Sol. Stat. Phen. 95 - 96 (2004) 283.

[Spi1997] E. Spiecker, M. Seibt, and W. Schröter; Phys. Rev. B 55 (1997) 9577.

[Spi2000] C. Spinella, S. Coffa, C. Bongiorno, S. Pannitteri, and M. G. Grimaldi; Appl. Phys. Lett. 76 (2000) 173.

[Ste2005] E. A. Steinman; Phys. Stat. Sol.(c) 2 (2005) 1837.

[Sue1982] M. Suezawa, K. Sumino, Y. Nishina; Jpn. J. Appl. Phys. 21 (1982) L518.

[Sue1983] M. Suezawa and K. Sumino; Phys. Stat. Sol.(a) 78 (1983) 639.

[Sue1983a] M. Suezawa, Y. Sasaki, and K. Sumino; Phys. Stat. Sol.(a) 79 (1983) 173.

[Sun2003] J. M. Sun, T. Dekorsy, W. Skorupa, B. Schmidt, and M. Helm; Appl. Phys. Lett. 83 (2003) 3885.

[Sun2004] J. M. Sun, T. Dekorsy, W. Skorupa, A.Mücklich, B. Schmidt and M. Helm; Phys. Rev. B 70 (2004) 155316.

[Sve1996] E. Ö. Sveinbjörnsson and J. Weber; Appl. Phys. Lett. 69 (1996) 2686.

[Sve1998] E. Ö. Sveinbjornsson, S. Bengtsson, J. Weber, N. Keskitalo; Electrochemical Society Proceedings 36 (1998) 264.

[Taj1992] M. Tajima, H. Takeno, and T. Abe; Mater. Sci. Forum 83-87 (1992) 1327.

[Tak2004] M. Takauji, N. Seki, T. Suemasu, F. Hasegawa, and M. Ichida; J. Appl. Phys. 96 (2004) 2561.

[Tar1999] I. Tarasov, S. Ostapenko, S. McHugo, J. X. Cao, and J. P. Kalejs; Proceedings of 9th Workrkshop on Crystalline Silicon Solar Cell Materials and Processes NREL (1999) 112.

[Tar2000] I. Tarasov, S. Ostapenko, C. Haessler, and E.-U. Reisner; Material Sci. and Engineering B 71 (2000) 51.

[Ter1997] K. Terashima, T. Ikarashi, M. Watanabe, T. Kitano; Mater. Sci. Forum 258–263 (1997) 587.

[Tru2003] T. Trupke, M. A. Green, P. Würfel, P. P. Altermatt, A. Wang, J. Zhao, and R.Corkish; J. Appl. Phys. 94 (2003) 4930.

[Tru2003a] T. Trupke, J. Zhao, A. Wang, R. Corkish, M.A. Green; Appl. Phys. Lett. 82 (2003) 2996.

[Tsy1996] L. Tsybeskov, S. P. Duttagupta, K. D. Hirschman, and P. M. Fauchet; Appl. Phys. Lett. 68 (1996) 2058.

[Var1967] Y. P. Varshni; Phys. Stat. Sol. 19 (1967) 459.

[Vou1977] A Vouk and E C Lightowlers; J. Phys. C: Sol. Stat. Phys. 10 (1977) 3689.

[Vyv2002] O. F. Vyvenko, T. Buonassisi, A. A. Istratov, H. Hieslmair, A. C. Thompson, R.Schindler, and E. R. Weber; J. Appl. Phys. 91 (2002) 3614.

[Wat2001] K. Watanabe, M. Fujii, and S. Hayashi; J. Appl. Phys. 90 (2001) 4761.

[Web1982] J. Weber, H. Bauch, and R. Sauer; Phys. Rev. B 25 (1982) 7688.

[Web1990] J. Weber and M. Alonso; Defect Control in Semiconductors (ed. Sumino), Elsevier Science Publishers B.V, North –Holland (1990) 1453-1457.

[Web1999] J. Weber; Variation of bandgap with temperature in c-Si in Properties of Crystalline Silicon (ed. R. Hull), INSPEC IEE, London (1999) 391.

[Wor1992] K. Woronek, J. Weber, A. Höpner, H F. Ernst, R. Buchner, M. Stefaniak, and H.Alexander; Mater. Sci. Forum 83-87 (1992) 1315.

[Yu2006] X. Yu, T. Arguirov, M. Kittler, W. Seifert, M. Ratzke, M. Reiche; Materials Science in Semiconductor Processings 9 (2006) 96.

[Yu2006a] X. Yu, O.F. Vyvenko, M. Kittler, W. Seifert, T. Mchedlidze, T. Arguirov, M.Reiche; Semiconductors 41(4) (2007) 458.

List of abbreviation and symbols

α – absorption coefficient or angle of incidence or coupling between the dislocation and the impurity level
a – lattice constant
b – Burgers vector
β - excitation level or angle of refraction
B - recombination coefficient
BB – band-to-band
BE – bound exciton
b_e – edge component of the Burgers vector
c – speed of light
c_c – EBIC contrast
CMOS – Complementary Metal Oxide Semiconductor
CZ – Silicon monocrystalline material produced by Czochralski method
D – diffusion constant
DLTS – Deep level transient spectroscopy
Δn – excess carrier concentration
Δn_{tot} – surface density of excess carriers
e - the elementary charge
E_a – deactivation energy
EBIC – electron beam induced current
E_C –energy position of the conduction band
E_D – shallow trap energy
E_{D2} – photon energy of D2 radiation
E_{Dc},– split off energy of the conduction band, corresponding to 60° dislocations
E_{Dv},– split off energy of the valence band, corresponding to 60° dislocations
eeh, ehh – electron-electron-hole or electron-hole-hole recombination
EFG – Edge Defined Film Fed Growth
E_g - band gap energy of silicon
EL – electroluminescence
E_m– deep level energy position in the band gap
E_{mob} – mobility edge of the carriers trapped in the dislocation bands
E_{ph} – phonon energy
ε_{Si} –permittivity of silicon
E_V – energy position of the valence band
Φ – photon flux
F_n, F_p – quasi Fermi levels for electrons and holes, respectively
FZ – Silicon monocrystalline material produced by float zone method
G – generation rate
h – Planck's constant
HEM – Heat Exchange Method
η_{ext} – external quantum efficiency
η_{int} – internal quantum efficiency
η_{int} – power efficiency
I – current or peak intensity
I_S – radiant intensity
j – current density
k – Boltzmann's constant

L – diffusion length
L_{twist} , L_{tild} – Period of the dislocation network
λ – wavelength

Acknowledgements

First of all, I would like to express my largest gratitude to Prof. J. Reif for giving me the possibility to make my Ph.D. thesis at the Brandenburg University of Technology and for the careful reading and correcting the manuscript.

My deepest thanks belong to Prof. M. Kittler for his continuous encouragement and guidance throughout this research work. Without his creativeness and patient way of sharing knowledge, this work would have been impossible.

I wish to thank Dr. W. Seifert for the many illuminating discussions and his encouragements and support. He has given me the most interesting insides into the photovoltaic research, and in particular into EBIC and diffusion length measurements.

I am very grateful to Dr. Teimuraz Mtchedlidze for his very friendly and kind support.

I would like to express great thank to Prof. Reiner Schmid for the encouragements and for sharing his experience with me.

I would like to express my thanks to Dr. Dirk Wolfframm, Markus Ratzke, Sebastian Eckert, and Mark Hänel for the discussions and their help in many technical problems.

I especially thank my colleagues from the Joint Lab, Gobin Jia and Dr. Xuegong Yu for their help with the EBIC and cathodoluminescence measurements.

I am very thankful to Prof. O. Vyvenko, Dr. V. Akhmetov for the discussions and the advices.

I would like to acknowledge the contribution of Dr. P. Formanek for the TEM imaging, Dr. A. Fischer for the device simulation, and Dr. R. Kurps for the SIMS measurements.

I would like to extend my thanks to Dr. T. Wilhelm, Prof. M. Reiche for the wafer bonding and the TEM characterisation and to Dr. D. Bolze, Dr. K.–E. Ehwald , Dr. T. Hoang and Prof. J. Schmitz for the implantation of samples.

I appreciate the help of our secretary, Marion Borrmann. She arranged a lot of thinks for me during the years.

I would like also to express my gratitude to all my colleagues for the nice environment, which we have in the group.

I would like to say thank to my friends Mira and Niki for the encouragement and the long phone calls.

Finally, I feel incredibly grateful to my wife S. Kouteva-Arguirova and my daughter Joana for their love and patience. They were always close to me, sometimes propping up my failing strength, sometimes just making me smile.